Ernst Hellbär

Ion Movement and Space-Charge Distortions in the ALICE TPC

-2015-

Ion Movement and Space-Charge Distortions in the ALICE TPC

Master Thesis

by

Ernst Hellbär

Institut für Kernphysik
Goethe-Universität, Frankfurt am Main

Supervisors:
Prof. Dr. Harald Appelshäuser
Prof. Dr. Christoph Blume

October 27, 2015

Abstract

The Time Projection Chamber (TPC), a large gaseous detector, is the main particle identification device of the ALICE experiment at the CERN LHC. The desired performance of the TPC defines the requirements for the gas mixture used in the detector. The active volume was filled with either Ne-CO_2 (90-10) or Ne-CO_2-N_2 (90-10-5) during the first LHC running period. For LHC Run 2 the gas mixture is changed to Ar-CO_2. Calculations of relevant gas properties are performed for Ar-based gas mixtures and compared to Ne-based gas mixtures to identify the most suitable Ar mixture. The drift velocity of ions in Ar is lower than in Ne. The closing time of the gating grid has to be adjusted accordingly to avoid drift field distortions due to back-drifting ions. The drift times of ions in the TPC readout chambers are calculated for the respective gas mixtures to determine the time to collect all ions from the amplification region. For LHC Run 3 the TPC readout chambers will be upgraded. The Multiwire Proportional Chambers (MWPCs) will be replaced by readout chambers based on Gas Electron Multipliers (GEMs) which are operated in continuous mode. As a consequence an ion backflow of the order of 1 % causes significant space-charge distortions in the TPC drift volume. Similar distortions are expected in data taken specifically for the study of space-charge effects at the end of Run 1. The gating grid of the MWPCs is operated in the open state allowing the ions from the amplification region to enter the drift volume. The magnitude of the distortions in this data is measured and compared to the expectations for the TPC upgrade and results from current simulations.

Contents

1 Introduction 1

1.1 Standard Model 2

1.1.1 Quantum Chromodynamics 3

1.2 Quark-Gluon Plasma 4

1.3 Relativistic Heavy-Ion Collisions 6

2 ALICE - A Large Ion Collider Experiment 9

2.1 Coordinate Systems 10

2.1.1 Global Coordinate System 10

2.1.2 Local Coordinate System 10

2.2 Detectors 11

2.2.1 Central Detectors 11

2.2.2 Muon Spectrometer 13

2.2.3 Forward Detectors 13

3 The ALICE Time Projection Chamber 15

3.1 Detector Design 17

3.1.1 Gas Choice 17

3.1.2 Field Cage 18

3.1.3 Readout Chambers 18

3.1.4 Front-End Electronics and Readout 21

3.2 Upgrade 21

3.3 Physics Principles 23

3.3.1 Gas Ionization and Energy Loss 23

3.3.2 Drift of Electrons and Ions 24

3.3.3 Gas Amplification and Generation of the Signal 27

4 Simulation of Ion Drift in Ne- and Ar-Based Gas Mixtures 29

4.1 Gas Properties 30

4.1.1 Electron Transport 30

4.1.2 Ionization 34

4.1.3 Ion Mobility 38

4.2 Chamber Layout and Settings 39

4.3 Calculation of Ion Drift Times 41
4.3.1 Ion-Collection time 42
4.3.2 Optimization of the Ion-Collection time with Ar-CO_2 46
4.3.3 Ion Collection and Backflow with an Open Gating Grid 49
4.4 Conclusions 53

5 Space-Charge Effects 55
5.1 Calculation of Space-Charge Distortions 56
5.2 Expected Space-Charge Distortions for the TPC Upgrade 57
5.3 Space-Charge Distortions with an Open Gating Grid 59
5.3.1 TPC Tracking Performance 61
5.3.2 Magnitude of the Space-Charge Distortions 64
5.3.3 Comparison to Model Calculations 71
5.4 Outlook 73

6 Summary 75

Bibliography 77

1 Introduction

Way before elementary particle physics was born people have dealt with questions like "What is ordinary matter made of?" or "Why does it exist?". The discovery of the electron (e^-) by J. J. Thomson in 1897 indicated that atoms in fact have a substructure of even smaller particles. Ernest Rutherford's scattering experiment showed that most of the mass of an atom and its positive charge is located in a nucleus at the center of the atom. Based on this Niels Bohr proposed a model in 1914 in which hydrogen, the lightest atom, consists of one positively charged proton circled by one negatively charged electron [1]. Studying the nuclear beta decay in 1930, Pauli found first evidence of the existence of neutrinos in the energy spectrum of the electron and about 30 years later Lederman, Schwartz and Steinberger showed that each charged lepton has its respective neutrino [2]. Motivated by Dirac's calculations in relativistic quantum mechanics, Anderson measured the first positron, the antiparticle of the electron, in 1931 [3]. By discovering the neutron in 1932, Chadwick completed the classical model of elementary particle physics, in which the smallest constituents of the atoms are protons, neutrons and electrons.

Yukawa's proposal in 1934 of the strong force holding the nucleus together via the exchange of mesons and systematic studies of cosmic rays by several groups revealed the existence of the pion (π), which is Yukawa's meson, and the muon (μ^-) in 1947 [4]. As the first strange particles were discovered with the kaon (K^0) [5] in 1947 and the lambda (Λ) in 1950, the first modern particle accelerators were built to produce all kinds of new particles in the laboratory. In 1961 Murray Gell-Mann introduced a pattern to arrange all those particles in a systematic way and called it the *Eightfold Way* [6]. The lightest baryons and mesons are arranged in *octets* and the heavier baryons in *decuplets*, according to charge and strangeness. This led to Gell-Mann's prediction of the omega (Ω^-) particle and its discovery in 1964. On the foundation of the Eightfold Way, Gell-Mann and Zweig independently suggested that all hadrons consist of even smaller elementary particles which have been called quarks [7]. At that time the quark model consisted of three quarks (up, down, strange) whereas the existence of a fourth quark (charm) has been predicted by Bjorken and Glashow and was confirmed by Samuel C. C. Ting's and Burton Richter's observation of the J/ψ in 1974 [8, 9]. After the first measurement of the tau (τ^-) lepton in 1975 it did not take long to discover the fifth quark (bottom) by

Fermions			
Generation	I	II	III
Quarks	up (u) down (d)	charm (c) strange (s)	top (t) bottom (b)
Leptons	e^- ν_e	μ^- ν_μ	τ^- ν_τ

Gauge bosons				Scalar bosons
g	$W^\pm$	Z^0	γ	H

Table 1.1: The elementary particles of the Standard Model are divided into fermions (quarks and leptons), gauge bosons and a scalar boson.

observing the upsilon (Υ) meson [10]. In 1983 Carlo Rubbia's team at CERN (European Organization for Nuclear Research) reported the predicted and long awaited observation of the $W^\pm$- and the Z^0-bosons [11], which was an important step in confirming the electroweak theory. The existence of the sixth quark (top) was finally proven by experiments at Fermilab (Fermi National Accelerator Laboratory) in 1995. With the six quarks (u, d, s, c, b, t), six leptons (e^-, μ^-, τ^- and their corresponding neutrinos), their antiparticles and the mediators of the different interactions the list of elementary particles of modern physics is complete and unified in one theory called the *Standard Model* (Section 1.1).

1.1 Standard Model

As the established theory of elementary particle physics the Standard Model (SM) covers three of the four fundamental interactions between elementary particles summarized in Table 1.1. The SM is based on the local gauge group $SU(3) \otimes SU(2) \otimes U(1)$ where the SU(3) component describes the strong interaction and the $SU(2) \otimes U(1)$ component describes the electroweak interaction. The elementary particles are grouped into quarks and leptons (fermions with spin $\frac{1}{2}$), the gauge bosons (spin 1) and the Higgs boson (spin 0). In addition there is an antiparticle to each fermion with opposite quantum numbers. The fermions are divided into three generations where the mass of the particles increases with each generation.

The six flavors of quarks carry an electromagnetic charge of $+\frac{2}{3}e$ (up, charm, top) or $-\frac{1}{3}e$ (down, strange, bottom) as well as a weak charge and a color, which makes them take part in electromagnetic, weak and strong interactions. Bound states of multiple quarks are called hadrons which are separated into baryons (qqq) with $\mathcal{B} = 1$ and mesons ($q\bar{q}$) with $\mathcal{B} = 0$, where the baryon number $\mathcal{B}$ is conserved in all physical processes.

For the six leptons, the e^-, μ^- and τ^- interact weakly as well as electromagnetically due to their electromagnetic charge of $-1e$. The neutral massless neutrinos ν_e, ν_μ and ν_τ on the other hand interact only via the weak force. Similar to the baryon number for quarks, the lepton number of each generation $\mathcal{L}_e$, $\mathcal{L}_\mu$ and $\mathcal{L}_\tau$ is conserved in all physical processes. In extensions of the Standard Model neutrinos have a finite mass and oscillate between the different flavors resulting in a violation of the lepton number conservation.

The gauge bosons are the mediators or force carriers of the three different interactions. The gluon (g), the force carrier of the strong interaction, is neutral and massless. The same applies to the photon (γ) which is the force carrier of the electromagnetic interaction. In contrast the mediators of the weak interaction, the $\mathrm{W}^{\pm}$- and Z^0-bosons, acquire their large masses of $M_W = 80\,\mathrm{GeV}/c^2$ and $M_Z = 91\,\mathrm{GeV}/c^2$ through spontaneous electroweak symmetry breaking and the Higgs mechanism, requiring the scalar Higgs (H) boson [12].

1.1.1 Quantum Chromodynamics

As part of the Standard Model, a theory called Quantum Chromodynamics (QCD) has been developed to quantify the strong interaction between quarks and gluons in a similar way as Quantum Electrodynamics (QED) describes the electromagnetic interaction. On the grounds of theoretical arguments and experimental evidence [13] the color charge has been introduced as a quantum number attributed to strongly interacting particles. In total there are three colors (red, blue and green) and their respective anticolors. Each quark or antiquark carries a color or an anticolor. As opposed to the neutral photon in QED, the gauge boson of QCD, the gluon, carries one color and one anticolor at the same time. Because of this property the gluons can couple not only to the color charges of quarks and antiquarks but also to those of other gluons.

Free quarks and gluons cannot be observed under normal conditions which is tied to the fact that there are only colorless free particles in nature. The meaning of colorless in this regard is a combination of all three colors or anticolors, as for baryons and antibaryons, or a combination of a color and its respective anticolor, as for mesons. Thus separating the quarks of a hadron would lead to an arbitrary large potential and to the creation of a quark-antiquark pair before tearing the hadron apart. This property of QCD is called *confinement* and is reduced to the interaction of gluons between themselves. Confinement is characterized in the approximation

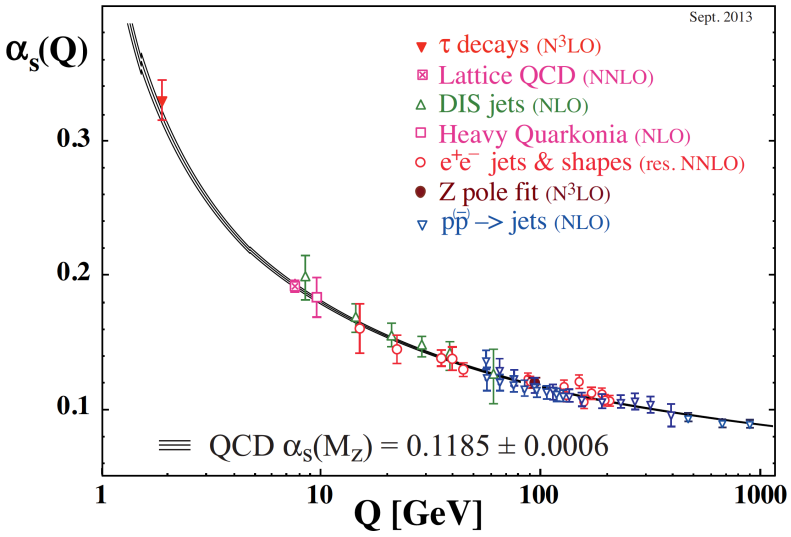

Figure 1.1: The coupling constant of the strong interaction $\alpha_s(Q)$ as a function of the energy scale Q, including results from several measurements [12].

of the quark-antiquark potential

$$V(r) = -\frac{4}{3}\frac{\alpha_s \hbar c}{r} + k \cdot r \,, \tag{1.1}$$

where r is the distance between the two particles, α_s is the coupling constant of the strong interaction and k is the string tension which describes the energy of the field per unit length. For short distances the potential looks Coulomb-like since the $\frac{1}{r}$ term dominates, whereas for long distances the $k \cdot r$ term is the dominant one and the potential increases linearly.

The coupling constant of the strong interaction α_s in Equation (1.1) is a measure of the coupling strength between two quarks and depends on the momentum transfer Q. The behavior of α_s as a function of Q is shown in Figure 1.1. For small momentum transfers, which corresponds to long distances between the quarks, the coupling increases, resulting in confinement. For large momentum transfers, corresponding to very short distances, the coupling decreases and the quarks can be assumed as quasi-free particles which is known as *asymptotic freedom*.

1.2 Quark-Gluon Plasma

Above a critical energy density ϵ_c of the order of $1\,\mathrm{GeV/fm^3}$ a deconfined state of matter, the quark-gluon plasma (QGP), is formed where quarks and gluons can move as free particles. Furthermore the chiral symmetry of QCD, which is spontaneously broken at low energy densities, is restored in the state of QGP. The critical energy density can be reached by increasing the temperature above a critical value of $T_c \approx 170\,\mathrm{MeV}$ or by compressing cold nuclear matter to net baryon densities of

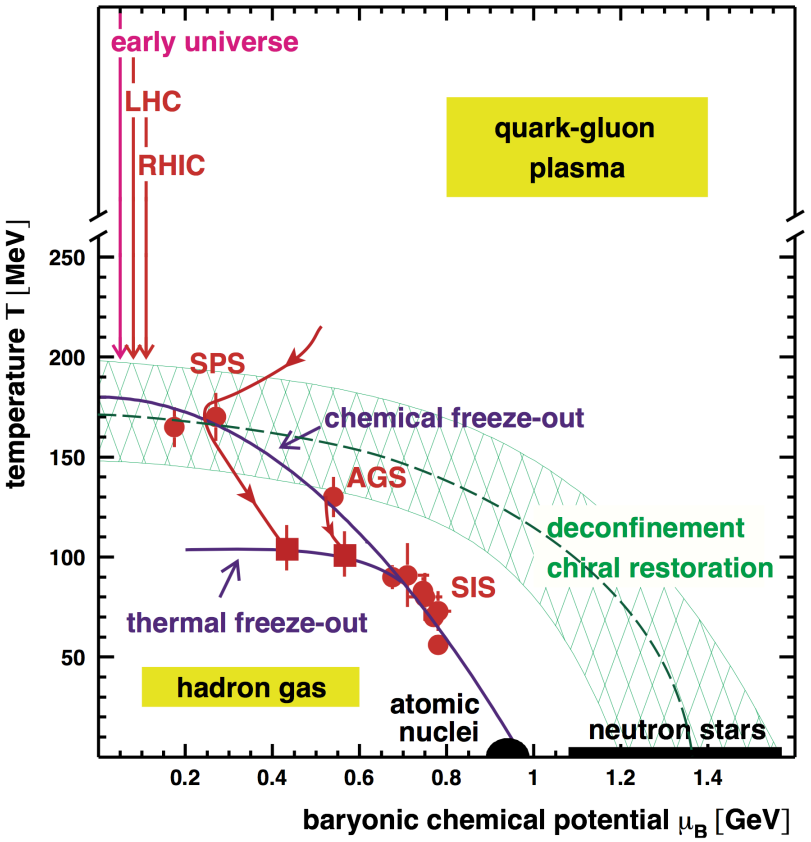

Figure 1.2: The QCD phase diagram as a function of the temperature T and the baryochemical potential μ_B. The region of the phase transition between the hadron gas and the QGP is indicated by the green cross-hatched area. The energy density regimes of several particle accelerators are marked with red points and arrows [14].

3–10 times the equilibrium density [14]. The phase diagram of QCD as a function of the temperature T and the baryochemical potential μ_B is shown in Figure 1.2. The cross-hatched region indicates the phase transition between the hadron gas and the QGP, which is assumed to be a smooth crossover at small baryon densities and a first-order phase transition at higher baryon densities [15]. In the laboratory a QGP can be produced by colliding heavy-ions at relativistic energies. At moderate beam energies, e.g. 35 A GeV at the future Compressed Baryonic Matter (CBM) experiment at FAIR (Facility for Antiproton and Ion Research), the colliding nuclei are partially stopped and heated enough to pass the critical energy density at high baryochemical potential and intermediate temperatures. For collisions at beam energies of 160 A GeV at the CERN Super Proton Synchrotron (SPS) the baryochemical potential decreases significantly and the temperature is near the critical temperature. At very high beam energies, e.g. $\sqrt{s} = 200$ GeV at Brookhaven National Lab's (BNL) Relativistic Heavy Ion Collider (RHIC) or $\sqrt{s} = 5.5$ TeV at the CERN Large Hadron Collider (LHC), the initial temperature of the formed QGP is well above T_c and the baryon density is close to zero, much like during the first few microseconds of the early universe.

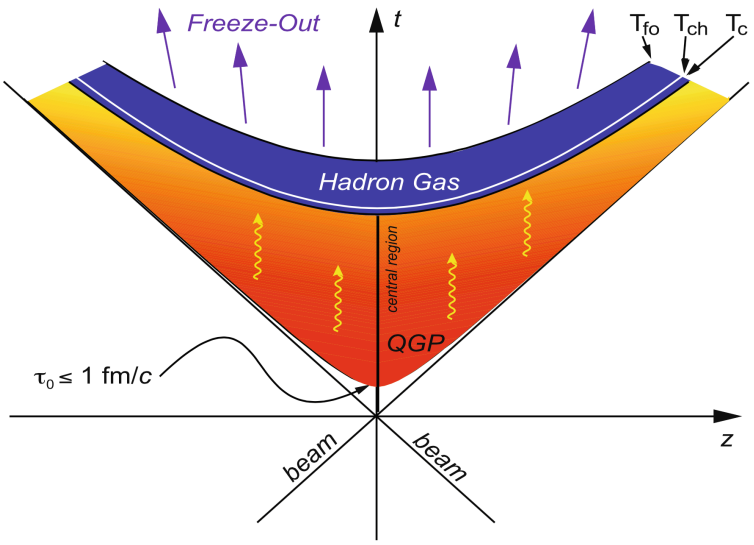

Figure 1.3: The various stages of a relativistic heavy-ion collision as a function of the time t and the spatial expansion z [16].

1.3 Relativistic Heavy-Ion Collisions

In relativistic heavy-ion collisions performed at high-energy collider experiments at RHIC and the LHC the medium which is formed in the collision zone undergoes various stages. Figure 1.3 shows the evolution of such a collision process as a function of time and spatial expansion. In the very early stages of the collision ($\tau \leq 1\,\mathrm{fm}/c$) hard particles with large masses or large transverse momenta ($p_\mathrm{T} > 1\,\mathrm{GeV}/c$) are created along with the bulk of soft particles. They start to rescatter off each other elastically and inelastically and form a dense, strongly interacting medium which becomes a QGP if it thermalizes and has an energy density bigger than ϵ_c. Because of the thermal pressure of the medium acting against the surrounding vacuum, the collision fireball expands and cools down while the energy density decreases ($1\,\mathrm{fm}/c < \tau < 15\,\mathrm{fm}/c$). When the system reaches the critical temperature of the phase transition T_c the quarks and gluons hadronize. The expansion of the system continues and the hadrons rescatter inelastically until the distance between them exceeds the range of the strong interaction at the *chemical freeze-out* temperature T_{ch} ($\tau > 10$–$15\,\mathrm{fm}/c$), which happens right after hadronization. The particle abundances do not change anymore but elastic scattering continues until the system freezes out kinetically at the *thermal freeze-out* temperature T_{fo} and the particle momenta are fixed. The particles then stream freely to the detector.

In order to extract information about the QGP formed in heavy-ion collisions, several observables can be used which are classified into *early* and *late* signatures originating from different stages of the collision. Directly produced real and virtual photons are early signatures. They are emitted throughout the expansion process of the system but their production rate is strongly shifted towards the early collision stages.

Since photons do not interact strongly they can escape the collision zone without reinteracting and carry important information about their parent particles. Other early probes are the charm quarks which are produced early in the collision by hard processes. The $c\bar{c}$ pairs travel through the medium and rescatter with other colored particles during all the stages of the fireball evolution, giving valuable information about the medium density. Along their path they are Debye screened from each other by other quarks and gluons in the QGP which keeps them from hadronizing into one of the charmonium states. This results in a J/ψ suppression compared to pp collisions. At LHC energies the charm production is large and the statistical recombination of $c\bar{c}$ pairs [17, 18] into charmonia partially compensates the initial suppression [19]. Late QGP signatures are hadrons made of the three light quarks (u, d, s) which can be thermally produced and decay very easily throughout all of the expansion stages. They account for a very large fraction of the particle production and can be measured with high precision [15].

2 ALICE - A Large Ion Collider Experiment

ALICE (A Large Ion Collider Experiment) is the dedicated heavy-ion experiment at the CERN LHC [20]. It aims to explore the structure of the QCD phase diagram and properties of the QGP phase at vanishing baryochemical potential and high temperature. Comprehensive studies address equilibrium and non-equilibrium physics of strongly interacting matter at extreme energy densities, the role of chiral symmetry in the generation of mass, physics of parton densities at phase-space saturation and their collective dynamical evolution towards hadronization in a dense nuclear environment [21, 22].

In order to achieve the physics goals of the experiment, the ALICE detector system (Figure 2.1) has to be capable of tracking and identifying particles in a large transverse momentum range ($0.1\,\mathrm{GeV}/c < p_\mathrm{T} < 100\,\mathrm{GeV}/c$) and reconstructing short-lived particles. The unique detector design allows to perform those tasks in a high-multiplicity environment of up to $\mathrm{d}N/\mathrm{d}\eta = 8000$ at mid-rapidity at the LHC design energy of $\sqrt{s_\mathrm{NN}} = 5.5\,\mathrm{TeV}$ for Pb-Pb collisions. The large acceptance of the detector enables the detection of the decay products of low-momentum particles and the study of particle ratios, p_T spectra and HBT (Hanbury-Brown-Twiss) correlations on an event-by-event basis. A short description of ALICE and its sub-detectors is given in Section 2.2.

The ALICE heavy-ion program started with Pb-Pb collisions at $\sqrt{s_\mathrm{NN}} = 2.76\,\mathrm{TeV}$ in 2010 and 2011 during LHC Run 1, accumulating an integrated luminosity of $\mathscr{L}_{int} = 0.16\,\mathrm{nb}^{-1}$. Further Pb-Pb data will be taken during Run 2 starting in 2015, concluding with $\mathscr{L}_{int} = 1\,\mathrm{nb}^{-1}$ according to expectations. After its Long Shutdown 2 (LS2), the LHC will increase its luminosity during Run 3, starting in 2020, to reach an interaction rate of 50 kHz and an integrated luminosity of $\mathscr{L}_{int} = 10\,\mathrm{nb}^{-1}$. To make use of this large amount of heavy-ion collision data, the ALICE detector, including the sub-detectors, readout electronics and data acquisition system, will undergo a major upgrade to improve the detector performance and to record all of the events with a continuous readout scheme [24]. In addition to nucleus-nucleus (AA) collisions, the physics program of ALICE also includes

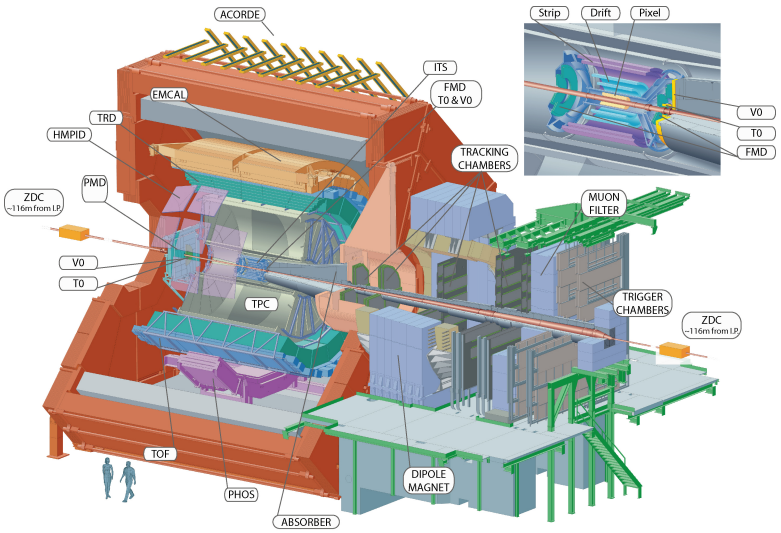

Figure 2.1: A schematic drawing of the ALICE detector system [23].

proton-nucleus (pA) and proton-proton (pp) collisions which serve as reference data and complement the studies of the dedicated pp experiments at the LHC.

2.1 Coordinate Systems

2.1.1 Global Coordinate System

The global ALICE coordinate system is a right-handed orthogonal Cartesian system with its origin at the nominal interaction point [25]. A sketch of the global ALICE coordinate system is given in Figure 2.2a. The z-axis is parallel to the beam direction and points away from the muon spectrometer. The side of the detector with positive z is labeled A-Side or Shaft-Side, the one with negative z is called C-Side or Muon-Side. The x-axis is aligned with the local horizontal plane and points towards the accelerator center while the y-axis points upwards. The azimuthal angle φ increases counterclockwise from the x-axis ($\varphi = 0$) to the y-axis ($\varphi = \pi/2$) with the observer standing on the A-Side and looking to the C-Side. The polar angle θ increases from positive z ($\theta = 0$) to the x-y plane ($\theta = \pi/2$) to negative z ($\theta = \pi$).

2.1.2 Local Coordinate System

The offline reconstruction software of the ALICE central tracking detectors (ITS, TPC, TRD) shares a common local coordinate system related to a given sub-detector (ITS module, TPC sector) [22]. A sketch of the local coordinate system is shown in Figure 2.2b. The local coordinate system is also a right-handed Cartesian system and uses the same point of origin and z-axis as the global coordinate system. The local x-axis is perpendicular to the sensitive plane of the sub-detector (ITS ladder, TPC pad row). Therefore, the transformations from the local coordinate systems to the global one are single rotations around the z-axis.

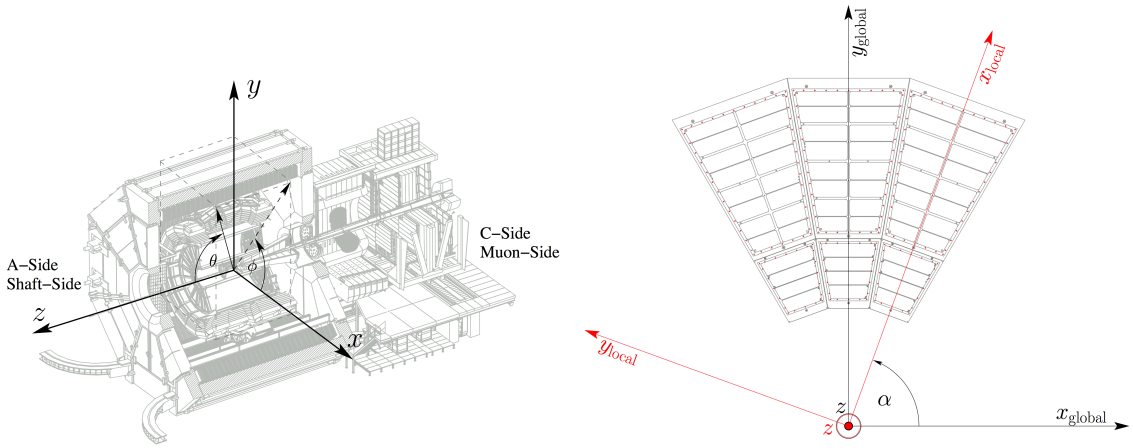

(a) (b)

Figure 2.2: A sketch of (a) the global ALICE coordinate system and (b) the local coordinate system [26].

2.2 Detectors

The ALICE detector system can be divided into three groups. Enclosed by the L3 solenoid magnet, the complex array of central detectors is designed to detect and identify hadrons, electrons and photons in the pseudorapidity region of $|\eta| < 0.9$. The central part consists of the central barrel detectors with full azimuthal coverage and several single-arm detectors covering a fraction of the central barrel phase space. Muons are detected and identified by the muon spectrometer with a pseudorapidity coverage of $-4.0 < \eta < -2.5$. Additional detectors positioned at forward rapidity are used for event characterization and triggering and cover a wide range of $-3.4 < \eta < 5.0$ [27].

2.2.1 Central Detectors

The Inner Tracking System (ITS) consists of 6 cylindrical layers which are positioned at radii between 4 and 43 cm around the nominal interaction vertex. The two innermost layers are equipped with Silicon Pixel Detectors (SPD), the following two layers with Silicon Drift Detectors (SDD) and the two outermost layers with Silicon Strip Detectors (SSD). Having an analogue readout, the four outer layers can perform particle tracking and identification via $\mathrm{d}E/\mathrm{d}x$ measurement. With a spatial resolution of the order of tens of μm, ITS detectors provide a primary vertex resolution better than 60 μm for $p_{\mathrm{T}} > 1\,\mathrm{GeV}/c$ depending on the multiplicity. Other tasks are the reconstruction of secondary vertices and the improvement of the momentum and angle resolution of particles reconstructed by the Time Projection Chamber.

The Time Projection Chamber (TPC) is the main tracking device in the central barrel. Together with the other tracking detectors, the TPC provides particle identification, charged particle momentum measurement and vertex determination with sufficient energy and momentum resolution and two track separation. It has a cylindrical shape with a length of 5 m and an active area with an inner radius of 85 cm and an outer radius of 245 cm. The cylinder is divided into two drift regions by the central electrode and the endplates are equipped with Multiwire Proportional Chambers (MWPC). A detailed description of the TPC is given in Chapter 3.

The Transition Radiation Detector (TRD) is designed to identify electrons with momenta above 1 GeV/c and separate them from pions by exploiting the transition radiation (TR) from electrons which pass the radiator. The TRD has an active length of 7 m and six layers in radial direction (2.9 m $< r <$ 3.68 m). Each detector module consists of 48 mm of composite radiator material, a 30 mm drift region and a MWPC (7 mm) with pad readout. The TR photons are efficiently converted using Xe as a counting gas mixed with 15 % of CO_2. The TRD also contributes to the global tracking and serves as a trigger for high-momentum particles.

The Time-Of-Flight (TOF) detector is used to identify particles in the intermediate momentum range, especially pions, kaons and protons. It covers the full azimuth, has a length of 7.41 m in z direction (active area) and a radial position of 370 cm $< r <$ 399 cm. The TOF employs a Multi-gap Resistive-Plate Chamber (MRPC) technology as each module consists of a group of 10-gap double stack MRPC strips with an intrinsic time resolution better than 40 ps.

The tasks of the High-Momentum Particle Identification Detector (HMPID) are to identify light nuclei and anti-nuclei at high transverse momenta and charged hadrons beyond the attainable momentum ranges of the ITS, TPC and TOF. As a single-arm detector, the HMPID covers 5 % of the central barrel acceptance at a radius of 5 m and is based on proximity-focusing Ring Imaging Cherenkov (RICH) counters.

The Photon Spectrometer (PHOS) is a single-arm electromagnetic spectrometer covering a pseudorapidity range of $|\eta| < 0.12$ and $\Delta\phi < 100\,^\circ$ in azimuth at a radius of 4.6 m. It consists of a highly segmented electromagnetic calorimeter and a Charged-Particle Veto (CPV) detector. With its high energy resolution and granularity, PHOS enables measurements of low-p_{T} direct photons, high-p_{T} π^0 and γ-jet correlations to extract thermal and dynamical properties from the initial phase of the collision and to study jet quenching.

The Electromagnetic Calorimeter (EMCal) provides a fast and efficient trigger for hard jets, photons and electrons and can measure the neutral energy component of jets. Therefore, it enables full jet reconstruction and a detailed study of jet quenching. The large Pb-scintillator sampling calorimeter is positioned at a radius of 4.5 m approximately opposite to PHOS and has a coverage of $|\eta| < 0.7$ in pseudorapidity and of 107 ° in ϕ.

The ALICE Cosmic Ray Detector (ACORDE) is placed on the upper surface of the L3 magnet and consists of 60 modules of plastic scintillators. The main tasks of ACORDE are to provide a fast trigger signal for the commissioning, calibration and alignment of the central barrel detectors and to detect atmospheric muons together with the TPC, TRD and TOF for the study of high-energy cosmic rays.

2.2.2 Muon Spectrometer

In order to study heavy-flavor production, the complete spectrum of heavy-quark vector-meson resonances in the $\mu^+\mu^-$ decay channel is measured by the muon spectrometer, as well as the unlike-sign dimuon continuum up to masses of $10\,\mathrm{GeV}/c^2$. The muon tracking system consists of five detection stations. Each station is equipped with two layers of high-granularity cathode pad chambers with a spatial resolution of the order of 70 μm. The middle station is located inside a large dipole magnet. A passive front absorber is placed in front of the tracking system to shield the detection planes from hadrons and photons coming from the interaction vertex. Following the tracking stations, a second passive absorber, the muon filter, provides additional protection for the four layers of the trigger detector.

2.2.3 Forward Detectors

The Zero-Degree Calorimeters (ZDC) measure the energy carried in forward direction by the spectator nucleons in AA collisions. This information gives an estimate of the number of participants and the collision geometry and is used to provide a centrality trigger. Two sets of hadronic ZDCs are located at 112.5 m on each side of the interaction point, while each set consists of two quartz fibers sampling calorimeters. One of them detects spectator neutrons (ZN), the other one spectator protons (ZP) which are separated from the neutrons by the magnetic elements of the LHC beam line. Two electromagnetic calorimeters (ZEM) complement the hadronic ZDCs by measuring the energy of particles at forward rapidity, which increases with the collision centrality. Therefore, central collisions can be distinguished from very peripheral ones. The ZEMs are placed 7 m from the interaction point on both sides of the beam pipe opposite to the muon spectrometer and cover a pseudorapidity range of $4.8 < \eta < 5.7$.

The Photon Multiplicity Detector (PMD) provides estimates of the transverse electromagnetic energy and the reaction plane by measuring the multiplicity and spatial (η-ϕ) distribution of photons in the pseudorapidity region of $2.3 < \eta < 3.7$. Employing the preshower method, the PMD consists of two planes of highly granular gas proportional counters with a three radiation length thick converter in between. The detector plane in front of the converter is used as a CPV detector while the second detector plane provides photon identification.

The Forward Multiplicity Detector (FMD) measures the charged particle multiplicity in the pseudorapidity range of $-3.4 < \eta < -1.7$ and $1.7 < \eta < 5.0$ and enables the study of multiplicity fluctuations and the determination of the reaction plane on an event-by-event basis. There is one FMD detector, consisting of an inner and outer ring, placed on each side of the ITS and a third FMD ring placed further from the interaction point at 3.2 m. The detector ring design is based on silicon sensors with high radial and azimuthal segmentation.

The V0 detector consists of two arrays (V0A and V0C) of scintillator counters. The V0A is located 3.4 m from the interaction point opposite to the muon spectrometer and covers a region of $2.8 < \eta < 5.1$ in pseudorapidity. The V0C is fixed to the front of the absorber 90 cm from the interaction point and covers a pseudorapidity range of $-3.7 < \eta < -1.7$. The V0 detector provides minimum-bias triggers for the central barrel detectors as well as multiplicity, semi-central and central triggers.

The T0 detector is designed to generate a start time for the TOF detector, to measure the vertex position followed by a trigger signal if it is within the preset limits and to provide minimum-bias and multiplicity triggers. The detector consists of two Cherenkov counter arrays called T0A and T0C. T0A is located 3.75 m from the interaction point opposite to the muon spectrometer and T0C is placed in front of the muon absorber 72.7 cm from the interaction point. The two detectors have pseudorapidity coverages of $4.61 < \eta < 4.92$ (T0A) and $-3.28 < \eta < 2.97$ (T0C) respectively.

3 The ALICE Time Projection Chamber

The Time Projection Chamber [28] is the main tracking device in the ALICE central barrel. It is designed to operate at charged-particle multiplicities of up to $\mathrm{d}N_{ch}/\mathrm{d}y = 8000$ in central Pb-Pb collisions at $\sqrt{s_{\mathrm{NN}}} = 5.5\,\mathrm{TeV}$ center-of-mass energy. This translates into 20 000 tracks within the TPC acceptance which covers 2π in azimuth and $|\eta| < 0.9$ in pseudorapidity. In such a high-multiplicity environment, the TPC provides charged-particle tracking and identification by measuring the specific energy loss ($\mathrm{d}E/\mathrm{d}x$) and the particle momentum. The achieved energy loss resolution is better than 8 % while the momentum resolution is better than 7 % for momenta of $10\,\mathrm{GeV}/c$. Furthermore the TPC aims for a two-track resolution in relative momentum below $5\,\mathrm{MeV}/c$, a track finding efficiency of $\sim 90\,\%$ as well as a $\sim 90\,\%$ track matching efficiency with the other detectors [29].

A schematic of the TPC layout is shown in Figure 3.1. The TPC consists of a cylindrical *field cage* with an active gas volume of $88\,\mathrm{m}^3$ which is divided into two *drift regions* of 250 cm length each by the *central electrode* (CE). A high-voltage of 100 kV at the CE and a fine segmentation of the field cage walls into 165 *field strips* with systematically decreasing potentials result in a highly uniform axial drift field of 400 V/cm with distortions in the range of 10^{-4}. During LHC Run 1 both Ne-CO_2 (90-10) and Ne-CO_2-N_2 (90-10-5) were used as the detector gas. For Run 2 Ne is replaced by Ar as the main gas component, employing a gas composition of Ar-CO_2 (88-12). The readout chambers are based on MWPCs with *cathode pad* readout and are mounted into the *endplates* at both ends of the cylinder. The active readout area has an inner radius of 85 cm and an outer radius of 247 cm and is segmented in radial (x_{local}) and $r\varphi$ (y_{local}) direction. A high spatial granularity is achieved by a total number of 557 568 pads which are read out by the *front-end electronics* (FEE) and readout chain capable of handling signal occupancies of up to 50 %. Specifications of the main TPC parts are given in more detail in Section 3.1.

The TPC is able to perform a full three-dimensional reconstruction of particle trajectories. When a charged particle traverses the active detector volume it *ionizes* a specific number of gas molecules along its path. The ionization electrons drift

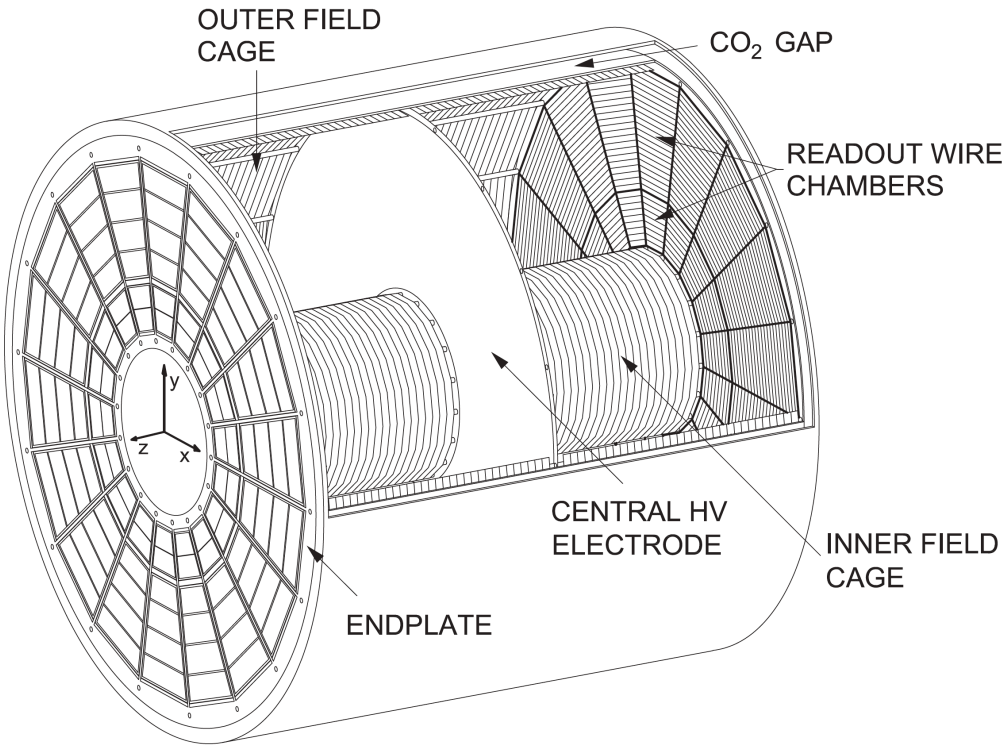

Figure 3.1: A view of the TPC field cage together with the central electrode and the endplates holding the readout chambers [29].

towards the readout chambers with a constant mean *drift velocity* along the electric field produced by the CE and the field cage. Entering the *amplification region* of the MWPCs, the ionization electrons are multiplied via *gas amplification* and the induced signals are measured on the cathode pads of the pad plane, yielding a two dimensional projection of the particle trajectory. The wire geometry and pad sizes are chosen such that the produced charge spreads over three adjacent pads, which enables a position resolution much better than the actual pad size by determining the center of gravity of the charge distribution. This information together with the *drift time* which is determined by sampling the time distribution of each pad signal is called a *cluster* [28]. The original coordinate of the ionization is then calculated as a three dimensional *space point* by a reconstruction software. Afterwards a *tracking* algorithm reconstructs the particle trajectory by combining the space points to one *track* [26]. The particle is identified by means of its momentum and its *mean specific energy loss* $\langle \mathrm{d}E/\mathrm{d}x \rangle$ in the detector gas. The transverse momentum of charged particles can be extracted from the radius of the curvature of their trajectory in a magnetic field which has a magnitude of 0.5 T and is parallel to the electric field. The total momentum is calculated after fitting the trajectory with a helix shape. The mean specific energy loss is obtained from the number of clusters assigned to the track and the truncated mean of either the maximum (Q_{max}) or the total charge (Q_{tot}) of the clusters [29]. The fundamental physics processes which are relevant for the TPC operation are qualitatively described in Section 3.3.

3.1 Detector Design

3.1.1 Gas Choice

The choice of the gas mixture and its stability and purity are crucial for the detector performance. It influences the charge transport in the drift volume and the amplification process in the readout chambers. Therefore, the choice of gas composition is constrained by the performance requirements and has substantial implications for the design of the gas system [29].

The detector gas ideally provides a large energy loss, high electron drift velocity and low diffusion coefficients, a high Townsend coefficient, a low attachment coefficient and a high ion mobility [30]. These requirements are met to a large extent by the noble gases of Ne and Ar. Comparing both gases, less ionization in Ne results in less primary statistics of electrons. On the other hand, Ar has a lower ion mobility which can lead to an accumulation of positive charge inside the drift volume and to undesired drift field distortions. To absorb photons originating from ionization processes a certain amount of a quencher gas is added to the noble gas with CO_2 being the quencher of choice.

For the RUN 1 operation of the TPC, Ne-CO_2 (90-10) has been chosen to avoid drift field distortions caused by space-charge. At the maximum drift field of 400 V/cm allowed by the design of the field cage, this mixture provides an electron drift velocity resulting in drift times below 100 μs and diffusion coefficients that match the requirements for the desired spatial resolution. Because of the relatively low primary ionization of Ne, the MWPCs have to be operated at high gains near 10^4. Adding 5 % of N_2 to the mixture leads to a more stable operation of the readout chambers under such conditions reducing the probability of self-sustained glow discharges [31].

For RUN 2 the detector gas has been changed to Ar-CO_2 (88-12) to further improve the stability of the readout chambers considering the higher interaction rates. The electron drift velocity and diffusion coefficients at 400 V/cm are comparable to the ones of the Ne-based mixtures.

To ensure the desired detector performance, the gas and cooling systems of the TPC precisely monitor and control the conditions inside the gas volume. The temperature dependence of the drift velocity of the gas mixtures requires a temperature uniformity of 0.1 K. Furthermore the drift velocity strongly depends on the CO_2 concentration calling for an accurate measurement of the gas composition. The gas is recirculated to avoid a waste of the main gas and to filter out impurities like oxygen and water with a Cu-catalyzer purifier.

3.1.2 Field Cage

The mechanical structure of the TPC consists of four cylinders, an inner and outer *containment vessel* and an inner and outer *field cage vessel*, all made of composite material. The field cage vessels are surrounded by the containment vessels which ensure the gas tightness of the system and serve as grounded enclosures at the inner and outer diameters of the TPC. The gaps between the field cage and containment vessels are continuously flushed with CO_2 to insulate the field cage voltage from the grounded walls of the containment vessels. The cylinder is divided by the central electrode made of a stretched 23 μm thick aluminized mylar foil. The field cage is segmented into 165 aluminized mylar strips on each side to provide a uniform electrostatic drift field. The field strips are 25 μm thick, 13 mm wide and have a pitch of 15 mm leaving a 2 mm gap between two strips. They are stretched around a set of 18 regularly spaced Makrolon® *rods* which are positioned on the internal walls of the inner and outer field cage vessels, respectively. On both sides of the field cage, one of the inner and one of the outer rods, called *resistor rods*, contain the voltage dividers which are chains of resistors defining the potential on each field strip. Six of the outer rods per side are used for the TPC laser calibration system [32] as well as, together with 10 more outer and 17 inner rods, for the circulation of the gas which flows radially through the system. The two endplates close the field cage vessels and hold the readout chambers in position.

3.1.3 Readout Chambers

The readout chambers of the ALICE TPC are based on conventional multiwire proportional chambers with cathode pad readout. Their design has been optimized in terms of momentum and $\mathrm{d}E/\mathrm{d}x$ resolution for the operation in an environment of high particle densities in central Pb-Pb collisions.

The readout plane is segmented in azimuth into 18 trapezoidal *sectors* which is common with the subsequent ALICE detectors (TRD, TOF). An additional radial segmentation into inner and outer readout chambers (IROCs and OROCs) meets the different requirements for the ROCs as a function of the radius originating in the radial dependence of the track density. A numbering scheme (0–71) in the offline code of the ALICE analysis software gives each readout chamber its own number as shown in Figure 3.2. The IROCs are labeled from 0 to 35 and the OROCs from 36 to 71, always starting with the ROCs on the A-Side [33]. The dead space between two adjacent chambers has been minimized to 27 mm, the radial length of the active readout area varies from 84.8 cm to 132.1 cm for the IROCs and from 134.6 cm to 246.6 cm for the OROCs. This results in a total active area of 32.5 m^2. The four main components of a readout chamber are the wire planes, the pad plane, an ad-

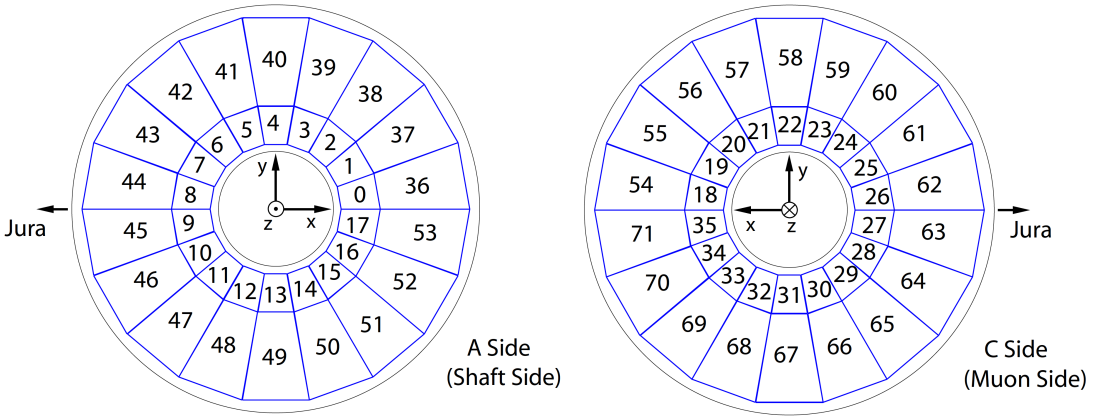

Figure 3.2: The numbering scheme for the TPC readout chambers used in the offline code of the ALICE analysis software [33].

ditional 3 mm Stesalit insulation plate and an aluminum frame.

A scheme of three wire planes is used for the readout chambers consisting of an anode wire plane above the pad plane, a cathode wire plane and a gating grid (GG). Different wire geometries are employed for IROCs and OROCs as shown in Figure 3.3. The gap between the anode wires and the pad plane is 2 mm for the IROCs and 3 mm for the OROCs as is the gap between the anode wires and the cathode wires. The gap between the cathode wires and the gating grid is 3 mm for both types of readout chambers. The anode wires and gating grid wires are staggered with respect to the cathode wires. All wires run in azimuthal direction and their length given by the detector layout varies from 27 cm to 44 cm for the inner and 45 cm to 84 cm for the outer chambers.

Gas amplification happens in the vicinity of the anode wires when they are set to a sufficiently high potential. Since the amplification factor increases with decreasing anode wire diameter, 20 μm thick gold-plated tungsten wires are used. Choosing a pitch of 2.5 mm between two anode wires, the accumulated charge per unit length of the anode wires is minimized to avoid rate-induced gain variations.

The 75 μm thick cathode wires are made of an alloy of copper and beryllium and separate the amplification region from the drift volume. Having a pitch of 2.5 mm the cathode wires collect a large fraction of the ions produced during gas amplification without reducing the transparency for ionization electrons coming from the drift region.

The same wires as for the cathode wire plane are used for the gating grid wires. In the open state the gating grid wires are set to a constant negative *offset voltage* V_G to provide full transparency to ionization electrons. In the closed state an additional

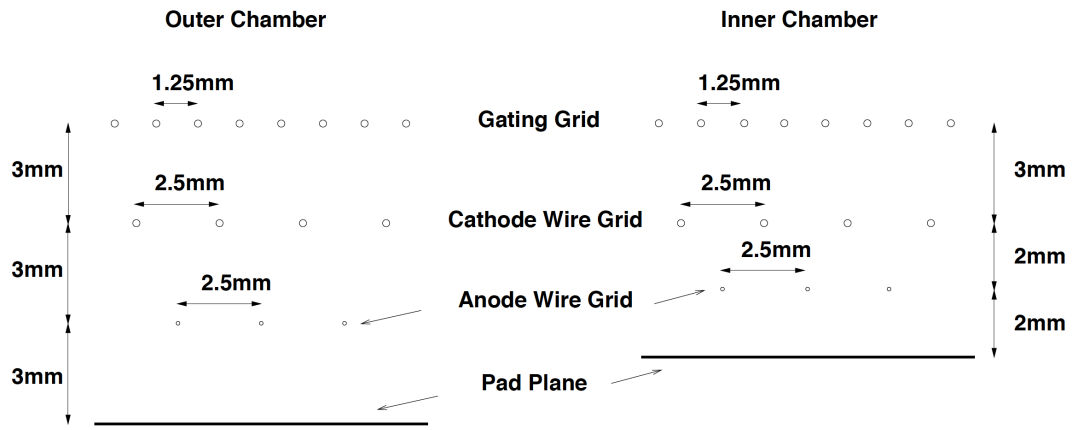

Figure 3.3: The wire geometries of the ALICE TPC inner (right) and outer (left) readout chambers [28].

	Pad size ($r\varphi \times r$)	Number of rows	Number of pads
IROC	$4 \times 7.5\,\mathrm{mm}^2$	63	5504
OROC medium	$6 \times 10\,\mathrm{mm}^2$	64	5952
OROC long	$6 \times 15\,\mathrm{mm}^2$	32	4032
TPC sector		159	15 488
TPC total			557 568

Table 3.1: The three different readout pad geometries, the total number of rows and pads for each pad size in one TPC sector and the total number of readout pads in the TPC [29].

bipolar potential $\pm\Delta V$ (*gating voltage*) is applied. Then the gating grid is no longer transparent for electrons from the drift region to protect the amplification region against unwanted ionization and it prevents the back-drifting ions from the amplification region to enter the drift volume which would cause significant distortions of the drift field. By default the gating grid is operated in the closed state and is only opened when a trigger signal is received. The opening time is defined by the electron drift time for the full drift length of the TPC. The pitch of the gating grid wires is 1.25 mm to keep the gating voltage reasonably low.

A halogen-free FR4 printed circuit board is employed as the pad plane. The pad plane design is optimized for signal-to-noise ratio and position resolution. It is segmented into a total of 159 *pad rows* in radial direction, each pad row providing a high granularity in rφ by a fine segmentation into single pads. The pad size increases in two steps with the radius according to the particle density. A summary of the adopted pad geometries is given in Table 3.1.

The mechanical stability of the readout chambers is provided by the aluminum frame. Reinforcing stiffening ribs prevent a deformation caused by gravitational forces and wire tension.

3.1.4 Front-End Electronics and Readout

Electrons and ions produced during gas amplification induce a positive current signal on the pad plane. The signal is characterized by a fast rise time of $< 1\,\text{ns}$ and a long complex tail of the order of $50\,\mu\text{s}$ due to the movement of the positive ions [29].

The cathode pads are read out by front-end cards (FEC) which are connected to the pad plane via flexible Kapton cables. The main components for signal transformation, processing and storage on the FEC are the PASA (Preamplifier Shaper) chip and the ALTRO (ALICE TPC readout) chip. The PASA chip is based on a charge-sensitive amplifier followed by a semi-Gaussian pulse shaper. It contains 16 channels, has a conversion gain of $12\,\text{mV/fC}$ and a dynamic range of $2\,\text{V}$. The differential semi-Gaussian voltage signals from the PASA are fed into the ALTRO chip where they are digitized by a 10-bit 25 MSPS (mega samples per second) ADC (analog-to-digital converter) operated at a sampling rate of $10\,\text{MHz}$. The digitized signals are processed by a set of circuits performing baseline subtraction, tail cancellation, zero-suppression and formatting and are stored in a multiple-event buffer (MEB). Depending on the received trigger, the stored event data is either discarded and overwritten by the next event or frozen in memory until its complete readout takes place. Each FEC accommodates eight PASAs and eight ALTRO chips resulting in 128 channels. The total of 4356 FECs are linked to 216 Readout Control Units (RCU) which provide an interface to the Data Acquisition (DAQ), Central Trigger Processor (CTP) and Detector Control System (DCS) [34].

3.2 Upgrade

In Run 3 (2020) the LHC luminosity for heavy ions is expected to increase significantly with interaction rates of about $50\,\text{kHz}$ which will enhance the sensitivity to a number of key observables characterizing the QGP. During LS2 (2019–2020), the MWPCs will be replaced by a continuous readout scheme based on GEMs (Gas Electron Multiplier) with a newly developed front-end electronics and readout system to match the future LHC interaction rates while retaining the current tracking and particle identification performance [35].

The gating grid of the MWPCs prevents an accumulation of positive ions from the amplification region inside the TPC drift volume which would cause significant distortions of the drift field. The operation of the gating grid of the MWPCs introduces an intrinsic dead time of the TPC leading to a rate limitation of the order of 1–3 kHz depending on the gas mixture. Because of the insufficient intrinsic ion blocking capability of the MWPCs, an operation without gating grid implies excessive drift field distortions which make precise space point measurements impossible.

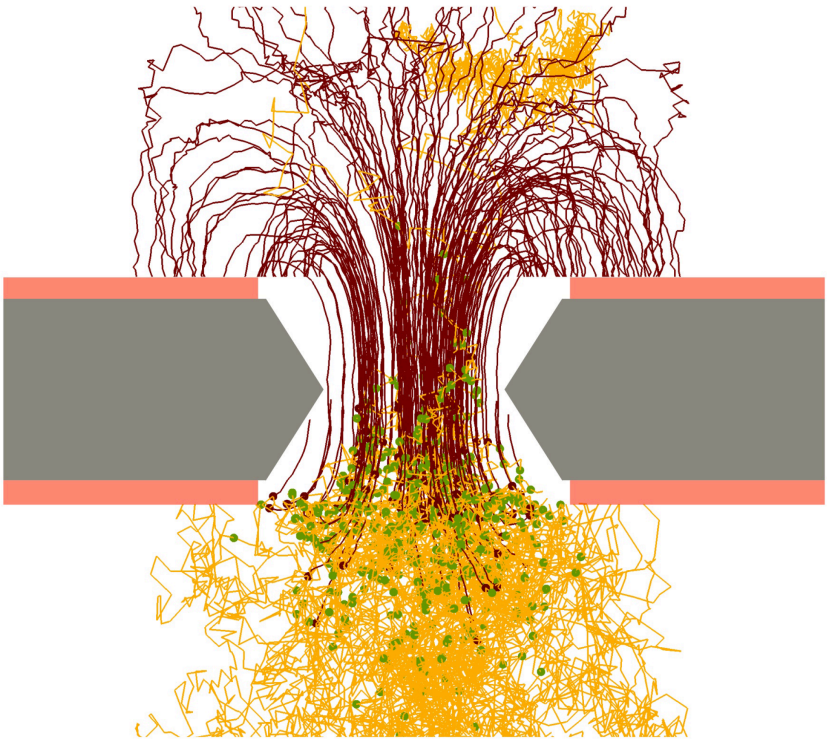

Figure 3.4: Garfield/Magboltz simulation of two avalanche processes inside a GEM hole. Two electrons (yellow lines) enter the amplification region and are multiplied. The positive ions (red lines) created in this process drift in the opposite direction closely following the electric field lines [35].

The upgraded readout chambers will be based on stacks of four GEM foils. A GEM foil consists of a 50 μm thin insulating Polyimid foil with Cu-coated surfaces. The foil is perforated to form a dense regular pattern of double-conical holes with an inner diameter of $\sim 50\,\mu$m and an outer diameter of $\sim 70\,\mu$m. The GEM holes serve as amplification structures and provide charge transport. Applying a moderate voltage difference of 200–400 V between the Cu layers, the electric field strength inside the GEM holes is sufficiently large for gas amplification. The complicated dynamics of charge movement and avalanche creation inside a GEM hole is illustrated in Figure 3.4. The positive ions created during the gas amplification process closely follow the electric field lines because of their small diffusion. Most of the ions end up on the top layer of the GEM since the electric field inside the hole is much higher than the one above the hole. A fraction of ions escapes into the region above the GEM foil. Using a combination of four GEM foils with different hole pitches for the upgrade of the TPC readout chambers, an *ion backflow* (IBF) of the order of 1 % is achieved. To minimize the space-charge density inside the drift volume due to the back-drifting ions, the gas composition will be changed to Ne-CO_2-N_2 (90-10-5) because of the higher ion mobility of the Ne^+ and $CO_2{}^+$ ions in this mixture and the smaller primary ionization of Ne compared to Ar. The resulting drift field distortion are well within acceptable limits and can be sufficiently corrected [35, 36].

3.3 Physics Principles

3.3.1 Gas Ionization and Energy Loss

Charged particles traversing the active gas volume of the detector leave a track of ionization along their trajectory. There are two different ionization mechanisms. *Primary ionization* describes collisions of a fast charged particle with a gas atom in which one or more high-energy electrons are knocked out of the gas atom. Most of the charge along a track is created by *secondary ionization* of gas atoms not encountered by the fast charged particle. In this case, the ionizing particles are the high-energy electrons or intermediate excited states of the gas atoms. One example involving the latter is the *Penning Effect* which contributes significantly to the ionization process in gas mixtures of noble gases and quenchers. If the excitation energy of a metastable state of the noble gas is higher than the ionization potential of the quencher, excited noble gas atoms can ionize the quencher molecules.

The sum of the primary and secondary ionization electrons per primary collision is called a *cluster*. The size of a cluster is determined by the cluster-size distribution which is a probability distribution with a very long tail leading to a small but finite probability of cluster sizes of the oder of 1000 electrons. The cluster-size distribution describes the amount of total ionization per track length when the number of primary collisions is known. The resulting ionization distribution develops a peak which defines the *most probable value* (MPV) and is significantly different from the mean value due to the long tail of the cluster-size distribution.

The energy spent on ionization accounts only for a fraction of the total energy loss of the fast charged particle. The total ionization is characterized by the energy W which is spent on average on the creation of one free electron:

$$W \langle N_\mathrm{t} \rangle = L \left\langle \frac{\mathrm{d}E}{\mathrm{d}x} \right\rangle \ . \tag{3.1}$$

$\langle N_\mathrm{t} \rangle$ is the average total number of ionization electrons created along the trajectory of length L and $\langle \mathrm{d}E/\mathrm{d}x \rangle$ is the mean total energy loss per unit path length of the fast charged particle [37].

The total energy loss of the traveling particle, i.e. the integral over all energies lost to the individual gas atoms, is given by the Bethe-Bloch formula. It includes high-energy transfers up to the kinematic limit which is different for electrons compared to heavier particles because they have a much smaller mass, they are identical with their collision partner and they have a different spectrum of transferred energy. To be applicable for the track ionization in drift chambers like the TPC, the Bethe-

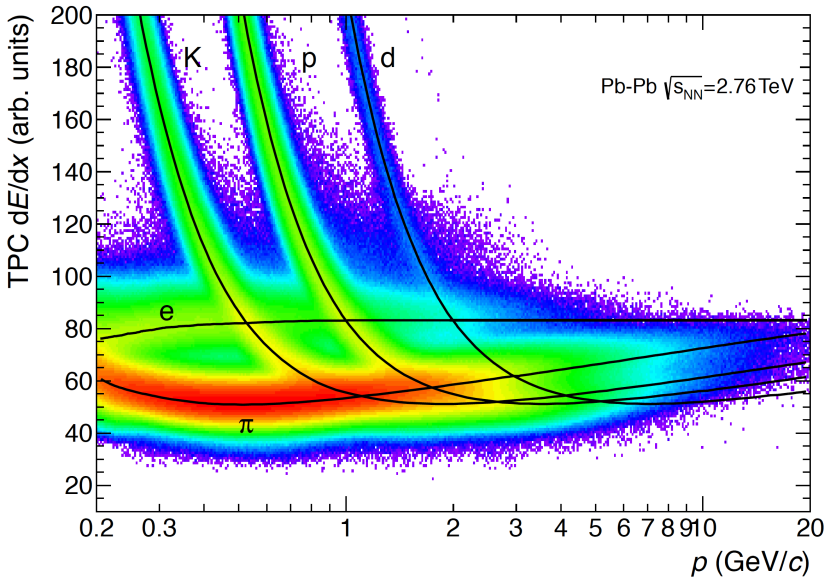

Figure 3.5: A measurement of the specific energy loss per unit path length $\mathrm{d}E/\mathrm{d}x$ of electrons, pions, kaons, protons and deuterons as a function of the particle momentum p in the ALICE TPC. The lines show the parametrization of the expected mean energy loss [38].

Bloch equation is modified with a cut-off energy $E_{\max}$ which replaces the kinematic limit and depends on the detector. The *restricted* energy loss per unit path length is then calculated by

$$\left(\frac{\mathrm{d}E}{\mathrm{d}x}\right)_{\text{restricted}} = \frac{4\pi N e^4}{mc^2}\frac{1}{\beta^2}z^2\left[ln\frac{\sqrt{2mc^2E_{\max}}\beta\gamma}{I} - \frac{\beta^2}{2} - \frac{\delta(\beta)}{2}\right], \tag{3.2}$$

where mc^2 is the rest energy of the electron, z is the charge of the traveling particle, N is the number density of electrons in the traversed matter, e is the elementary charge, I is the mean excitation energy of the atom, $\beta = v/c$ and $\gamma = 1/\sqrt{1-\beta^2}$. The correction term $\delta(\beta)$ corresponds to the *density effect* of the surrounding polarizable atoms which shield the field of the traveling particle. The restricted energy loss is a universal function depending only on the velocity of the particle and not on its mass or energy. With increasing $\beta\gamma$ the energy loss first decreases with $1/\beta^2$ until it reaches a broad minimum near $\beta\gamma = 4$. Particles in this region are called *minimum ionizing particles* (MIP). For larger $\beta\gamma$ the energy loss increases again in the region of the *relativistic rise*, which is described by the logarithmic term in Equation (3.2), and saturates at the *Fermi plateau* due to the density effect. A measurement of the specific energy loss per unit path length of several particle species as a function of the particle momentum is shown in Figure 3.5.

3.3.2 Drift of Electrons and Ions

Electrons and ions created in ionization processes in the TPC drift volume and the amplification region of the MWPCs move through the gas under the influence of an

electric and a magnetic field. They pick up energy as they are accelerated by the electric field and lose this energy in collisions with the gas atoms. In the case of electrons, they scatter isotropically and randomly having no preferential direction after the collisions because of their small mass. On average, all of the energy they picked up since their last collision is lost in the next collision. Because of the larger masses of ions, they are slower than electrons by about a factor of 10^3 and their momentum is not as randomized as that of electrons. Their drift velocity vector has a significant component in drift direction after collisions. The balance of extra energy picked up and collision losses leads to a constant drift velocity v_D in the direction of the electric field.

Macroscopically, the motion of electrons and ions in an electric and a magnetic field $\mathbf{E}$ and $\mathbf{B}$ is described by the Langevin equation, an equation of motion with friction,

$$m\frac{\mathrm{d}\mathbf{u}}{\mathrm{d}t} = e\mathbf{E} + e\left[\mathbf{u}\times\mathbf{B}\right] - K\mathbf{u}\,, \tag{3.3}$$

where m and e are the mass and the electric charge of the particle, $\mathbf{u}$ is its velocity vector and K corresponds to a frictional force proportional to $\mathbf{u}$ which is caused by the interaction of the particle with the gas [37]. The solution of Equation (3.3) is a steady state with $\mathrm{d}\mathbf{u}/\mathrm{d}t = 0$ resulting in the linear equation

$$\frac{1}{\tau}\mathbf{u} - \frac{e}{m}\left[\mathbf{u}\times\mathbf{B}\right] = \frac{e}{m}\mathbf{E}\,, \tag{3.4}$$

where $\tau = m/K$ has the dimension of a characteristic time and can be associated with the average time between two collisions. The drift velocity vector is obtained by solving Equation (3.4) for $\mathbf{u}$:

$$\mathbf{u} = \frac{e}{m}\tau\left|\mathbf{E}\right|\frac{1}{1+\omega^2\tau^2}\left(\hat{\mathbf{E}} + \omega\tau\left[\hat{\mathbf{E}}\times\hat{\mathbf{B}}\right] + \omega^2\tau^2\left(\hat{\mathbf{E}}\cdot\hat{\mathbf{B}}\right)\hat{\mathbf{B}}\right)\,. \tag{3.5}$$

$\hat{\mathbf{E}}$ and $\hat{\mathbf{B}}$ are the unit vectors of the electric and magnetic field and $\omega = (e/m)\left|\mathbf{B}\right|$ is the cyclotron frequency of the electron. The dimensionless factor $\omega\tau$ determines the drift direction in the presence of a magnetic field.

Without a magnetic field ($\omega\tau = 0$) the drift direction runs along the electric field $\mathbf{E}$ and Equation (3.5) has the form

$$\mathbf{u} = \frac{e}{m}\tau\mathbf{E} = \mu\mathbf{E}\,, \tag{3.6}$$

where the scalar mobility $\mu = (e/m)\,\tau$ is defined as the ratio of drift velocity to electric field in the absence of a magnetic field.

In the case of the TPC, the magnetic field is mostly parallel to the electric field but, because of minor imperfections due to misalignment, there are also small components of $\mathbf{B}$ in the other directions. Using $\mathbf{E} = (0, 0, E_\mathrm{z})$, $\mathbf{B} = (B_\mathrm{x}, B_\mathrm{y}, B_\mathrm{z})$ and $B_\mathrm{x}, B_\mathrm{y} \ll B_\mathrm{z}$, the first order approximation of the ratios of the drift vector components can be expressed as

$$\begin{aligned} \frac{u_\mathrm{x}}{u_\mathrm{z}} &= \frac{-\omega\tau B_\mathrm{y} + \omega^2\tau^2 B_\mathrm{x}}{(1+\omega^2\tau^2)\, B_\mathrm{z}} \,, \\ \frac{u_\mathrm{y}}{u_\mathrm{z}} &= \frac{\omega\tau B_\mathrm{x} + \omega^2\tau^2 B_\mathrm{y}}{(1+\omega^2\tau^2)\, B_\mathrm{z}} \,. \end{aligned} \tag{3.7}$$

For small positive values of $\omega\tau$ the drift direction stays along the electric field whereas for large $\omega\tau$ the drift vector tends to be along $\mathbf{B}$. The imperfections of the $\mathbf{B}$ field lead to a displacement of every track element in x and y direction which is proportional to the drift length L and equal to $\delta_\mathrm{x} = L u_\mathrm{x}/u_\mathrm{z}$ and $\delta_\mathrm{y} = L u_\mathrm{y}/u_\mathrm{z}$.

When the magnetic field is perpendicular to the electric field, i. e. $\left(\hat{\mathbf{E}} \cdot \hat{\mathbf{B}}\right) = 0$, $\mathbf{E} = (E_\mathrm{x}, 0, 0)$ and $\mathbf{B} = (0, 0, B_\mathrm{z})$, the drift direction is given by

$$\begin{aligned} u_\mathrm{x} &= \frac{(e/m)\,\tau}{1+\omega^2\tau^2}\,|\mathbf{E}| \\ u_\mathrm{y} &= -\frac{(e/m)\,\tau}{1+\omega^2\tau^2}\omega\tau\,|\mathbf{E}| \\ u_\mathrm{z} &= 0 \,. \end{aligned} \tag{3.8}$$

Equation (3.8) implies that large $\omega\tau$ turn the drift velocity vector into the $\hat{\mathbf{E}} \times \hat{\mathbf{B}}$ direction. The angle between the drift velocity $\mathbf{u}$ and the electric field $\mathbf{E}$ is defined by the Lorentz angle α_L [39]:

$$\tan\alpha_\mathrm{L} = \frac{u_\mathrm{y}}{u_\mathrm{x}} = -\omega\tau \,. \tag{3.9}$$

Using Equation (3.9), the magnitude of the drift velocity is determined by

$$|\mathbf{u}| = \frac{(e/m)\,\tau}{\sqrt{1+\omega^2\tau^2}}\,|\mathbf{E}| = \frac{e}{m}\tau\,|\mathbf{E}|\cos\alpha_\mathrm{L} \,, \tag{3.10}$$

where $|\mathbf{E}|\cos\alpha_\mathrm{L}$ represents the component of the electric field $\mathbf{E}$ in the drift direction and defines the magnitude of the drift velocity for every magnetic field [37].

In general, the effect of track displacements due to magnetic field components which are not parallel to the electric field is called $\mathbf{E} \times \mathbf{B}$ effect.

Diffusion

Due to the random nature of the collisions with gas atoms the drift velocity of single electrons and ions deviates from the average drift velocity v_{D}. As a result, a point-like cloud of electrons drifting in z direction assumes a Gaussian density distribution after some time t. In the simplest case, the deviation is the same in all three directions which leads to the density distribution

$$n\left(t\right) = \left(\frac{1}{\sqrt{4\pi Dt}}\right)^3 \exp\left(\frac{-r^2}{4Dt}\right) \ , \tag{3.11}$$

where $r^2 = x^2 + y^2 + \left(z - v_{\mathrm{D}}t\right)^2$ and D is the diffusion constant. Since the collision rate of the electrons is a function of the electron energy, the electron mobility is smaller at the leading edge of the cloud than at the center. Therefore, the diffusion in drift direction is different from the one perpendicular to the drift direction. Taking this anisotropy into account, Equation (3.11) changes to

$$n\left(t\right) = \frac{1}{\sqrt{4\pi D_{\mathrm{l}}t}}\left(\frac{1}{\sqrt{4\pi D_{\mathrm{t}}t}}\right)^2 \exp\left[-\frac{x^2+y^2}{4D_{\mathrm{t}}t} - \frac{\left(z - v_{\mathrm{D}}t\right)^2}{4D_{\mathrm{l}}t}\right] \ , \tag{3.12}$$

where D_{l} and D_{t} are the *longitudinal* and *transverse* diffusion constants. The diffusion width σ of the electron cloud after a distance $L = v_{\mathrm{D}}t$ is given by the mean squared deviation of the density distribution:

$$\begin{aligned} \sigma_{\mathrm{l}}^2 &= 2D_{\mathrm{l}}t = \frac{2D_{\mathrm{l}}}{v_{\mathrm{D}}}L = \frac{2D_{\mathrm{l}}}{\mu E}L \ , \\ \sigma_{\mathrm{t}}^2 &= 2D_{\mathrm{t}}t = \frac{2D_{\mathrm{t}}}{v_{\mathrm{D}}}L = \frac{2D_{\mathrm{t}}}{\mu E}L \ . \end{aligned} \tag{3.13}$$

Derived from Equation (3.13), the drift length independent diffusion coefficients D_{L} and D_{T} are often used to characterize the diffusion of electrons in a gas in units of $\mu\mathrm{m}/\sqrt{\mathrm{cm}}$:

$$\begin{aligned} D_{\mathrm{L}} &= \frac{\sigma_{\mathrm{l}}}{\sqrt{L}} = \sqrt{\frac{2D_{\mathrm{l}}}{\mu E}} \ , \\ D_{\mathrm{T}} &= \frac{\sigma_{\mathrm{t}}}{\sqrt{L}} = \sqrt{\frac{2D_{\mathrm{t}}}{\mu E}} \ . \end{aligned} \tag{3.14}$$

3.3.3 Gas Amplification and Generation of the Signal

Ionization electrons created in the drift volume of the TPC drift towards the readout chambers where they induce the measured signal. As they approach one of the anode wires, the electric field $\mathbf{E}$ increases and, in close vicinity to the wire, is given by

$$E\left(r\right) = \frac{\lambda}{2\pi\varepsilon_0}\frac{1}{r} \ , \tag{3.15}$$

where r is the radial distance of the electron from the anode wire and λ is the linear charge density of the wire. When the electric field is sufficiently high ($\mathcal{O}(10^4\,\mathrm{V/cm})$) the electron picks up enough energy for ionization between collisions with the gas atoms and creates another electron-ion pair. An ionization avalanche starts as the process repeats itself for both electrons. The number of electrons multiplies and the avalanche grows until all electrons are collected on the anode wire, which is called gas amplification. There is a lateral extent of the avalanche due to the diffusion of the electrons and the electrostatic repulsion of charges. Therefore, the lateral size of the avalanche depends on the gas composition, the number of charges in the avalanche and their density. The wire diameter influences the azimuthal spread of the avalanche around the wire. The increase of the number of electrons $\mathrm{d}N$ per path $\mathrm{d}s$ is given by

$$\mathrm{d}N = N\alpha \mathrm{d}s \;, \tag{3.16}$$

where N is the current number of electrons. The first Townsend coefficient $\alpha = \alpha\,(E/\rho, \rho)$ describes the multiplication of ionization and depends on the electric field E and the gas density ρ. It is determined by the excitation and ionization cross sections of the electrons. The amplification factor $G = N/N_0$ is defined as the ratio of the final number of electrons N in the avalanche to the initial number of electrons N_0 starting the avalanche and is called *gain*.

For a precise measurement of the ionization, the anode wires need to be operated in proportional mode, i.e. the signal resulting from gas amplification is proportional to the number of electrons in the avalanche. This characteristic is ensured as long as the charge density of the avalanche is negligible compared to the linear charge density of the anode wire.

The electrons and ions created during gas amplification near the anode wires induce currents on the surrounding electrodes by moving towards and away from the anode wires [37]. Electrons move to the wire surface within a time much shorter than a nanosecond whereas the slower ions take much longer to drift to the cathode and gating grid wires or the pad plane. Therefore, the signal induction by the electrons is negligible compared to the one by the ions which leads to a signal with a long tail due to the slow ion movement. In order to perform a coordinate measurement of the avalanche, the signal induced on the segmented pad plane is read out.

4 Simulation of Ion Drift in Ne- and Ar-Based Gas Mixtures

Considering the desired detector performance and the resulting requirements for the detector gas, the two noble gases Neon and Argon qualify as the main detector gas of the ALICE TPC as discussed in Section 3.1.1. Limited amounts of CO_2 and N_2 are added as quenchers to absorb UV photons created in ionization processes. Because of their smaller mass, Ne^+-ions move faster through the gas than Ar^+-ions. Therefore, the gas mixtures Ne-CO_2 (90-10) and Ne-CO_2-N_2 (90-10-5) were used during LHC Run 1, avoiding a potential accumulation of positive ions from primary and secondary ionization inside the TPC drift volume which would distort the uniform drift field. The amount of primary ionization of Ne is relatively small which is further discussed in Section 4.1.2. As a consequence a high gas amplification factor of about 10^4 is necessary to achieve the required signal-to-noise ratio. Ne-CO_2 mixtures are very sensitive to variations of the electric field, temperature, pressure and exact composition with respect to the amplification process. Thus the operation at high gains enhances the risk for a breakdown in the form of self-sustained discharges [31]. In Run 2 the interaction rates are expected to increase up to 10 kHz in Pb-Pb. Under such conditions the stability of the readout chambers can be improved by using Ar instead of Ne as the counting gas. Because of its smaller ion mobility the use of Ar can result in drift field distortions caused by the ions from primary and secondary ionization, which are of the order of the position resolution with Ne. The minimum closing time of the gating grid also increases since it is determined by the time it takes the Ar^+-ions created during gas amplification to reach the surrounding electrodes of the readout chamber. The gating grid closing time puts an intrinsic limitation on the maximum rate at which the TPC can register consecutive events without letting ions from the amplification region drift back into the drift volume. Such an ion backflow implies space-charge distortions inside the drift volume which are significantly larger than the potential distortions due to the ions from the ionization of particle tracks. Considering a change from Ne to Ar, the properties of several Ne- and Ar-based gas mixtures, such as electron transport and characteristic ionization quantities, are studied in Section 4.1. Systematic studies of the drift times of ions from the amplification region of the MWPCs in the gas mixtures considered are presented and discussed in Section 4.3.

The studies are performed with the Garfield software package [40] which is used to simulate the electric field configuration of a TPC readout chamber as well as the movement of electrons and ions in electric and magnetic fields. An interface to the Magboltz program [41] provides the electron transport properties of the gas mixtures. The energy loss and ionization by a fast charged particle traversing the chamber is calculated by an interface to the HEED program [42].

4.1 Gas Properties

The characteristic properties of gas compositions consisting of Ar and CO_2 are calculated and compared to the previously used gas mixtures Ne-CO_2 (90-10) and Ne-CO_2-N_2 (90-10-5). The CO_2 content of the Ar-based mixtures is varied from 10 % to 16 %. In addition to these conventionally used gas mixtures, compositions of Ne and Ar mixed with CF_4 are investigated as well as the mixture Ne-CO_2-N_2 (90-5-10). However, CF_4 reacts with aluminum in the presence of water and elemental fluorine attacks the wire materials [30]. Thus the compatibility of CF_4 to the materials used in the TPC has to be validated before it can be considered as a quencher.

A constant gas temperature and pressure for all gas mixtures ensures the consistent comparison of the gas properties. A temperature of 300 K is assumed and the pressure is set to 1 atm, which comes very close to the real operating conditions in the TPC.

4.1.1 Electron Transport

The electron transport properties of the gas mixture have significant implications for the performance of the TPC. They depend on the electric field strength and the gas density and pressure. As discussed in 3.3.2 and [37], the additional magnetic field of the TPC can have a considerable impact on the drift of the electrons. Therefore, all calculations are done with a magnetic field $B = 0.5\,\mathrm{T}$ parallel to the electric field unless stated otherwise. The uncertainties of the calculations are correlated with the accuracy of the cross sections and Monte Carlo techniques provided by Magboltz.

The electron drift velocity determines the drift time of ionization electrons to the readout chambers. The maximum electron drift time defines the period of time for which the gating grid is opened to collect all of the ionization from a single event. It is one major factor contributing to the dead time of the TPC since the gating grid is closed afterwards to block ionization from further events until the readout is completed.

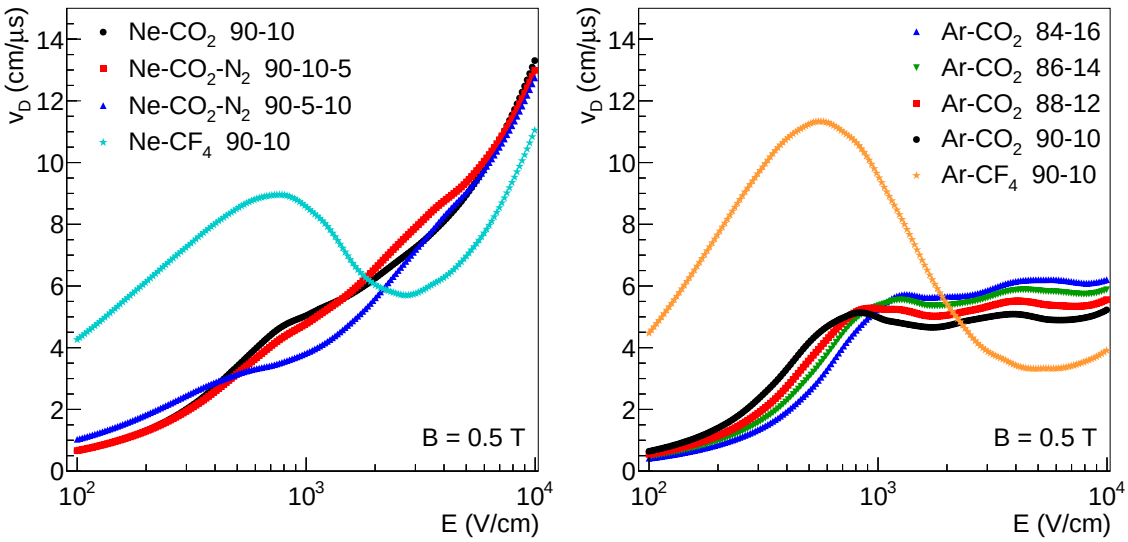

Figure 4.1: Electron drift velocity v_D as a function of the electric field E for Ne-based (left) and Ar-based (right) gas mixtures.

Figure 4.1 shows the electron drift velocity v_D as a function of the electric field E for the various gas mixtures. In Ne-CO_2 and the Ne-CO_2-N_2 mixtures the drift velocity continuously increases with the electric field whereas in the Ar-CO_2 mixtures it reaches a local maximum near 1 kV/cm. This behavior is explained by the electron scattering cross sections of Ne, Ar and CO_2 shown in Figure 4.2 [30]. At the relevant electron energies up to a few eV, the cross section for Ne rises with increasing energy whereas the cross section for CO_2 is dominated by a decrease in most of the energy regions. The cross section for Ar has a characteristic minimum at 0.23 eV called the *Ramsauer minimum* which leads to the maximum in the drift velocity. Adding CF_4 to Ne or Ar, the drift velocity is significantly larger compared to the CO_2 mixtures and has a more pronounced peak compared to the Ar-CO_2 mixtures. The cross section for CF_4 (Figure 4.3) is smaller by one order of magnitude at low electron energies compared to CO_2 and has a Ramsauer minimum leading to the significant increase of the drift velocity and the local maximum. The peak value of the Ar-CO_2 mixtures increases and moves to higher electric fields with larger fractions of CO_2. A general tendency can be observed in both the Ne-CO_2-N_2 and the Ar-CO_2 mixtures varying the CO_2 fraction. At low electric fields the drift velocity decreases with higher CO_2 fractions. The energy distribution of the electrons is shifted to lower energies at a constant electric field when more CO_2 is added and, in addition, the minimum of the cross sections moves to larger electron energies. At large electric fields the drift velocity increases with the CO_2 fraction. The high electric field strengths lead to a higher mean electron energy which dominates the shift of the energy distribution to lower electron energies. On the other hand the addition of N_2 to Ne-CO_2 only slightly effects the drift velocity.

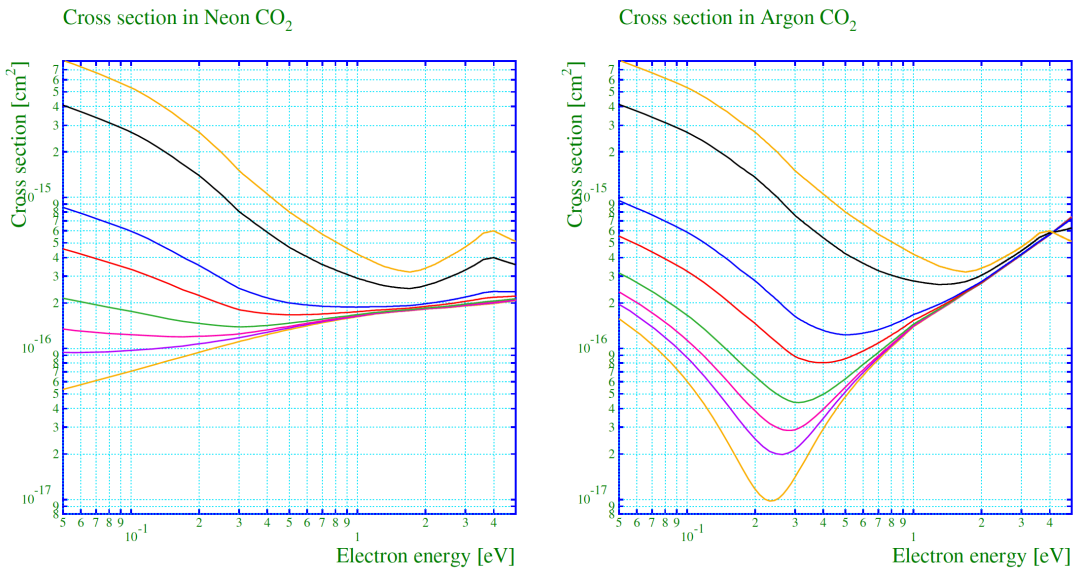

Figure 4.2: Electron cross sections for Ne-CO_2 (left) and Ar-CO_2 (right) as a function of the electron energy. The curves correspond, from bottom to top, to 0 %, 0.5 %, 1 %, 2 %, 5 %, 10 %, 50 % and 100 % CO_2 concentration [30].

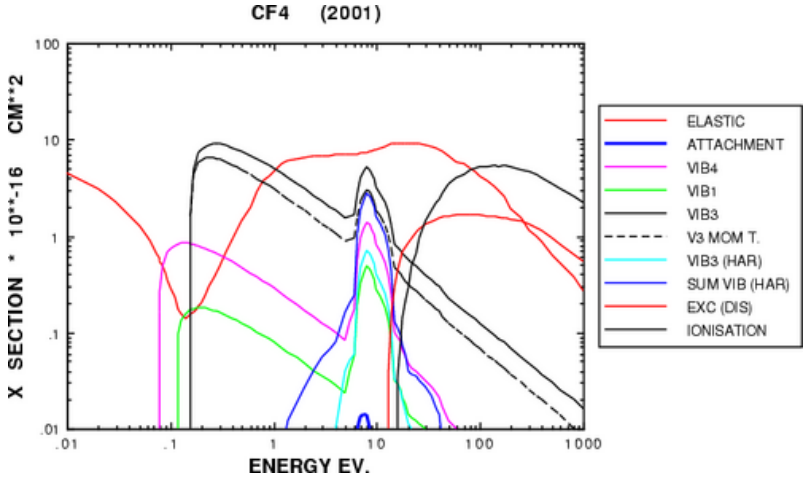

Figure 4.3: Electron scattering, attachment, excitation and ionization cross sections for CF_4 as a function of the electron energy [41].

The diffusion of the ionization electrons is crucial for the space point resolution of the TPC. The transverse diffusion is a factor in the $r\varphi$ resolution which determines the momentum resolution. In order to achieve the desired spatial resolution of $\sigma_{r\varphi} < 200\,\mu$m, its contribution should be small compared to other factors, i.e. the transverse diffusion over the full drift length divided by the mean number of ionization electrons per pad should be considerably smaller than the spatial resolution. The longitudinal diffusion determines the resolution in the drift time direction which is not as critical since the tracks in this direction are straight in a first order approximation.

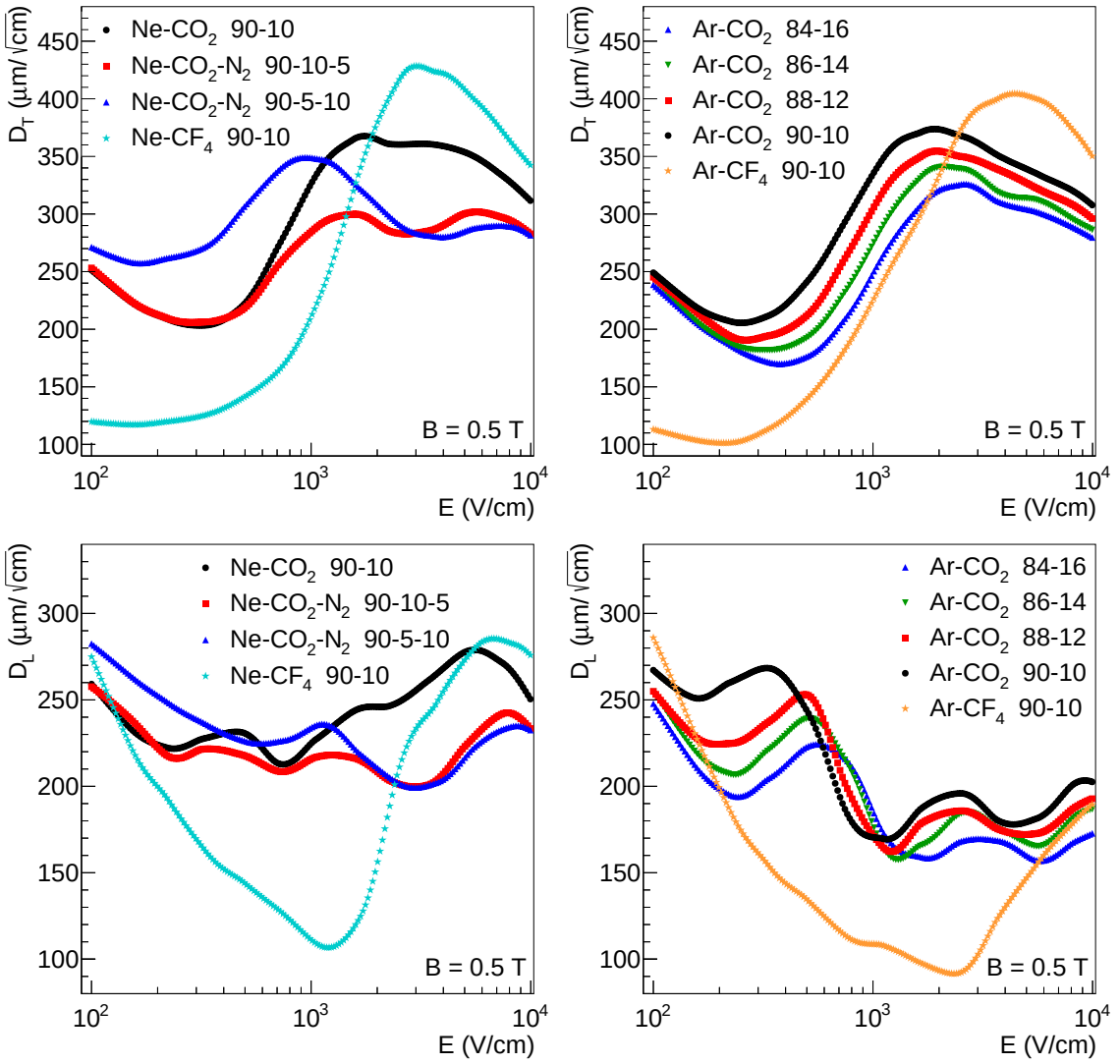

Figure 4.4: Transverse diffusion coefficient D_{T} (top) and longitudinal diffusion coefficient D_{L} (bottom) as a function of the electric field E for Ne-based (left) and Ar-based (right) gas mixtures.

The calculated transverse and longitudinal diffusion coefficients D_{T} and D_{L} as a function of the electric field E are shown in Figure 4.4. Comparing the Ne- and Ar-based gas mixtures, the diffusion is of the same order and behaves in a similar way up to an electric field of 1 kV/cm. The diffusion of the mixtures quenched with CF_4 significantly differs from the CO_2 mixtures and is much smaller in the majority of the electric field range. At the low electric fields most interesting for the TPC operation, the difference between the transverse and longitudinal diffusion is within 10 % for Ne-CO_2 and the Ne-CO_2-N_2 mixtures and within 20 % for the Ar-CO_2 mixtures. At these fields the addition of N_2 to Ne-CO_2 also has a relatively small effect on both the transverse and longitudinal diffusion. An increase of the CO_2 fraction of the Ne-CO_2-N_2 and Ar-CO_2 mixtures leads to a systematic decrease of the diffusion coefficients.

Gas		Drift velocity v_D (cm/μs)	Diffusion coefficients D_T (μm/$\sqrt{\text{cm}}$)	D_L	Lorentz angle $\omega\tau$
Ne-CO_2	90-10	2.73	208	231	0.34
Ne-CO_2-N_2	90-10-5	2.58	209	221	0.32
	90-5-10	2.88	285	231	0.39
Ne-CF_4	90-10	8.02	131	152	1.77
Ar-CO_2	84-16	1.94	170	212	0.25
	86-14	2.28	184	230	0.30
	88-12	2.74	199	246	0.36
	90-10	3.31	221	262	0.43
Ar-CF_4	90-10	10.77	123	144	2.07

Table 4.1: The electron transport properties for Ne- and Ar-based gas mixtures evaluated at an electric field of 400 V/cm and a parallel magnetic field of 0.5 T. The Lorentz angle $\omega\tau$ is calculated for the magnetic field perpendicular to the electric field.

A summary of the electron transport properties evaluated at the nominal TPC drift field of 400 V/cm for all gas mixtures is given in Table 4.1. The Lorentz angle $\omega\tau$ is calculated for the magnetic field perpendicular to the electric field. All quantities for Ne-CO_2 (90-10) and Ne-CO_2-N_2 (90-10-5) are identical for practical purposes as the biggest difference is found in the drift velocities with a deviation of 5 %. Ar-CO_2 (90-10) has a higher drift velocity, larger diffusion coefficients and a larger Lorentz angle than Ne-CO_2 (90-10). Increasing the CO_2 fraction of Ar-CO_2 leads to a decrease of all properties. The electron transport in Ar-CO_2 (88-12) is very similar to that in Ne-CO_2 (90-10) as the drift velocity and $\omega\tau$ are the same, the transverse diffusion is slightly smaller and the longitudinal diffusion is slightly bigger. Therefore, a change from Ne-CO_2 to Ar-CO_2 (88-12) has only minor implications for the electron transport in the TPC. The CF_4 mixtures show significantly different properties. The drift velocity is higher by a factor of three to four and the diffusion is smaller almost by a factor of two, reducing the maximum drift time of ionization electrons. The effect of the large Lorentz angle plays a role when the deviation of the directions of the E- and B-field becomes larger or when there is an $E \times B$ effect in the drift volume because of space-charge.

4.1.2 Ionization

The ionization along the trajectory of a particle provides a direct measurement of the specific energy loss which is used for particle identification in the TPC. The amount of ionization per unit track length is a characteristic property of gas mixtures. It depends on the ionization potentials and cross sections of the gas components as well as on the particle velocity. The primary ionization N_p is defined by the number of ionization electrons per unit track length created directly by collisions of the

Gas	E_i (eV)
CO_2	13.8
N_2	15.6
Ar	15.7
CF_4	15.9
Ne	21.6

Table 4.2: The ionization potential E_i of the different gas components used in the gas mixtures investigated [41].

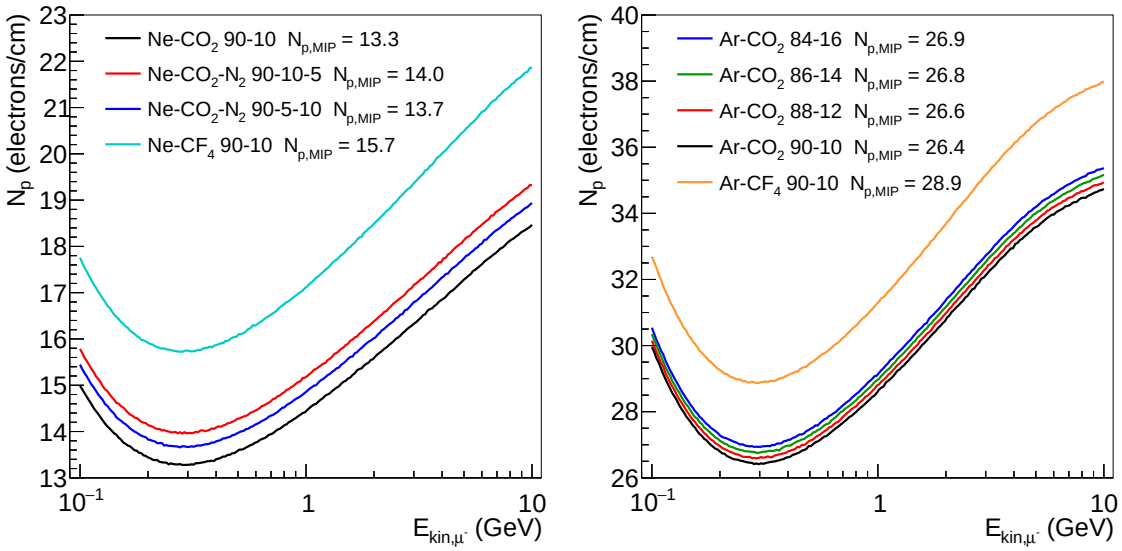

Figure 4.5: The primary ionization N_p as a function of the kinetic energy E_kin of muons for Ne-based (left) and Ar-based (right) gas mixtures. The values at the MIP position are quoted in the legends.

particle with the gas atoms. The total ionization N_t includes the electrons created in secondary ionization processes. Both quantities are usually quoted for MIPs. In general a higher ionization is beneficial since it improves the potential energy resolution of the energy loss measurement and the position resolution. Another advantage of a high ionization is the possibility to operate the TPC readout chambers at lower gains to achieve the desired signal-to-noise ratio, which improves their stability. The effective ionization energy W_i which is spent on average for one ionization process is used to calculate the energy loss when the amount of deposited charge along the track is known.

The ionization potentials of the gas components used in the gas mixtures investigated are listed in Table 4.2. Ne has by far the highest ionization potential of 21.6 eV while the one of Ar, N_2 and CF_4 is very similar around 15.7 eV. The minimum ionization energy of CO_2 is the lowest with 13.8 eV.

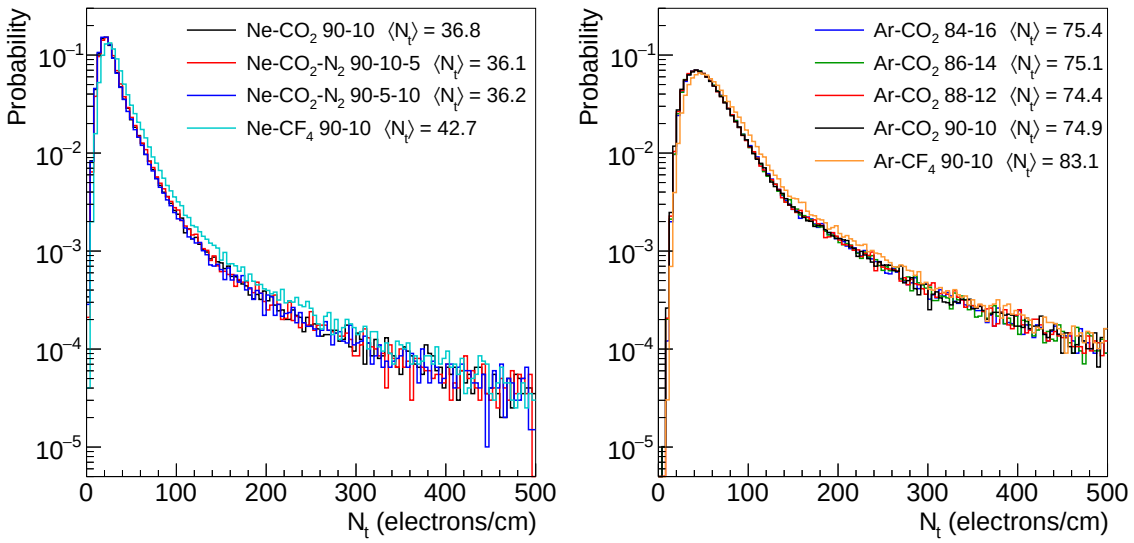

Figure 4.6: The total ionization (N_t) distributions of a MIP for Ne-based (left) and Ar-based (right) gas mixtures. The mean values $\langle N_\mathrm{t} \rangle$ of the distributions are quoted in the legends.

The different ionization potentials are reflected in the primary ionization N_p which is calculated as a function of the muon kinetic energy in Figure 4.5 for the various Ne- and Ar-based gas mixtures. It is averaged over 200 000 tracks of 1 cm length for each energy. The curves have the expected Bethe-Bloch shape discussed in Section 3.3.1. The fluctuations represent the statistical accuracy of the calculations. The primary ionization is evaluated at the MIP position and quoted in the legends of the figures. Due to the large fractions of Ne and Ar, respectively, their ionization potentials dominate the energy loss. The differences in the primary ionization for Ne-CO_2 and the Ne-CO_2-N_2 mixtures is negligible for practical purposes as it amounts around 13.6 electrons per cm. The primary ionization of 15.7 electrons per cm for Ne-CF_4 (90-10) is slightly higher. As for the Ar-CO_2 mixtures, there is a minor increase of the number of primary electrons from 26.4 to 26.9 when the CO_2 fraction is increased and again a small increase to 28.9 when CF_4 is added to Ar. Due to the lower ionization potential of Ar and the smaller radiation length the primary ionization is higher by a factor of two comparing the Ar-based mixtures to the Ne-based mixtures.

The distribution of the total ionization N_t is calculated for 200 000 muon tracks with a kinetic energy of 290 MeV (MIP) and a length of 1 cm. The results for the different gas mixtures are shown in Figure 4.6. The distributions have long tails which lead to large fluctuations and can be approximately described by a Landau distribution. Therefore, one can either quote the mean value of the distribution or the most probable value which is represented by the peak and is significantly different from the mean. The mean values of the distributions $\langle N_\mathrm{t} \rangle$ are quoted in the legends of the figures. They are within 2 % for the different Ne-CO_2(-N_2)

Gas		Primary ionization N_p (electrons/cm)	Total ionization $\langle N_t \rangle$ (electrons/cm)	Effective ionization energy W_i (eV)
Ne-CO_2	90-10	13.3	36.8	38.1
Ne-CO_2-N_2	90-10-5	14.0	36.1	37.3
	90-5-10	13.7	36.2	37.7
Ne-CF_4	90-10	15.7	42.7	37.7
Ar-CO_2	84-16	26.9	75.4	29.3
	86-14	26.8	75.1	28.9
	88-12	26.6	74.4	29.0
	90-10	26.4	74.9	28.8
Ar-CF_4	90-10	28.9	83.1	28.9

Table 4.3: The basic ionization properties of the different Ne- and Ar-based gas mixtures for a minimum ionizing particle (MIP).

and Ar-CO_2 mixtures, respectively, as the distributions are on top of each other. The mean total ionization of Ar-CO_2 is higher by a factor of about two compared to Ne-CO_2(-N_2) as the width of the distributions increases. For Ne-CF_4 and Ar-CF_4 the total ionization increases by 10–15 % compared to the respective mixtures with CO_2. These observations are in agreement with the results obtained for the primary ionization.

The effective ionization energy W_i is also calculated averaging over 200 000 muon tracks of 1 cm length at the MIP position. The mean total energy of an electron cluster is divided by the mean cluster size. The results are shown in Table 4.3 together with the primary and mean total ionization. The effective ionization energy for the Ne-based gas mixtures is higher by 30 % compared to the Ar-based gas mixtures as the ionization potential of Ne is higher by the same factor.

Penning Effect

The penning effect significantly impacts the amount of ionization and has to be taken into consideration for the application of gas mixtures based on Ne or Ar. Especially the ionization during the gas amplification process in the readout chambers is affected as comparisons of measurements and simulations of the gain imply considerable penning transfer rates [30]. The excitation states of Ne are all above 16.6 eV. Regarding the ionization potentials in Table 4.2, the excited Ne atoms can ionize all of the quenchers used. The excited state of Ar with an energy of 14.0 eV can still lead to the ionization of the CO_2 molecules. These effects are included for the calculations of the ionization properties and of the gain of the readout chambers (Section 4.2) by applying the penning transfer rates listed in Table 4.4. Their precision is of the order of 20 % since they were obtained by tuning results of simulations

Gas	Penning transfer rate (%)
Ne-CO_2	49.0
Ne-CO_2-N_2	32.6
Ne-CF_4	30.0
Ar-CO_2	37.0

Table 4.4: The penning transfer rates applied for the ionization and gain calculations for the different gas mixtures [43].

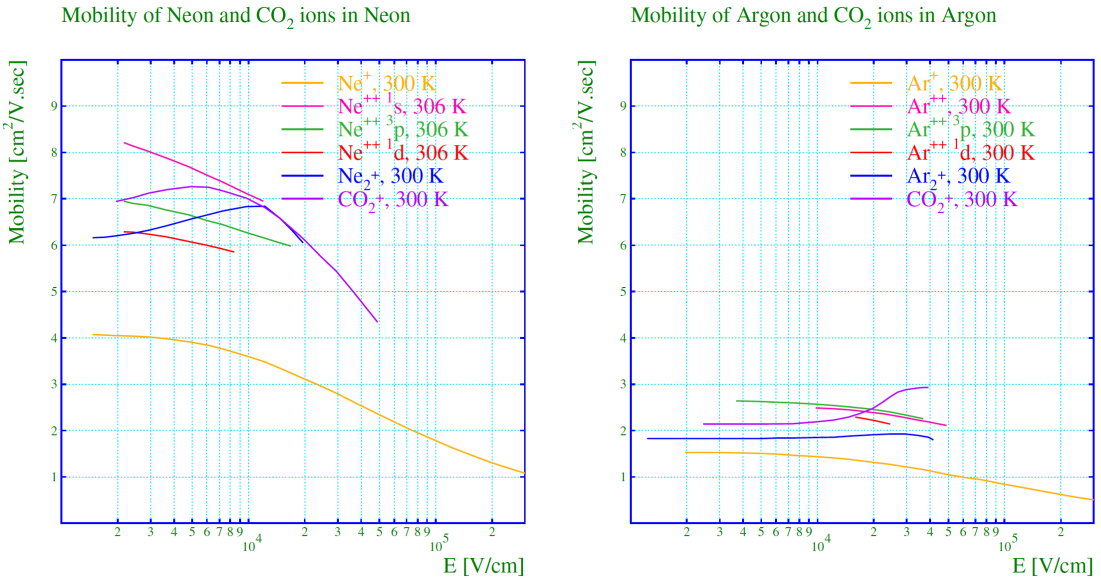

Figure 4.7: The mobility of Ne-ions and $CO_2{}^+$ in pure Ne (left) and the mobility of Ar-ions and $CO_2{}^+$ in pure Ar (right) as a function of the electric field [30].

to data. The same rates are used for all the different compositions of the respective gas mixtures.

4.1.3 Ion Mobility

Contrary to the electron transport properties, the mobility of ions in the gas is not provided by Magboltz and has to be entered manually. An extensive series of measurements of the mobility of numerous ions in several gases has been performed by different groups since the 1950's and is summarized in [30]. The precision of the detectors used for these measurements is of the order of 1–5 %. The mobility of Ne-ions in pure Ne, Ar-ions in pure Ar and CO_2 ions in both pure Ne and pure Ar as a function of the electric field is shown in Figure 4.7. Ne^+ is faster by a factor of about 2.5 than the Ar^+-ions. The $CO_2{}^+$-ions are faster by a factor of 1.5–2 compared to the Ne^+- and Ar^+-ions. For the calculation of the ion drift in Section 4.3 the mobility of Ne^+ in Ne is used for all Ne-based gas mixtures as well as the mobility of Ar^+ in Ar for all Ar-based gas mixtures. The effect of CO_2-, N_2- and CF_4-ions is neglected.

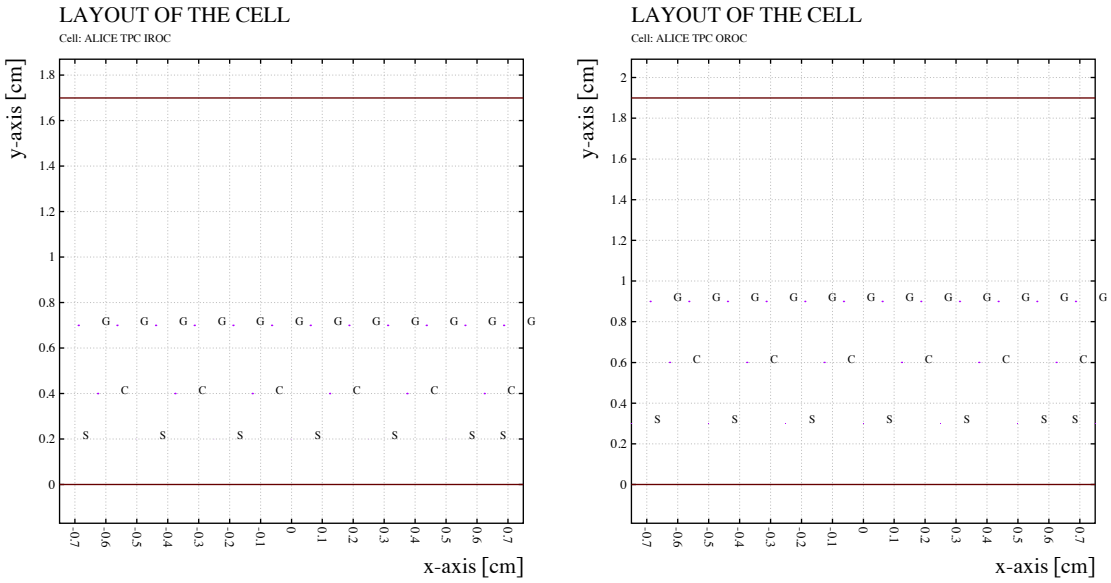

Figure 4.8: The layout of the simulated IROC (left) and OROC (right). The lines at $y = 0$ represent the pad plane, the lines at $y = 1.7$ (IROC) and $y = 1.9$ (OROC) the central electrode. The big purple dots are the gating grid wires (G) and the cathode wires (C) whereas the dots representing the anode wires (S) are barely visible since their diameter is much smaller.

The relevance of the different ion species in the gas for the amplification process, the clustering of ions and the implications for the effective mobility of the drifting ions is discussed in [44]. In Ne-CO_2 (90-10) the ionization rate of CO_2 dominates the one of Ne until the very late stages of the avalanche. Therefore, a large fraction of the drifting ions consists of ${CO_2}^+$. In Ar-CO_2 (90-10) the Ar^+-ions are dominant during the gas amplification. However, the Ne^+- and Ar^+-ions transfer their charge to CO_2 within a few ns which is a much shorter time scale than the drift time of the ions until they are collected by the electrodes. As a result the ${CO_2}^+$-ions remain as the relevant ion species for the ion drift. Within about 100 μs they start to build clusters with predominantly one or more CO_2 molecules. The measurements of the mobility of such ${CO_2}^+ \cdot (CO_2)_n$ clusters are summarized in [44]. By coincidence, the mobility of ${CO_2}^+ \cdot (CO_2)_n$ in Ne-CO_2 (90-10) and Ar-CO_2 (90-10) differs by only 10–15 % compared to the mobility of Ne^+ in pure Ne and Ar^+ in pure Ar, respectively.

4.2 Chamber Layout and Settings

The geometry of the TPC readout chambers described in Section 3.1.3 is implemented for the calculation of the drift of ions created during gas amplification. Sketches of the simulated IROC and OROC are shown in Figure 4.8. The anode wire plane, the cathode wire plane and the gating grid each have an infinite lateral extent (x-direction) to avoid edge effects. The drift direction of the ionization elec-

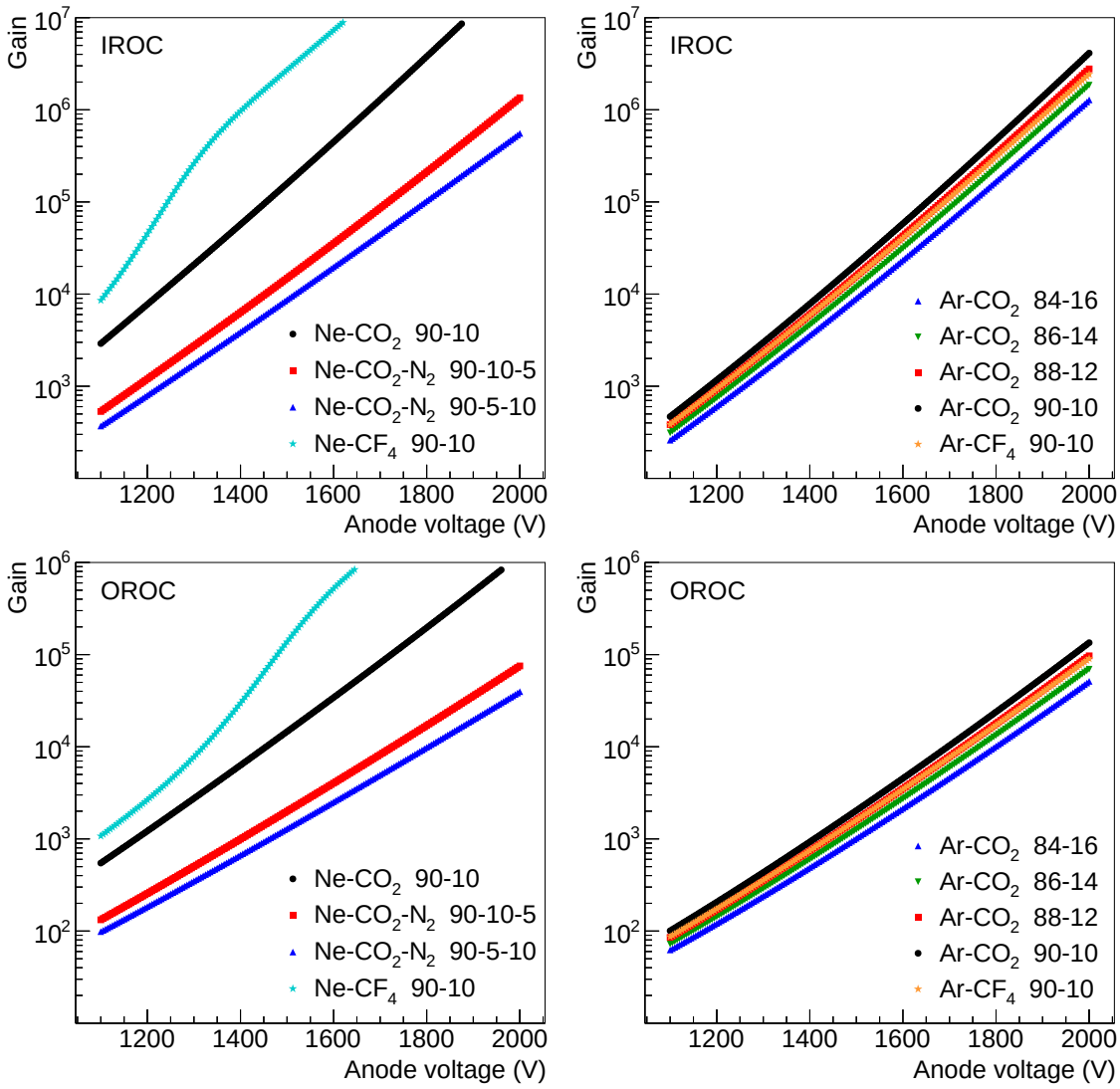

Figure 4.9: The gain in the IROC (top) and OROC (bottom) as a function of the anode voltage for Ne-based (left) and Ar-based (right) gas mixtures.

trons runs along the y-axis, the x-axis corresponds to the radial direction. The wire parameters, such as material and thickness, and the distances between the electrodes match the ones of the real TPC readout chambers. The pad plane is approximated as an infinite equipotential plane. Another equipotential plane represents the central electrode and determines the length of the drift volume which is chosen to be 1.3 cm in the simulated chamber.

In order to emulate the real operating conditions the voltages of the pad plane and the cathode wires are set to 0 V. The CE potential is adjusted to generate a drift field of 400 V/cm and a magnetic field of 0.5 T in the drift direction is applied. The offset and gating voltage of the gating grid wires are set to $V_{\mathrm{G}} = -70\,\mathrm{V}$ and $\pm\Delta V = 90\,\mathrm{V}$ for the IROC and $V_{\mathrm{G}} = -155\,\mathrm{V}$ and $\pm\Delta V = 90\,\mathrm{V}$ for the OROC as these settings were used in the real TPC [43]. Since the ionization properties of the Ar-based gas mixtures yield roughly twice as many ionization electrons per unit track length as for

Gas		IROC		OROC	
		Anode voltage (V)	Gain	Anode voltage (V)	Gain
Ne-CO_2	90-10	1230	10 397	1460	10 418
Ne-CO_2-N_2	90-10-5	1460	10 539	1730	10 221
	90-5-10	1520	10 273	1805	10 221
Ne-CF_4	90-10	1115	10 710	1325	10 542
Ar-CO_2	84-16	1440	5189	1715	5202
	86-14	1415	5268	1685	5273
	88-12	1385	5204	1650	5241
	90-10	1360	5307	1615	5125
Ar-CF_4	90-10	1385	5076	1650	5107

Table 4.5: The anode voltage settings and the resulting gains for the simulated chambers for Ne- and Ar-based gas mixtures.

the Ne-based mixtures (Section 4.1.2), the gain for the Ar mixtures can be a factor two lower than for the Ne mixtures to achieve the same signal-to-noise ratio. Using Ne-CO_2 (90-10) and Ne-CO_2-N_2 (90-10-5) the TPC readout chambers are operated at a gain of about 10 000 which implies a gain of 5000 for the Ar-based gas mixtures. To adjust the potential of the anode wires accordingly, the mean gain is calculated as a function of the anode voltage for both IROC and OROC as shown in Figure 4.9. The accuracy of these calculations is assumed to be of the order of 10 % due to the uncertainty of the penning rates. In the simulation very high amplification factors are possible which is not the case in reality because of discharge effects. The voltages chosen for the anode wires are summarized in Table 4.5 together with the resulting gains.

4.3 Calculation of Ion Drift Times

During the gas amplification process an equal number of electrons and gas ions is created in the readout chambers. The electrons quickly drift towards the anode wires where they are absorbed. Most of the ions drift in the opposite direction towards the drift volume of the TPC. A good fraction of ions escapes the amplification region defined by the cathode wires. The offset voltage of the GG wires is adjusted by the gating voltage $\pm\Delta V$ to collect these ions. This configuration attracts the ions at one GG wire and repels them from the next one, thus preventing them from entering the drift volume. Even a fraction of these ions escaping into the drift volume would lead to significant space-charge distortions since the amount of ions in the amplification region is larger by the gain factor compared to the number of ions from primary and secondary ionization processes. Therefore, the gating grid has to stay closed until all ions are collected at the cathode and GG wires implying an intrinsic rate limitation to the TPC. The resulting ion-collection time varies with

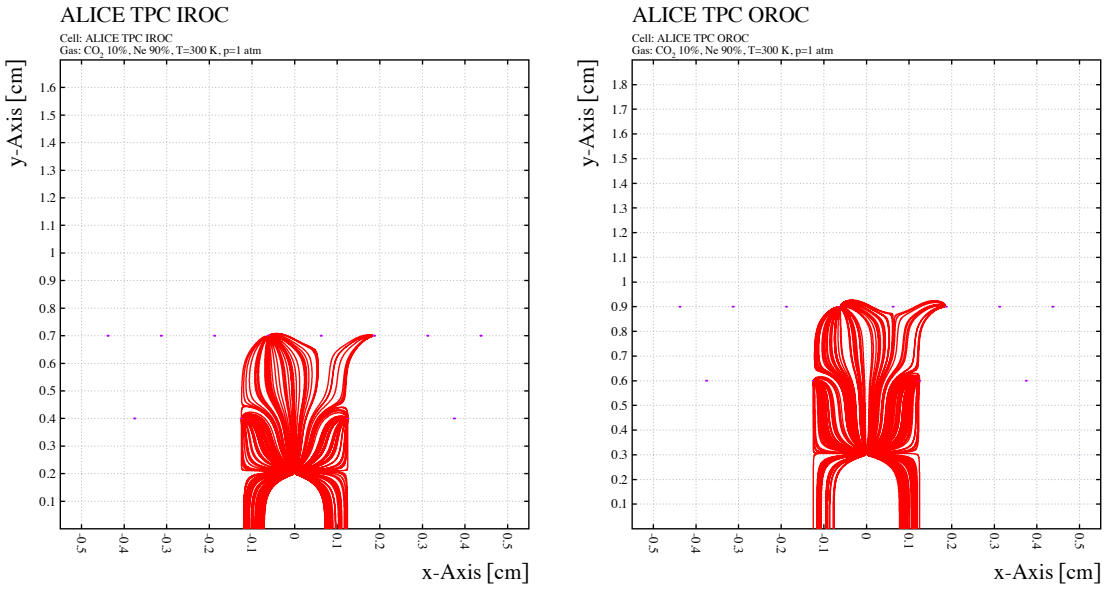

Figure 4.10: The drift lines of ions distributed randomly around the anode wire in the IROC (left) and OROC (right). The ions initially have a distance of 10 μm from the wire surface and an angular distribution of $\pm 0.675\pi$ with respect to the drift direction of the ionization electrons. They end up on the pad plane, cathode wires and GG wires.

the ion mobility and the electric field in the amplification region. Because of their bigger mass Ar^+-ions are slower by a factor of about 2.5 compared to Ne^+-ions as discussed in Section 4.1.3. The $CO_2{}^+$-ions in Ne are also faster by about the same factor than in Ar. Thus a change of the main gas component from Ne to Ar leads to an increase of the ion-collection time. The time the gating grid is kept in the closed state has to be adjusted accordingly.

The ion-collection time is calculated for different Ne- and Ar-based gas mixtures. The results for Ne-CO_2 (90-10) and Ne-CO_2-N_2 (90-10-5) are compared to Ar-CO_2 with CO_2 fractions of 10 % and 12 % since it provides the required electron transport properties (Section 4.1.1). Ne-CF_4 (90-10) and Ar-CF_4 (90-10) are also used in the simulations. The offset and gating voltage of the gating grid are varied to study the effect on the ion-collection time. For comparison the ion-collection time and the fraction of ions escaping into the drift volume are calculated for the case of an open gating grid. The accuracy of the calculated ion drift times is correlated with the precision of the ion mobility data.

4.3.1 Ion-Collection time

Although the avalanches in the amplification region have some lateral extent, the ion-collection time is determined by the ions with the longest drift time which are created in the vicinity of the anode wires. A total number of 200 000 ions are dis-

tributed randomly around one anode wire at a distance of 10 μm from the wire surface. Since the ionization electrons starting the avalanches all come from the same direction, the angular extent of the avalanche around the wire is limited and depends on the total charge of the avalanche. An angular distribution of the ions around the anode wire of $\pm 0.675\pi$ with respect to the drift direction of the ionization electrons is assumed.

The drift lines of the ions in the IROC and OROC are shown in Figure 4.10. The ions end up at the pad plane, cathode wires and GG wires. Because of the asymmetric configuration of the GG wire potentials the length of the drift lines to the GG wires varies considerably depending on the point of origin of the ion and the GG wire on which the ion ends up.

The corresponding drift times of the ions to the pad plane, cathode wires and GG wires are calculated. They mostly depend on the main gas, the anode wire potentials and the resulting electric field inside the chamber since the drift of the quencher-ions is neglected. The normalized drift time distributions in the IROC and OROC can be seen in Figure 4.11 for the different gas mixtures. Several peaks represent the various electrodes which collect the ions and are similarly distributed for the IROC and OROC. On average, the ions first reach the pad plane and shortly afterwards the cathode wires which are hit by the majority of the ions. The smallest fraction actually passes the cathode wires and ends up at the gating grid. The drift times to the pad plane and the cathode wires in the OROC are larger by about a factor of 1.5 due to the larger distance between the anode wires and the pad plane leading to longer drift lines and different field configurations compared to the IROC. On the other hand the time the ions need to reach the GG wires is about 10 % shorter in the OROC than in the IROC which can be attributed to the higher offset voltage. Two peaks are observed for the gating grid corresponding to two different GG wires and the various length of the drift lines (Figure 4.10). They are about 30 μs apart for the Ne-based mixtures and about 60–80 μs for the Ar-based mixtures. Considering the different peak heights for IROC and OROC, more ions end up at the gating grid in the OROC.

Comparing the drift times for the Ne-based gas mixtures, Ne-CO_2-N_2 (90-10-5) is the fastest mixture followed by Ne-CO_2 (90-10) while the largest drift times are obtained with Ne-CF_4 (90-10) according to the anode wire voltages (Table 4.5). The drift times in the Ar-based mixtures are significantly higher as the width of the peaks also increases. On average the ions take twice as long to hit the pad plane and it takes about 2.5 times as long until the first ions reach the gating grid. Between the Ar mixtures, Ar-CO_2 (90-10) is the slowest, the drift times in Ar-CO_2 (88-12) and

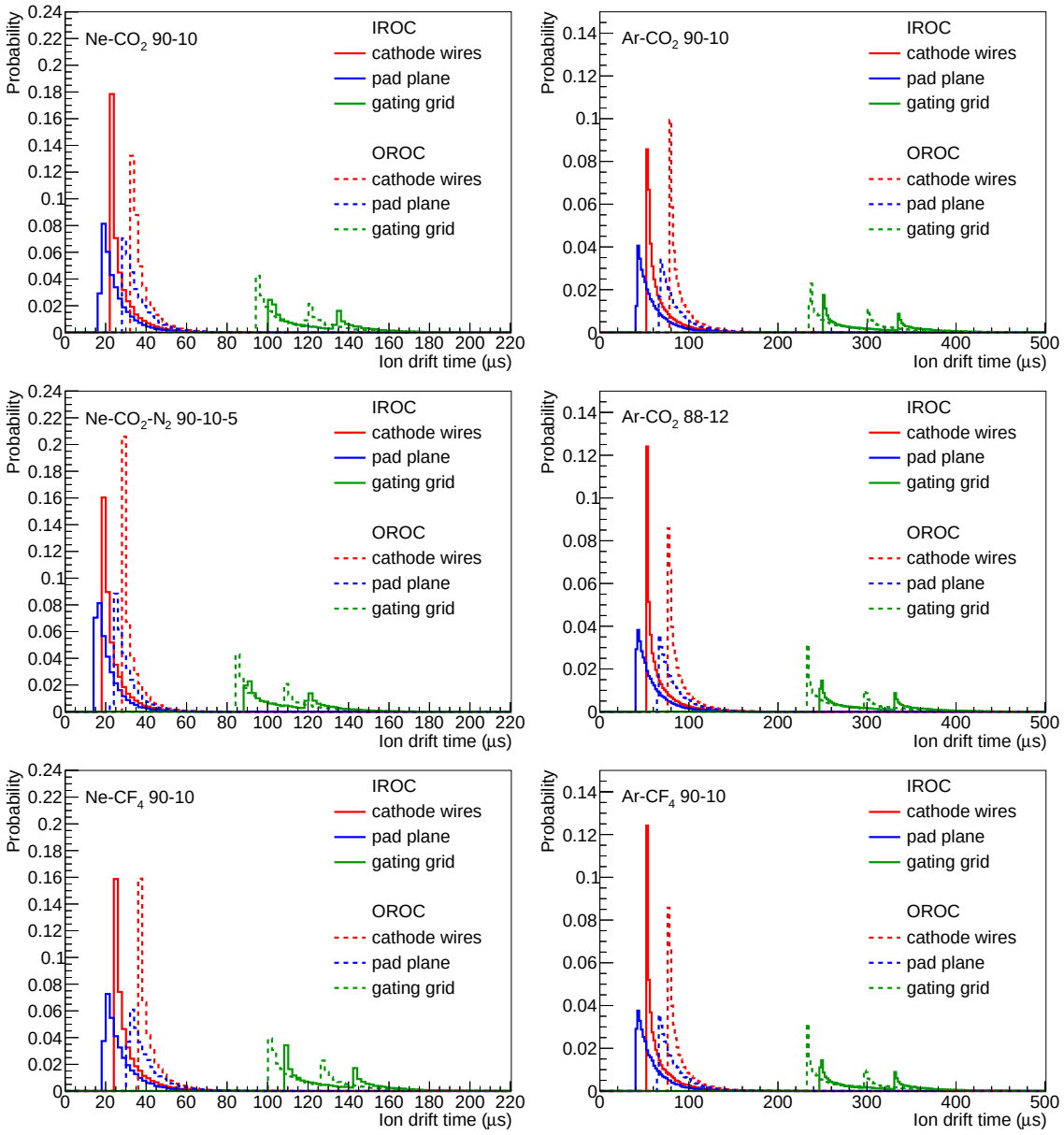

Figure 4.11: The normalized drift time distributions to the cathode wires, pad plane and GG wires in the IROC and OROC for the different Ne-based (left) and Ar-based (right) gas mixtures.

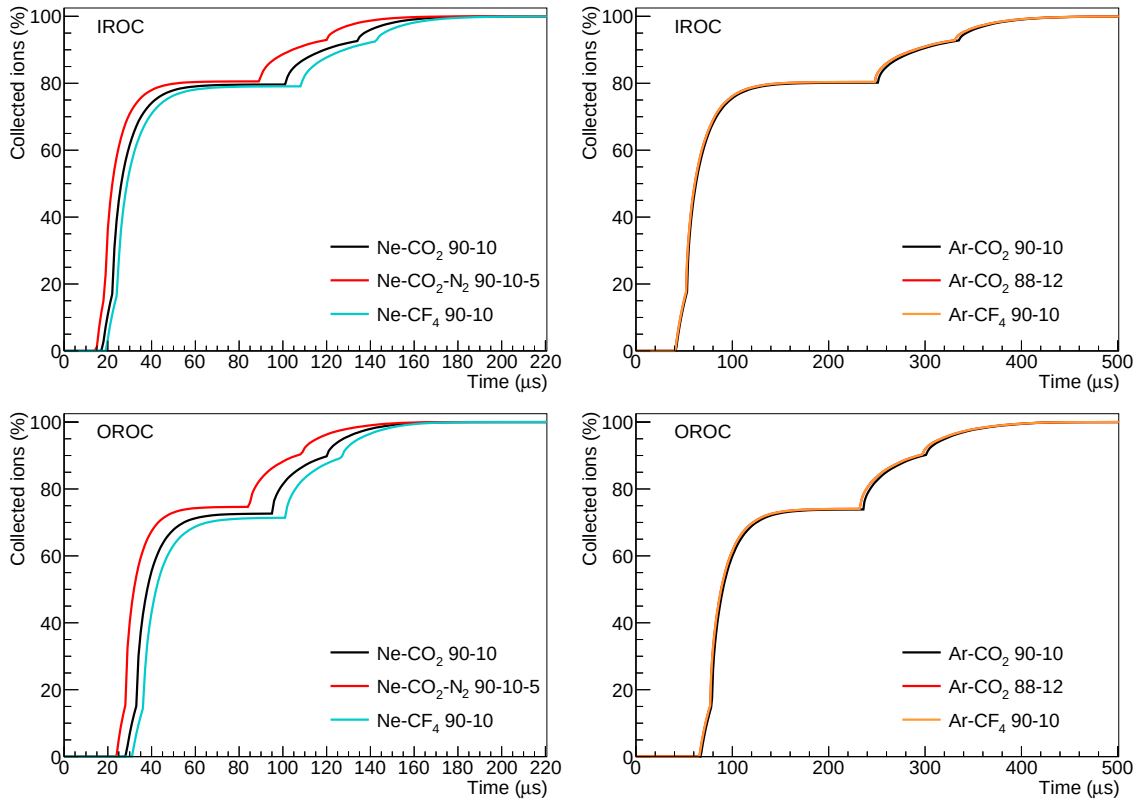

Figure 4.12: The fraction of collected ions as a function of time in IROC (top) and OROC (bottom) for the different Ne-based (left) and Ar-based (right) gas mixtures. Several shoulders represent ions arriving at the various electrodes (pad plane, cathode wires, gating grid) of the readout chamber.

Ar-CF_4 (90-10) are about equal and slightly faster than in the mixture with 10 % CO_2. These differences are also reduced to the different anode wire potentials.

In order to obtain the ion-collection time, the fraction of collected ions as a function of the time is calculated by integrating the total drift time distribution which is the sum of the distributions for cathode wires, pad plane and gating grid. The resulting graphs for the Ne- and Ar-based gas mixtures are shown in Figure 4.12. The curves are characterized by several shoulders representing ions arriving at the various electrodes similar to the different peaks in the drift time distribution. After about 15–30 μs in the Ne mixtures and 40–65 μs in the Ar mixtures the ions start to arrive at the pad plane. The cathode wires are hit by the ions about 5 μs later in Ne and about 10 μs later in Ar. The fraction of ions collected at the pad plane and cathode wires amounts to about 80 % in the IROC whereas this fraction is reduced to 72–75 % in the OROC. The gating grid is reached by the remaining ions after 85–105 μs in the Ne-based mixtures and after 235–250 μs in the Ar-based mixtures. The differences in the drift times and number of collected ions with respect to the various electrodes in the IROC and OROC observed in Figure 4.11 are also seen in Figure 4.12. Corresponding to the drift time distributions, the collection of ions happens faster in

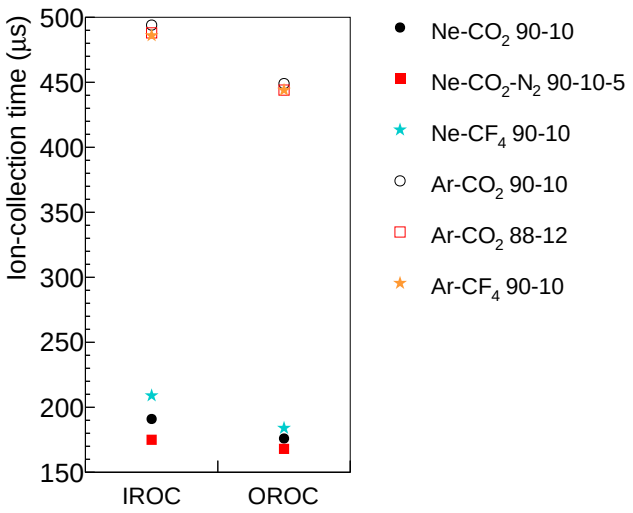

Figure 4.13: The ion-collection time in the IROC and OROC for the different Ne- and Ar-based gas mixtures.

Ne-CO_2-N_2 (90-10-5) than in Ne-CO_2 (90-10) and Ne-CF_4 (90-10) comparing the Ne-based mixtures. The curves for Ar-CO_2 (88-12) and Ar-CF_4 (90-10) are on top of each other and very close to the one of Ar-CO_2 (90-10).

The ion-collection time is deduced by evaluating the graphs in Figure 4.12 at the time when all ions are collected. The results are plotted in Figure 4.13 and quoted in Table 4.6. On average the ion-collection time is about 9 % higher in the IROC than in the OROC. Comparing the Ne-based gas mixtures, the ion-collection times in the IROC for Ne-CO_2 (90-10) and Ne-CF_4 (90-10) are 9 % and 20 % higher, respectively, than for Ne-CO_2-N_2 (90-10-5). In the OROC the relative differences are smaller with 5 % and 10 %, respectively. Taking into account the ion-collection time in the IROC and the maximum drift times of ionization electrons calculated with the electron drift velocities in Table 4.1, the rate at which the TPC can register consecutive events is limited to about 3.6–4.2 kHz with Ne-based gas mixtures (Table 4.6). In the Ar-based gas mixtures, the total ion collection is significantly slower as the ion-collection time increases on average by a factor of 2.6 in the IROC and 2.5 in the OROC compared to the Ne mixtures. The relative differences between the Ar-based mixtures are within 2 % for both IROC and OROC. The major increase of the ion-collection time leads to a decrease of the maximum rate at which the TPC can be operated to 1.7–2.0 kHz depending mostly on the electron drift velocity.

4.3.2 Optimization of the Ion-Collection time with Ar-CO_2

The undesired increase of the ion-collection time by exchanging Ne with Ar is unavoidable simply due to the smaller ion mobilities in Ar. However, there are several ways to improve the ion-collection time to some extent, thus enabling higher event rates in the TPC.

Gas		Ion-collection time IROC (μs)	Ion-collection time OROC (μs)	Max. event rate (kHz)
Ne-CO_2	90-10	191	176	3.6
Ne-CO_2-N_2	90-10-5	175	168	3.7
Ne-CF_4	90-10	209	184	4.2
Ar-CO_2	90-10	494	449	1.8
	88-12	488	444	1.7
Ar-CF_4	90-10	488	444	2.0

Table 4.6: The ion-collection time for the different Ne- and Ar-based gas mixtures. For the maximum event rate of the TPC, the maximum drift time of ionization electrons in the respective gas mixture is taken into account.

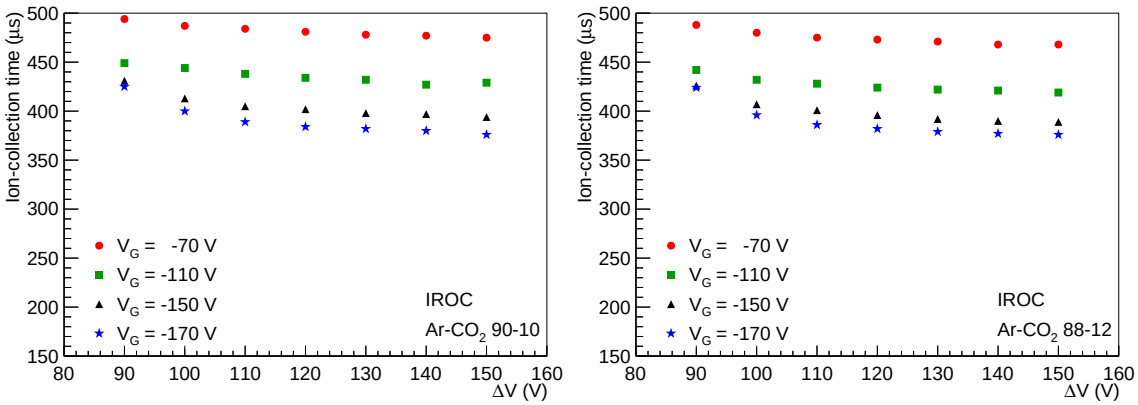

Figure 4.14: The ion-collection time in the IROC for Ar-CO_2 (90-10) (left) and Ar-CO_2 (88-12) (right). The offset voltage V_G and gating voltage ΔV of the GG wires are varied to optimize the ion-collection time.

The ion drift time depends strongly on the electric field inside the readout chamber which can be modified by adjusting the voltages of the electrodes. The anode wire voltage is fixed because it determines the gain which is kept as low as possible to ensure the most stable operation of the readout chamber. Since the ion-collection time is defined by the last ions arriving at the gating grid, a more preferable and promising approach is to increase the offset voltage V_G of the GG wires. The effects on the drift field of the TPC are negligible and can be compensated by adjusting the CE or cathode wire voltages. Since the electron transparency in the open state depends on V_G, it is verified that the gating grid stays fully transparent at higher offset voltages. The gating voltage ΔV is another free parameter which influences the electric field in the readout chamber while the gating grid is closed.

The ion-collection time in the IROC is calculated for Ar-CO_2 (90-10) and Ar-CO_2 (88-12), varying the negative offset voltage between the nominal value of $V_G = -70\,\mathrm{V}$ and $V_G = -170\,\mathrm{V}$ while the alternating gating voltage is increased from the nominal value of $\Delta V = 90\,\mathrm{V}$ to $\Delta V = 150\,\mathrm{V}$. The real application of such high voltages at the GG wires has to be validated since it increases the demands on the

Ar-CO_2 (90-10)	Ion-collection time (μs)						
V_G \ ΔV	90 V	100 V	110 V	120 V	130 V	140 V	150 V
70 V	494	487	484	481	478	477	475
110 V	449	444	438	434	432	427	429
150 V	431	413	405	402	398	397	394
170 V	425	400	389	384	382	380	376

Ar-CO_2 (88-12)	Ion-collection time (μs)						
V_G \ ΔV	90 V	100 V	110 V	120 V	130 V	140 V	150 V
70 V	488	480	475	473	471	468	468
110 V	442	432	428	424	422	421	419
150 V	426	407	401	396	392	390	389
170 V	424	396	386	382	379	377	376

Table 4.7: The ion-collection times in the IROC for a number of different configurations of the offset voltage V_G and gating voltage ΔV of the GG wires. The values are calculated for Ar-CO_2 with 10 % and 12 % CO_2.

gating grid pulser. The results of the parameter scan are shown in Figure 4.14. The ion-collection times obtained are quoted in Table 4.7 for both Ar-CO_2 mixtures. The differences between them are all within 2.5 % for the different voltage configurations. The biggest improvement of the ion-collection time can be achieved by increasing the offset voltage. At V_G = -170 V and the nominal gating voltage, the ion-collection time decreases by 13 % compared to the nominal settings. For higher gating voltages the relative differences between the different offset voltages even reach 20 %. The increase of the gating voltage yields a small improvement of the ion-collection time of 4 % for the highest gating voltage at the nominal offset voltage and 11 % at $V_G = -170$ V. Combining both effects, the lowest ion-collection time is achieved at the highest offset and gating voltage and is 23 % shorter than for the nominal settings. Assuming an improvement of the ion-collection time down to about 450 μs, the limit of the TPC event rate slightly relaxes to 1.8–1.9 kHz. An ion-collection time of 400 μs results in the highest possible event rate of 2.0–2.1 kHz increasing by about 15 % compared to the nominal settings.

A further increase of the maximum event rate of the TPC can be achieved by opening the gating grid before all ions are collected. As a consequence a fraction of ions enters the TPC drift volume where they cause significant field distortions. This effect is even more critical using an Ar-based gas mixture because the much slower ions have to travel the whole drift length of 250 cm which is huge compared to the distance between anode wires and GG wires.

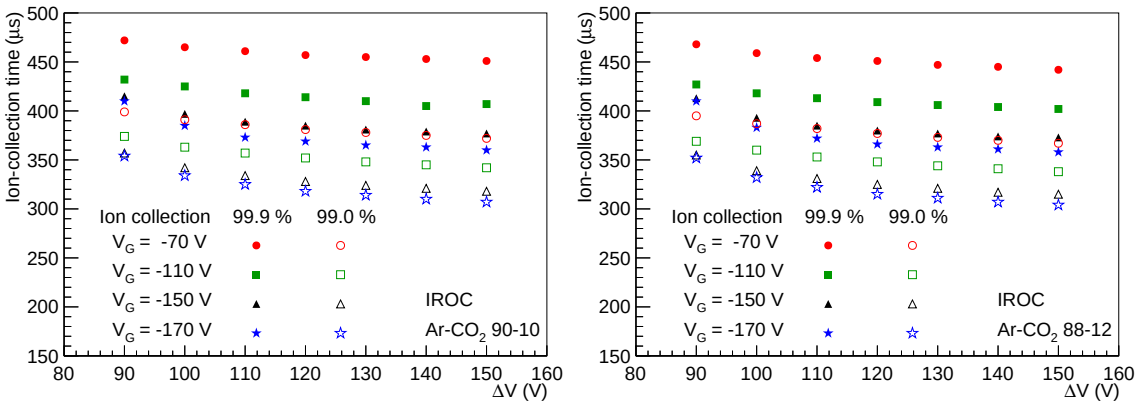

Figure 4.15: The ion-collection time in the IROC for 99.9 % and 99 % of the ions with Ar-CO_2 (90-10) (left) and Ar-CO_2 (88-12) (right). The offset voltage V_G and gating voltage ΔV of the GG wires are varied.

Considering a realistic scenario to keep the space-charge distortions within acceptable limits, the ion-collection time in the IROC for fractions of 99.9 % and 99 % of the total number of ions is calculated by integrating the total drift time distribution until the respective fractions of ions are reached. The offset and gating voltages of the GG wires are varied the same way as before. The results are plotted in Figure 4.15. The variations with respect to the different voltage configurations are comparable to the ones observed in Figure 4.14. Using the nominal voltage settings, the ion-collection time decreases by 4 % for 99.9 % of the ions and by 19 % for 99 % of the ions compared to the previously obtained values. The ion-collection times for 99.9 % of the ions are between 400 μs and 450 μs and can also be achieved, collecting all ions, by simply adjusting the gating grid voltages. If the fraction of collected ions is reduced to 99 %, the gating grid can be opened after about 350 μs by slightly adjusting of the potentials at the GG wires. This yields a possible event rate of 2.3–2.4 kHz for the TPC.

4.3.3 Ion Collection and Backflow with an Open Gating Grid

In addition to the standard case in which the gating grid is kept closed until all ions created during gas amplification are collected, the scenario with a permanently open gating grid is studied. In the open state the gating grid is fully transparent for ionization electrons by setting all the GG wires to the same negative potential V_G. Regarding the drift of ions, the GG wires still attract the ions but the attractive potential is smaller compared to the closed state and the repulsive effect of the electric field between two GG wires with the additional alternating gating voltage $\pm\Delta V$ is missing. Therefore, all field lines either end up at the GG wires or reach the drift volume and end up at the central electrode. As a consequence some ions are not collected at the wires and accumulate as space-charge in the 250 cm long drift volume where they distort the drift path of the ionization electrons. The space-charge

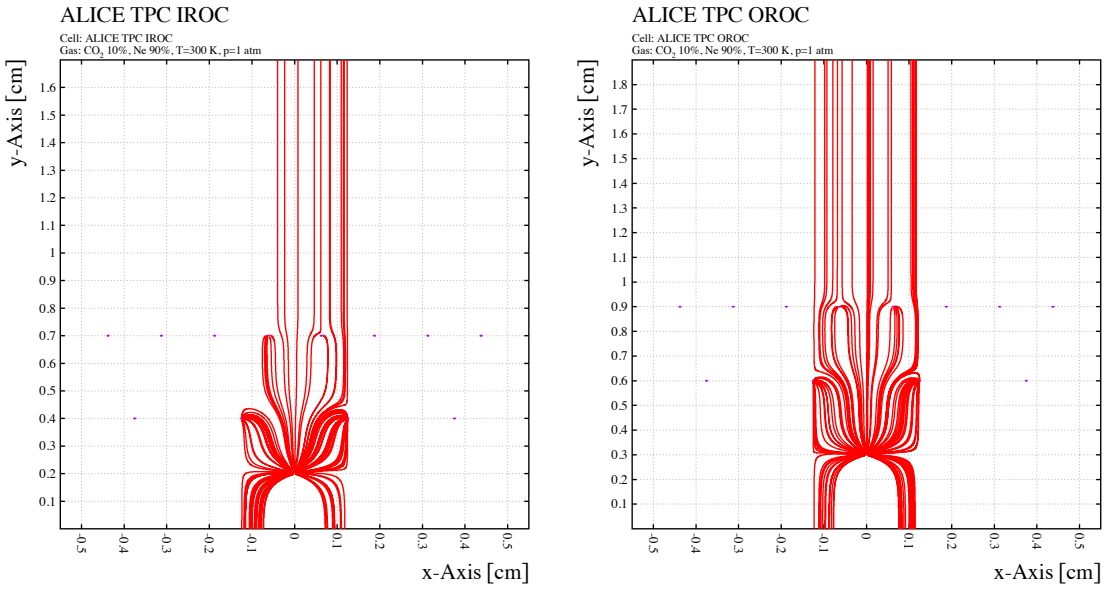

Figure 4.16: The drift lines of ions distributed randomly around the anode wire in the IROC (left) and OROC (right) with an open gating grid. The ions initially have a distance of 10 μm from the wire surface and an angular distribution of $\pm 0.675\pi$ with respect to the drift direction of the ionization electrons. They end up on the pad plane, cathode wires and GG wires or escape into the drift volume and are collected by the central electrode.

distortions in the TPC drift volume caused by back-drifting ions due to an open gating grid are studied in Section 5.3.

The simulation of the ion drift is performed exactly the same way as in Section 4.3.1 except the nominal voltage settings for the open state of the gating grid are used. The GG offset voltage is set to $V_{\mathrm{G}} = -70\,\mathrm{V}$ for the IROC and $V_{\mathrm{G}} = -155\,\mathrm{V}$ for the OROC and the gating voltage is set to $\pm\Delta V = 0\,\mathrm{V}$ for both types of readout chambers. The calculated ion drift lines in the IROC and OROC are shown in Figure 4.16. They are symmetric on both sides of the anode wire which is not the case for a closed gating grid because of the different potentials at neighboring GG wires. Most of the ions end up at the pad plane, cathode wires and GG wires but a considerable fraction of the ions moves into the drift volume.

The ion drift time of the collected and escaped ions is calculated. The drift time of the escaped ions is defined by the time it takes them to reach a virtual plane which is 200 μm above the gating grid. It is assumed that the attractive potential of the GG wires is too weak to collect the ion once it reaches this plane. The total distribution of the collected and escaped ions in the IROC and OROC as a function of the ion drift time is shown in Figure 4.17 for the Ne- and Ar-based gas mixtures. Similar as in Figure 4.11, three peaks are observed for the distribution of the col-

lected ions. The first peak corresponds to the ions ending up at the pad plane, the largest peak to the ions hitting the cathode wires and the third peak at high drift times to the ions collected by the gating grid. The distribution of ions collected at the pad plane and cathode wires is comparable to the results obtained for a closed gating grid. The ions at the gating grid merge in one peak compared to two peaks in the previous results because of the equal potentials at the GG wires. The time it takes the first ions to reach the gating grid is about 10–15 % longer than in the closed state which is also reduced to the different GG wire voltages. The differences between the IROC and the OROC are the same as observed before. Because of the different distances between the anode wires and the pad plane, the ions in the OROC need more time to reach the cathode wires and the pad plane and less time to reach the gating grid. Amongst the Ne-based gas mixtures, the drift times are generally lower in Ne-CO_2-N_2 (90-10-5) than in Ne-CO_2 due to the higher anode voltage which also affects the electric field in the region between cathode wires and GG wires. In Ne-CF_4 the highest ion drift times are observed. The ions in the Ar-based mixtures are about a factor 2.5 slower than in the Ne-based mixtures. Comparing the two Ar-CO_2 mixtures and Ar-CF_4, the ion drift times in Ar-CO_2 (90-10) are about 2 % lower than in the other two mixtures because of the slightly different anode voltages.

The drift time until the first ions finally escape into the drift volume is about 10 % shorter in the OROC compared to the IROC due to the respective GG wire voltages. Two peaks are observed in the distributions of the escaped ions. The peak at shorter drift times corresponds to the ions drifting back between the two GG wires which collect the ions (Figure 4.16). The smaller one at about 8–10 % higher drift times represents the ions which move around the GG wires and then escape into the drift volume. In the Ne-based gas mixtures, the ions start to enter the drift volume after about 113–135 μs in the IROC and 103–120 μs in the OROC. The ions in the Ar-based mixtures start to escape after about 310–325 μs in the IROC and 280 μs in the OROC.

The fraction of the collected and escaped ions in the IROC and OROC as a function of the time is shown is Figure 4.18 for the Ne- and Ar-based gas mixtures. It is obtained by integrating the respective distributions in Figure 4.17. For the collected ions, the curves show three shoulders corresponding to the different electrodes which are hit by the ions. In the OROC about 5–10 % less ions are collected by the pad plane and cathode wires, depending on the gas mixture and the anode wire voltages. The total number of collected ions is nearly the same comparing IROC and OROC and similar comparing the different gas mixtures. It takes about 140–160 μs to collect the full amount of ions in Ne and about 380 μs in Ar.

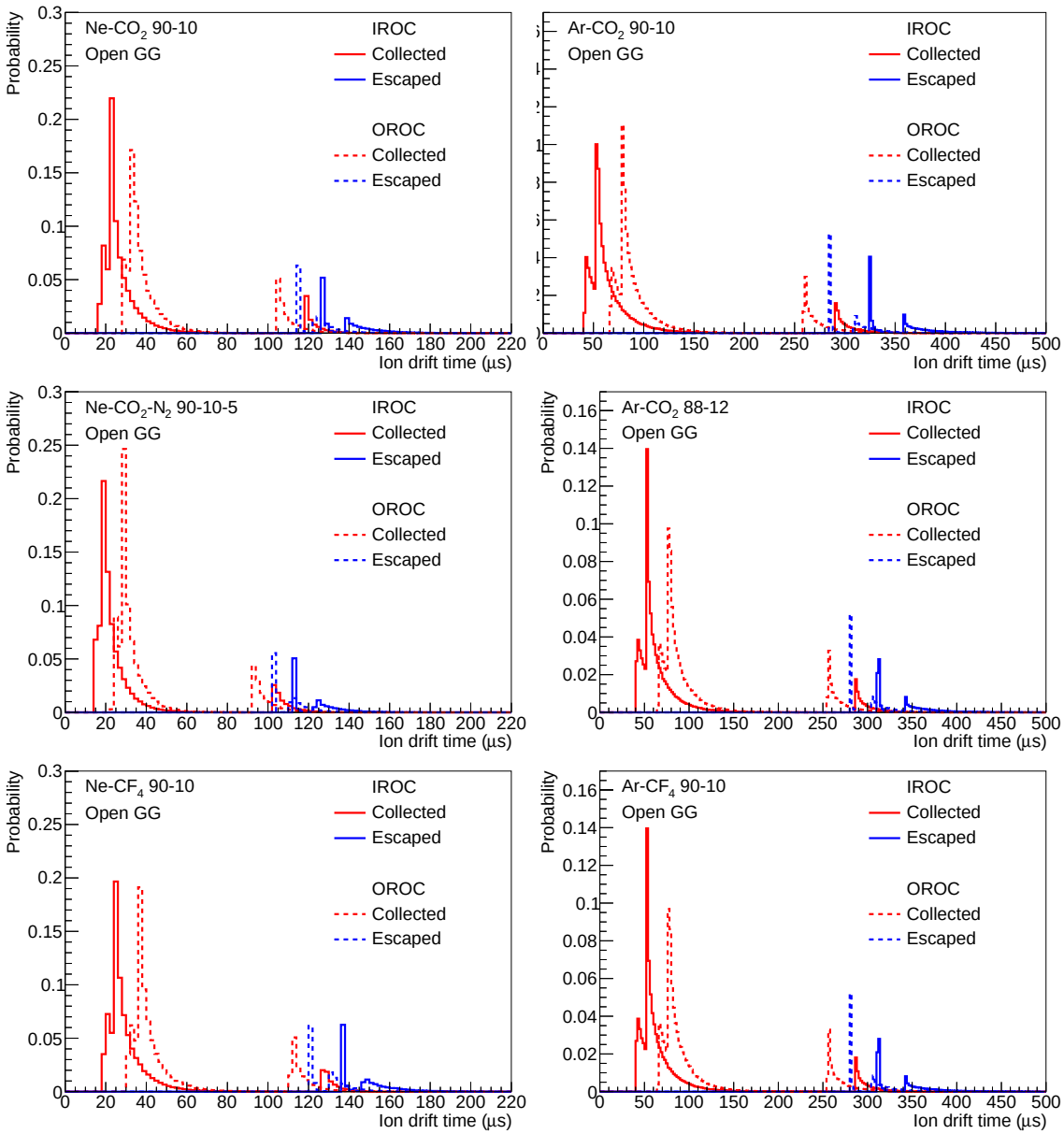

Figure 4.17: The total distribution of collected ions and ions escaped into the drift volume in the IROC and OROC with an open gating grid as a function of the ion drift time for the different Ne-based (left) and Ar-based (right) gas mixtures.

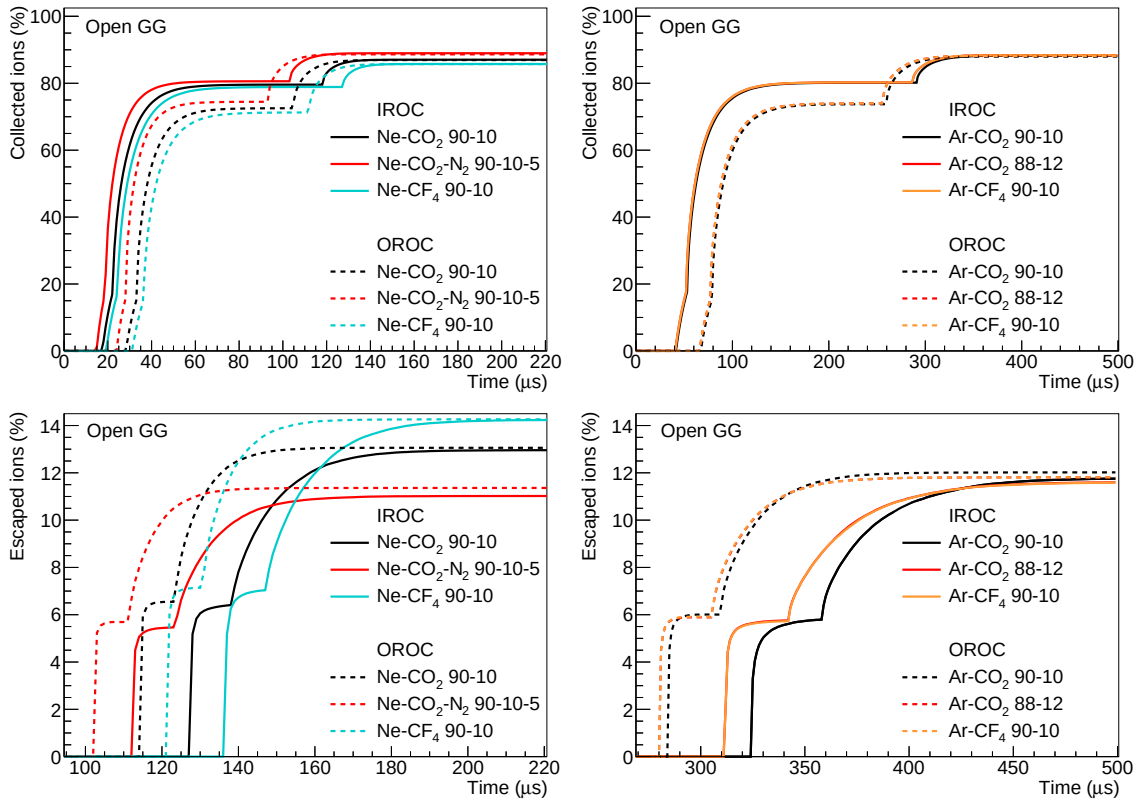

Figure 4.18: The fraction of collected ions (top) and escaped ions (bottom) in IROC and OROC with an open gating grid as a function of the time for the Ne-based (left) and Ar-based (right) gas mixtures.

The fraction of escaped ions represents the different drift paths of the ions by means of two shoulders. The previously discussed differences of the drift times to the GG wires in the IROC and OROC are also observed in the various curves for all gas mixtures. The total fraction of escaped ions is of interest and defines the ion backflow in MWPCs which is listed in Table 4.8 for the Ne- and Ar-based gas mixtures. In general the ion backflow in the OROC is higher by a few tenths of percentage points. The differences of the anode voltages with the Ne-based gas mixtures result in relative differences of the ion backflow of 20–30 % as it varies between 11 % for Ne-CO_2-N_2 (90-10-5) and 14.2 % for Ne-CF_4. The ion backflow with the Ar-based mixtures is just below 12 %. The relative differences between the different gas compositions are within 2 %. An ion backflow of that order cannot be tolerated as the tracking performance of the TPC suffers significantly because of the resulting space-charge distortions (Section 5.3.1).

4.4 Conclusions

The two Ar-CO_2 gas mixtures with a CO_2 fraction of 10 % and 12 % qualify for the application in the ALICE TPC in LHC Run 2. Their electron transport properties are of the same order as for Ne-CO_2 (90-10) and Ne-CO_2-N_2 (90-10-5) which

Gas		Ion backflow (%) IROC	OROC
Ne-CO_2	90-10	13.0	13.1
Ne-CO_2-N_2	90-10-5	11.0	11.4
Ne-CF_4	90-10	14.2	14.3
Ar-CO_2	90-10	11.8	12.0
	88-12	11.6	11.8
Ar-CF_4	90-10	11.6	11.8

Table 4.8: The ion backflow in IROC and OROC with an open gating grid for the Ne- and Ar-based gas mixtures.

were used during Run 1, thus not significantly affecting the drift of the ionization electrons. On the other hand, the ion mobilities in Ar-based gas mixtures are lower than in Ne. As a consequence, the ions created during the ionization processes are present in the drift volume for a longer period of time. In addition, the amount of ionization along the particle trajectories increases by a factor of two in the Ar mixtures leading to twice as many ions in the drift volume. The resulting drift field distortions are expected to increase compared to the Ne-based mixtures in which they are of the order of the position resolution of the TPC.

Regarding the ions created in the amplification region, the collection at the pad plane, cathode wires and gating grid is also slower by a factor of about 2.5 in Ar-CO_2 compared to Ne-CO_2 (90-10) and Ne-CO_2-N_2 (90-10-5). The ion-collection time increases from 180–190 μs in Ne to 490 μs in Ar which puts a harder intrinsic limitation to the maximum TPC event rate. The ion-collection time can be improved to 400–450 μs by adjusting the potentials at the GG wires or opening the gating grid earlier. The latter implies that about 1 % of the ions from the amplification region drift back into the drift volume and further increase the drift field distortions.

5 Space-Charge Effects

As particles traverse the active volume of the TPC and ionize the gas, the ionization electrons drift towards the readout chambers within 100 μs in the gas mixtures used. The positive ions on the other hand are about a factor 10^3 slower than the electrons. Therefore, it takes about 100 ms until the ions in the drift volume are completely evacuated. In the high multiplicity environment of Pb-Pb collisions, the large number of ions starts to accumulate as space-charge in the drift volume with increasing interaction rates, which leads to distortions of the uniform drift field. Disregarding fluctuations and the event topology, the space-charge density is symmetric in φ and depends on the radial and longitudinal position in the drift volume because the track density varies with the radius and z-position. The resulting electric field has a component in radial and z-direction. Because of the magnetic field there is also an $\mathbf{E} \times \mathbf{B}$ effect implying space-charge distortions in r-, $r\varphi$- and z-direction. As the path of the ionization electrons is affected, the precise reconstruction of their initial coordinates is no longer possible leading to a decrease of the position resolution and potential deterioration of the tracking performance. In addition, ions created by charged particles in the readout chambers from previous events drift back into the drift volume. Their contribution to the space-charge effect is about as high as the one from the ionization in the drift volume [45]. Neglecting a potential gating grid leakage due to floating wires, those two effects are the main sources of space-charge in the present TPC.

In the amplification region of the readout chambers each ionization electron is multiplied by the gain factor, leading to the same number of ions. The ions are collected by the cathode and GG wires of the MWPCs to prevent them from entering the drift volume. For Run 3 the readout chambers of the TPC will be upgraded (Section 3.2). The MWPCs will be replaced by four-GEM detectors. The intrinsic ion blocking capability of one single GEM is of the same order as for MWPCs, but a combination of four GEMs on top of each other is capable of significantly reducing the ion backflow by about one order of magnitude. Considering the expected interaction rates of 50 kHz for Pb-Pb collisions in Run 3, even the desired ion backflow of 1 % leads to a substantial accumulation of ions from the amplification zone in the drift volume. These ions outnumber those from the primary and secondary ionization processes by the factor $\varepsilon = \text{IBF} \times \text{Gain}$ and become the dominant source of

space-charge effects. Because of local gain variations and the dead zones between the readout chambers, the space-charge density fluctuates in φ which adds further r- and $r\varphi$-components to the space-charge distortions. The magnitude of the distortions which are expected for the upgrade of the TPC in Run 3 are discussed in Section 5.2.

Similar space-charge effects can be studied with the MWPCs in the present TPC leaving the gating grid permanently open. Since the ion backflow is significantly higher in this scenario (Section 4.3.3), the beam conditions have to be adjusted accordingly since the space-charge density depends on the ion backflow, interaction rate and the number of tracks per event. A set of real data with space-charge distortions comparable to those expected for Run 3 is extremely useful for the verification of current models. Furthermore the performance of correction schemes which are developed for the TPC upgrade can be tested on data. Therefore, the gating grid of the TPC was operated in the open state during a dedicated data taking period at the end of Run 1 in 2013 to mimic the space-charge effects of the upgraded TPC. The observed space-charge distortions are analyzed and discussed in Section 5.3.

The analysis of the space-charge effects is performed with the ALICE offline analysis framework AliRoot [46] which is based on the ROOT framework [47].

5.1 Calculation of Space-Charge Distortions

The general concept to calculate the distortions of the drifting electrons consists of two steps. First, the deviations of the electric field ΔE_{r}, ΔE_{φ} and ΔE_{z} due to the space-charge density $\rho_{\mathrm{SC}}(r, \varphi, z)$ of the positive ions are calculated by solving the Poisson equation

$$\Delta\phi = \frac{\rho_{\mathrm{SC}}}{\epsilon} \,, \tag{5.1}$$

where ϕ is the electric potential field and ϵ is the permittivity. A customized version of the Poisson relaxation method is implemented in AliRoot and used to calculate the field deviations [35]. In the second step, the distortions of the electrons along their drift path $\mathrm{d}r$, $\mathrm{d}\varphi$ and $\mathrm{d}z$ are obtained with the solution of the Langevin equation (Equation (3.3)) which can be provided by a simplified integral technique in case the magnetic field is nearly parallel to the electric field or by detailed algorithms like Euler or Runge-Kutta [48, 49].

A simplified parameterization of the space-charge density expected for the ALICE TPC is derived in [50] and modified in [35] to take the effect of the ion backflow into account:

$$\rho_{SC}(r, z) = \frac{a - bz + c\varepsilon}{r^d} \,. \tag{5.2}$$

The factors a, b, and c depend on the characteristics of the experiment and describe the detector geometry, gas properties, interaction rate, particle multiplicity and certain scaling factors to make it applicable for the ALICE TPC. The radial dependence is extracted from data with a value for d between 1.5 and 2 [35]. Neglecting the effect of local gain variations and dead zones between chambers in case of ion backflow, the space-charge density is symmetric in φ and linear in z due to the constant ion drift velocity. It is proportional to ε which describes the number of ions drifting back into the drift volume for each ionization electron entering the amplification region.

5.2 Expected Space-Charge Distortions for the TPC Upgrade

The space-charge density depends on the interaction rate, ion backflow and the drift time of ions in the drift volume, which is taken into account in Equation (5.2). Interaction rates up to 50 kHz for Pb-Pb collisions are expected in Run 3, increasing the number of ions from ionization due to particle collisions with the gas atoms. However, the space-charge density is determined to a large degree by the ion backflow introduced by the GEM readout chambers. For an ion drift time of 160 ms and the expected interaction rates, ions of 8000 events are accumulated in the drift volume at any given moment. Minimizing the ion backflow is, therefore, crucial to provide a sufficient tracking performance. Varying several parameters of a four-GEM detector during the comprehensive R&D program, an ion backflow below 1 % is achieved in [35] and [36]. The resulting space-charge distortions in the TPC drift volume are also studied and discussed in [35].

The average space-charge density for an interaction rate $R_{\text{int}} = 50\,\text{kHz}$ is calculated with Equation (5.2) using Ne-CO_2-N_2 (90-10-5). The ion backflow of 1 % results in an ε-factor of 20, assuming an effective gain of 2000 for the GEM readout chambers. The expected space-charge density is illustrated in Figure 5.1 as a function of the radius and z. It generates the highest values near the central electrode at small radii as the highest track densities are also found in this region. The muon absorber leads to a 10 % smaller space-charge density on the C-side, explaining the step at $z = 0$. In addition to the previously mentioned space-charge fluctuations in φ, variations of the number of events per unit time and the number of tracks per event lead to further space-charge density fluctuations which are not taken into account here. The significance of the space-charge fluctuations is studied in [35].

The resulting electric field inside the TPC drift volume deflects the drift path of the ionization electrons in radial and z-direction towards regions with lower field

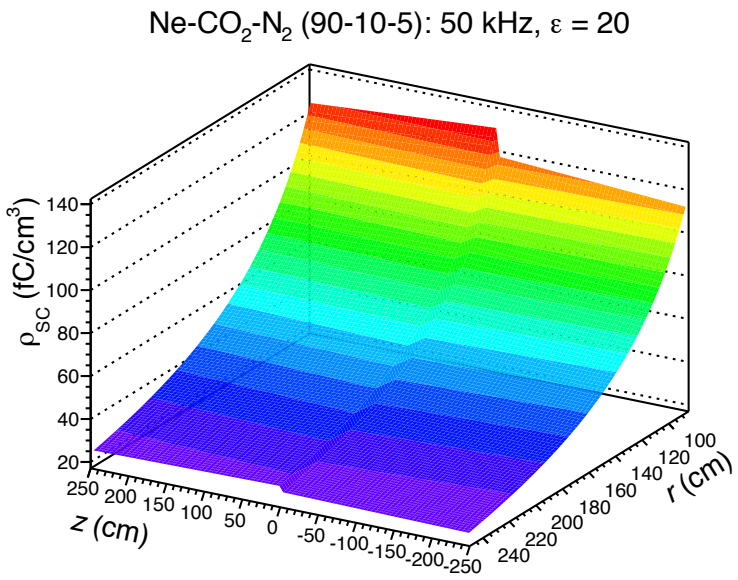

Figure 5.1: The average space-charge density ρ_{SC} for Ne-CO_2-N_2, $R_{\text{int}} = 50\,\text{kHz}$ and $\varepsilon = 20$ as a function of r and z [35].

gradients. The combination of the radial electric field and the magnetic field cause additional distortions in the $r\varphi$-direction due to the $\mathbf{E} \times \mathbf{B}$ effect. The magnitude of the expected space-charge distortions is calculated in [35] using the space-charge density in Figure 5.1. Figure 5.2 shows the distortions dr, d$r\varphi$ and dz for Ne-CO_2-N_2 (90-10-5), $R_{\text{int}} = 50\,\text{kHz}$ and $\varepsilon = 20$ as a function of the radius and z-position of the ionization electrons. The biggest distortions are observed in the r- and $r\varphi$-direction, which influences the precise calculation of the transverse momentum. The radial distortions are below 10 cm in most of the volume of the TPC. The space-charge field has a focusing effect on the electrons as they are drawn to bigger radii in the inner part of the TPC and to smaller radii in the outer part. The $r\varphi$-distortions are below 2 cm in a large part of the TPC. They are correlated to the radial distortions and their sign depends on the polarity of the magnetic field.

The strongest effects are observed near the central electrode and at the inner field cage. The radial profile of the r- and $r\varphi$-distortions in this region is shown in Figure 5.3. Distortions in radial direction of up to 19 cm at the inner field cage and 10 cm at the outer field cage are expected. The largest $r\varphi$-distortions assume values of 7 cm at the inner field cage.

The precise reconstruction of space points and tracks in an environment with the space-charge distortions discussed requires an accurate calibration and correction scheme which is presented in [35]. In a first step, an average space-charge map is applied for a coarse correction of the measured clusters. The average map is updated several times per fill and takes variations of the luminosity, ambient conditions and the status of the readout chambers into account. In addition it is scaled to

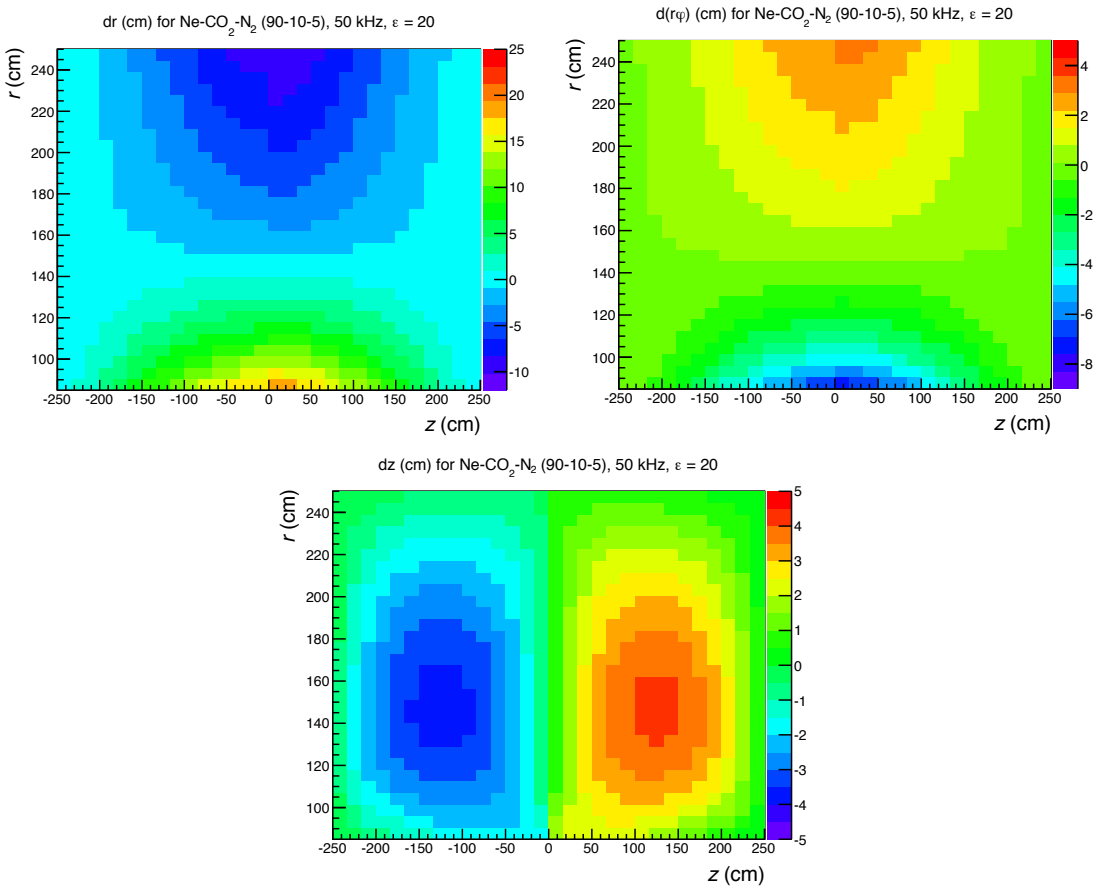

Figure 5.2: The expected space-charge distortions dr (top left), d$r\varphi$ (top right) and dz (bottom) for Ne-CO_2-N_2 (90-10-5), $R_{\text{int}} = 50\,\text{kHz}$ and $\varepsilon = 20$ as a function of the radius and z-position [35].

the current ion density based on the measurement of the instantaneous ion current. Therefore, fluctuations of the number of events contributing to the space-charge density are taken into account. The residuals after this correction are of the order of the cluster resolution and allow an efficient cluster-to-track association. For the second step a high-resolution map is applied which also contains topological fluctuations in r and $r\varphi$. The information of the external detectors is used for an interpolation of ITS and TRD track segments and combined with the information of the TPC space points to create a correction map with sufficient spatial and time granularity. The residuals remaining after the second correction are of the order of the intrinsic spatial resolution of the TPC or smaller.

5.3 Space-Charge Distortions with an Open Gating Grid

The expected space-charge distortions in the upgraded TPC pose new challenges for the TPC operation, detector calibration and data reconstruction. The applied space-charge models are under continuous development to further improve the un-

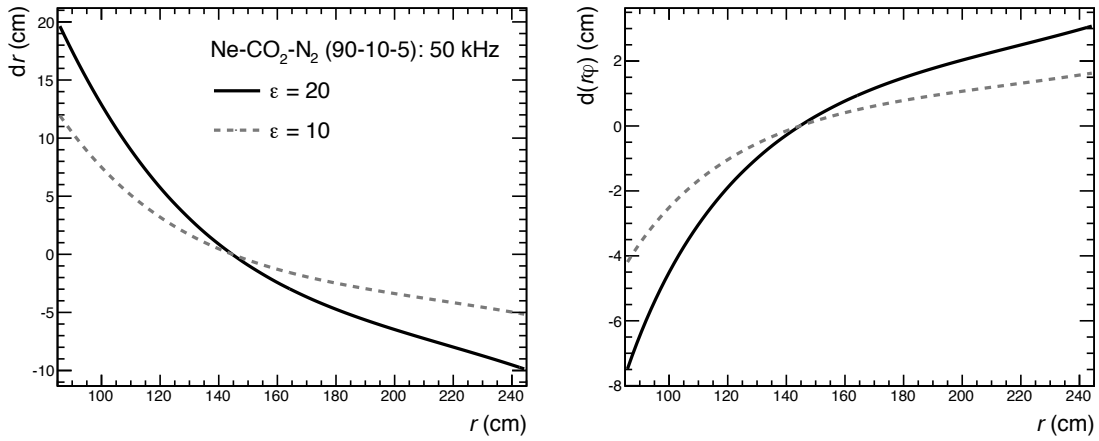

Figure 5.3: The expected space-charge distortions dr (left) and d$r\varphi$ (right) for Ne-CO_2-N_2 (90-10-5), $R_{\text{int}} = 50\,\text{kHz}$ and $\varepsilon = 20$ as a function of the radius. The distortions for $\varepsilon = 10$ are included and drawn with the dashed line [35].

derstanding and description of the space-charge effects. As a contribution to this development, a set of real data is analyzed which was taken at the end of LHC RUN 1 in similar conditions in the TPC as are expected for RUN 3.

In order to provide similar ion densities in the drift volume for the present TPC, the gating grid of the MWPCs was operated in the open state permanently during one dedicated run. The space-charge density depends on the number of ions drifting from the amplification region into the drift volume, the ion mobilities in the gas, the interaction rate and the particle multiplicity per event. The ion mobility is the same in RUN 1 and RUN 3 as the gas mixture Ne-CO_2-N_2 (90-10-5) is used in both LHC running periods. The ion backflow of the GEM readout chambers is of the order of 1 % resulting in $\varepsilon = 20$ at a gain of 2000. The MWPCs have an ion backflow of 11 % (Section 4.3.3) and are operated at a gain of about 7000. This implies $\varepsilon = 770$ which is about a factor 40 higher than for GEMs. The remaining free parameters are the collision system and the interaction rate. Assuming that the number of tracks per event N_{ch} is 100 times higher in Pb-Pb collisions, pp collisions at an interaction rate of $R_{\text{int}} = 200\,\text{kHz}$ result in space-charge densities in the present TPC which are of the same order of magnitude as expected in the upgraded TPC:

$$\frac{\rho_{\text{SC, open GG}}}{\rho_{\text{SC, RUN 3}}} \sim \frac{(\varepsilon \times R_{\text{int}} \times N_{\text{ch}})_{\text{open GG}}}{(\varepsilon \times R_{\text{int}} \times N_{\text{ch}})_{\text{RUN 3}}} \sim 1\,. \tag{5.3}$$

Table 5.1 provides a summary of the run conditions of the dedicated run with an open gating grid. One OROC on the C-side of the TPC is completely switched off during this run. A major impact on the space-charge densities in the neighboring regions is expected as a consequence which is discussed in Section 5.3.2.

Run number	197470
Run period	LHC 13g
Run duration	21 min
LHC fill number	3555
Collision system	pp
CMS energy $\sqrt{s}$	2.76 TeV
Interaction rate R_{int}	$\sim$ 200 kHz
B-field polarity	$--$
Total number of events	926 144
Number of events in TPC	876 520
TPC status	OROC C08 off

Table 5.1: The run conditions of the dedicated run in which the TPC is operated with an open gating grid. It was taken at the end of RUN 1 in 2013.

The raw data is reconstructed by using the common tracking algorithms. In particular, no corrections for the expected space-charge distortions are applied which makes an efficient assignment of found clusters to tracks very challenging. The achieved tracking performance of the TPC is discussed in Section 5.3.1. The original approach to determine the distortions uses interpolations of ITS and TRD or TOF tracks and compares these to the reconstructed TPC space points, similarly as in the second step of the proposed correction scheme for the TPC upgrade (Section 5.2). Because of the results presented in Section 5.3.1, an alternative approach is used to measure the space-charge distortions in Section 5.3.2. The measured distortions are compared to current model calculations in Section 5.3.3.

5.3.1 TPC Tracking Performance

An accurate determination of the distortions requires the precise reconstruction of space points and tracks in the TPC. Ideally 159 clusters are assigned to each track, one cluster in each pad row. In reality this is not always the case as the average number of clusters per track is of the order of 140 clusters. Since in the nominal case the distortions are of the order of the position resolution, the search window for cluster candidates is limited to ± 1 cm in $r\varphi$ with respect to the estimated track position. Regarding the large space point distortions in the open gating grid data, the number of clusters per track is expected to decrease since no distortion correction is applied. Therefore, the cluster-to-track association provides a meaningful estimate on the tracking performance of the TPC in the environment of significant space-charge distortions.

In Figure 5.4, the cluster-to-track association for the open gating grid data and for a reference data set without distortions are compared. The normalized distributions show the number of clusters which are assigned to TPC tracks as a function

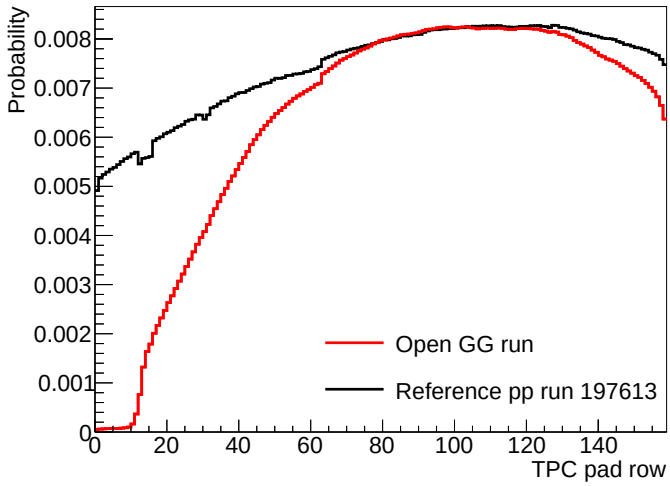

Figure 5.4: The normalized radial distributions of the clusters in the TPC which are associated with tracks pointing to the nominal vertex within the full TPC acceptance. The shape of the distribution for the open gating grid run is compared to the one for some reference data without distortions. The distribution for the reference run is scaled to match the magnitude of the distribution for the open gating grid data.

of the TPC pad row. The distribution of the reference data is scaled to match the magnitude of the distribution of the open gating gird data. A cut on the direction of the tracks is applied to take only those tracks into account which point to the nominal vertex. Another cut selects those tracks which are in the full acceptance of the TPC ($|\eta| < 0.9$).

Significant differences in the shape of the two curves are observed. The reference data has a roughly flat distribution of assigned clusters. For the open gating grid data, the cluster-to-track association is comparable to the reference data in regions where only small distortions are expected (Figure 5.3). This region covers quite a large range of radii as almost no deterioration of the cluster-to-track association is observed between pad rows 50 and 145, demonstrating the robustness of the tracking algorithm. As the distortions are expected to get larger towards the inner and outermost radii, a change of the slope of the distribution indicates a constant decrease in the number of assigned clusters for the open gating grid data. This behavior is in agreement with large distortions of the clusters as more and more clusters move outside of the tracking window and are not considered to belong to the respective tracks. The effect is observed up to the outer field cage and down to pad row 15. Between this pad row and the inner field cage the largest radial distortions are expected. A steep drop of the number of clusters associated with tracks to zero is observed implying that the ionization electrons from the selected tracks do not end up in the first 15 pad rows. Therefore, an estimate of the radial distortions of electrons which travel the full drift length can be extracted. Considering the length of the pads, the observed radial distortions in the open gating grid run amount to

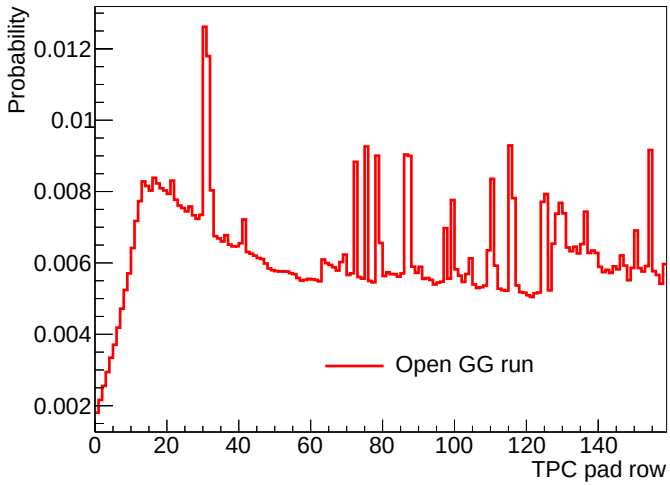

Figure 5.5: The normalized radial distribution of all clusters which are measured in the TPC. The spikes at some pad rows are attributed to noise effects.

11.25 cm at the inner field cage near the central electrode and are more than half as large as the expectations for the TPC upgrade.

The effect of the large radial distortions near the inner field cage is also observed in the normalized distribution of all clusters measured in the TPC which is shown in Figure 5.5. Disregarding the spikes at some pad rows which are attributed to noise, the distribution is nearly flat down to pad row 50 and rises down to pad row 20. Between pad row 15 and the inner field cage, a steep decrease of the number of measured clusters indicates large radial distortions similar to the observation in the distribution of clusters assigned to tracks. The radial cluster position is shifted towards higher radii as the distribution shows a small peak structure around pad row 15.

Considering the low cluster-to-track association efficiency observed in Figure 5.4, the number of reconstructed space points for each TPC track decreases compared to the common case without major space-charge distortions. The TPC tracks are propagated only to some point towards the inner and outer part of the TPC resulting in a decrease of the length of the reconstructed tracks. As a consequence, the precision of the transverse momentum calculation and of the track extrapolation suffers significantly which is crucial for the track matching with the external detectors. The track matching efficiencies of TPC tracks to the ITS and TOF are shown in Figure 5.6 as a function of the ratio of the charge of the particle and the measured transverse momentum q/p_{T}. Usually, matching efficiencies with the ITS of the order of 95 % are achieved. A significant decrease is observed in the open gating grid data for all q/p_{T} down to 60.2 % on average. The track matching efficiency with the TOF drops to 30.1 % on average.

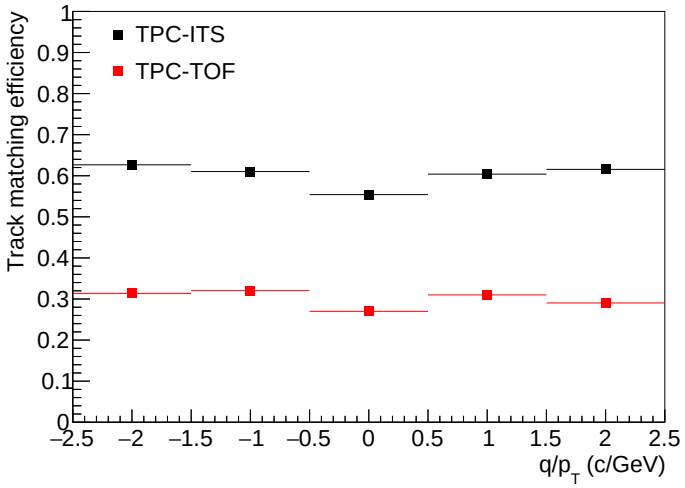

Figure 5.6: The matching efficiencies of the TPC tracks with the ITS and TOF as a function of q/p_{T} for the open gating grid data. The statistical uncertainties are smaller than the size of the data points. In the nominal scenario without distortions, track matching efficiencies with the ITS of the order of 95 % are achieved.

5.3.2 Magnitude of the Space-Charge Distortions

For a comparison to the expected space-charge distortions for the TPC upgrade and to current models, the quantification of the observed distortions in the open gating grid run is performed. A method similar to the second step of the proposed Run 3 correction scheme (Section 5.2) proves to be insufficient for this task. It is demonstrated in Section 5.3.1 that only clusters in the regions of smaller distortions are assigned to TPC tracks. Furthermore the track matching efficiencies to the external detectors significantly decrease due to the low cluster-to-track association efficiency. Thus a comparison of the interpolated tracks from the external detectors and the TPC space points only provides a measurement of the smallest distortions as the clusters which are strongly distorted are disregarded. Also the available statistics are not fully exploited as only a fraction of the available tracks can be used due to the inefficient track matching.

An alternative approach to measure the observed space-charge distortions uses the reconstructed ITS tracks provided by the ITS standalone tracker. These tracks are not affected by the space-charge in the TPC but are only reconstructed up to the outermost layer of the ITS at a radius of 43 cm. The deviation in $r\varphi$ of the extrapolated ITS tracks to all clusters measured in the TPC, regardless weather they are associated with a track or not, is calculated. The tracking coordinate system of each ITS track is, if possible, rotated to the coordinate system of each cluster (Figure 5.7). The ITS track is extrapolated to the radial position (x_{local}) of the cluster. A 5-dimensional histogram is filled with the deviation $\Delta_{r\varphi} = y_{cluster} - y_{track}$ and the coordinates of the cluster, expressed in terms of the radius r, the TPC sector

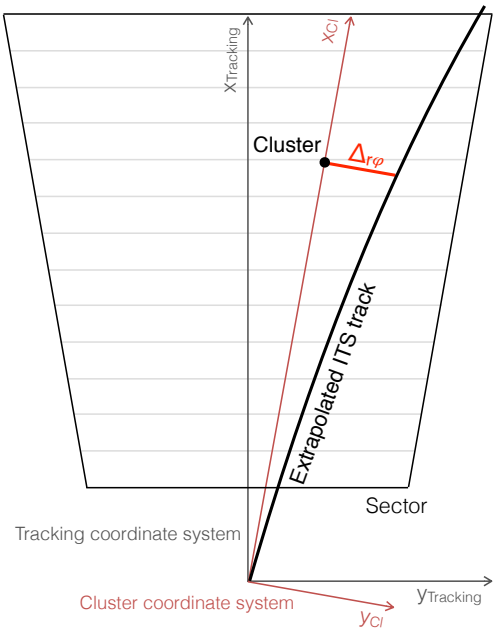

Figure 5.7: A sketch of the method to provide the measured distortions $dr\varphi'$. The tracking coordinate system of the ITS track is rotated to the cluster coordinate system. The ITS track is extrapolated to the cluster radius x_{cluster}, the deviation $\Delta_{r\varphi}$ is measured and filled into a histogram together with the cluster coordinates and the q/p_{T} of the ITS track.

and z-position, as well as the track q/p_{T} of the ITS track. The resulting histograms provide a $\Delta_{r\varphi}$-distribution of clusters belonging to tracks with a combinatorial background of other clusters. A reduction of the background is achieved by limiting the windows in $r\varphi$ and z to $|\Delta_{r\varphi}| < 10\,\text{cm}$ and $|\Delta_z| < 10\,\text{cm}$. The distributions are fitted in each bin to extract the measured distortions $\text{d}r\varphi'$.

Figure 5.8 shows four examples of the obtained $\Delta_{r\varphi}$-distributions for different positions in the TPC and different q/p_{T}. The distributions are fitted with a function consisting of the sum of a Gaussian and a linear polynomial. The mean value of the fit function corresponds to the measured distortions $\text{d}r\varphi'$. At small radii a clear peak is observed whereas towards bigger radii and z the statistics in each bin decrease. The precision in $r\varphi$ of the extrapolated ITS tracks decreases towards bigger radii. It is of the order of 1 mm at the inner field cage and of the order of 1 cm at the largest TPC radii, depending on the q/p_{T} of the track [35]. The uncertainties of the measured distortions are strongly correlated with the precision of the ITS track extrapolation and the available statistics and increases with bigger radii. The distribution of the width σ of the Gaussian peak is examined to make an estimate on the uncertainties of the measured distortions. The normalized distribution and the average $\langle\sigma\rangle$ as a function of the radius are shown in Figure 5.9. The sigma of the fitted $\Delta_{r\varphi}$-distributions reaches relatively large values up to 6 cm. These values correspond to regions with the least statistics making it difficult for the fit to converge.

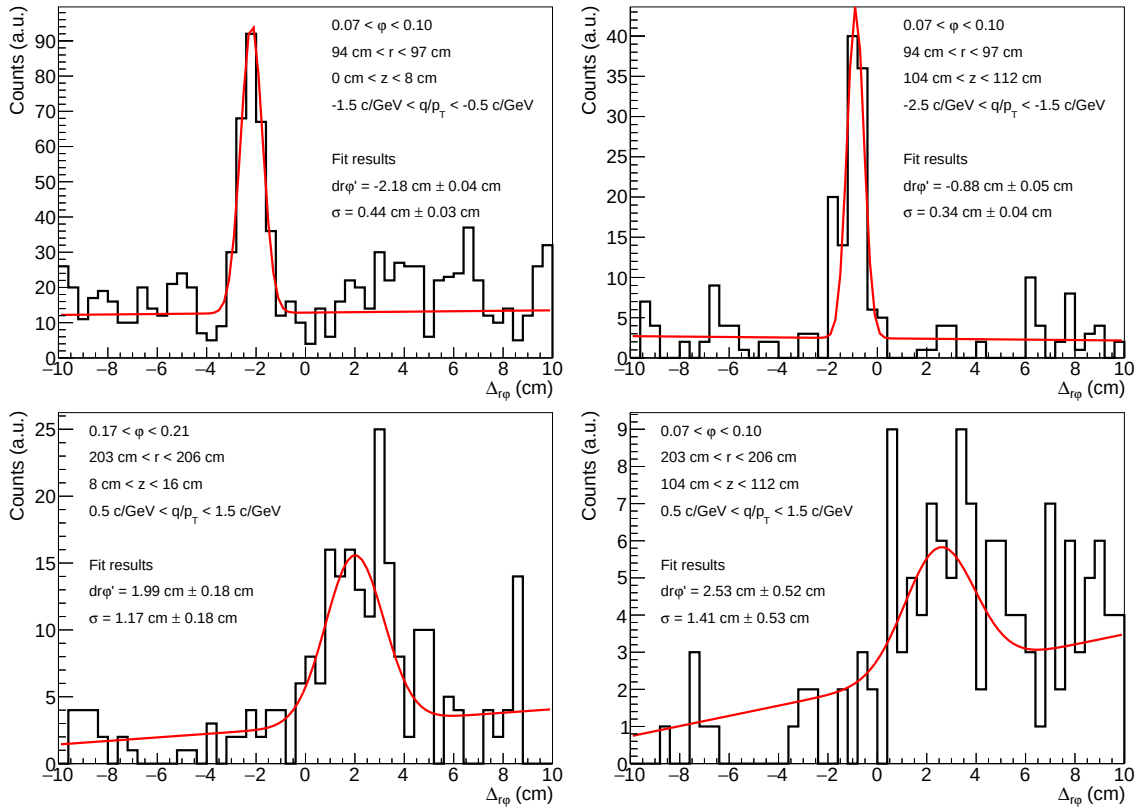

Figure 5.8: The measured distribution $\Delta_{r\varphi}$ of extrapolated ITS tracks to all clusters found in the TPC. Four examples are shown at four different positions in the TPC and different q/p_{T}. The distributions are fitted with the sum of a Gaussian and a linear polynomial. The mean value of the fit function corresponds to the measured distortions $\mathrm{d}r\varphi'$.

The radial dependence of the average sigma corresponds to the rising extrapolation errors. At the innermost radii the average width of the fitted peak is of the order of 7 mm and it increases up to 2.3 cm at the outer field cage, resulting in quite large uncertainties of the measured distortions.

The measurement of the distortions is provided by the deviation in $r\varphi$ of the distorted cluster to the respective track at the position of the distorted cluster. The actual distortions with respect to the position where the cluster is created, which is shifted in r due to the radial distortions, cannot be measured directly. The real distortions $\mathrm{d}r$ and $\mathrm{d}r\varphi$ are correlated with the measured distortions $\mathrm{d}r\varphi'$ by the linear equation

$$\mathrm{d}r\varphi' = \mathrm{d}r\varphi + \mathrm{d}r \cdot \tan\alpha\,, \tag{5.4}$$

where α is the inclination angle of the track with respect to the pad rows [35]. A sketch illustrating this correlation is shown in Figure 5.10. For straight tracks with high transverse momentum which are perpendicular to the pad row, the measured and real distortions in $r\varphi$ are identical but the radial distortions cannot be measured. As soon as the track is inclined with respect to the pad row or has a curvature due

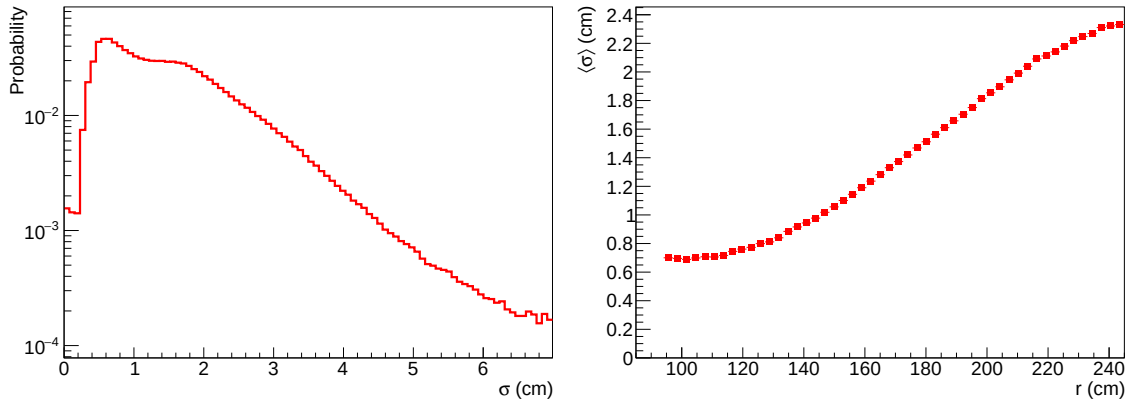

Figure 5.9: The normalized σ-distribution obtained by the fit results of the $\Delta_{r\varphi}$-distributions (left) and the average $\langle\sigma\rangle$ as a function of the radius r (right). The fit function is the sum of a Gaussian and a linear polynomial.

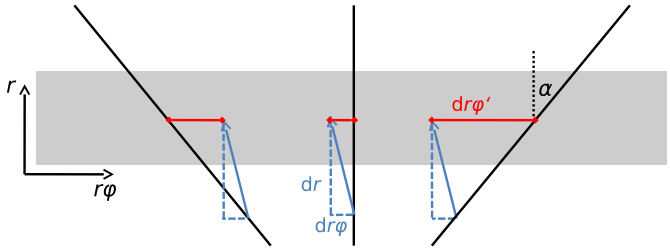

Figure 5.10: The measured distortions $\mathrm{d}r\varphi'$ vary with the inclination angle α of the track. The real distortions $\mathrm{d}r$ and $\mathrm{d}r\varphi$ can be extracted from the measured ones via Equation (5.4) [35].

to the charge of the particle and its transverse momentum, the measured distortions $\mathrm{d}r\varphi'$ depend on the inclination angle of the track. Thus measuring the distortions for tracks with different inclination angles allows to disentangle the real distortions from the measured ones via Equation (5.4). The inclination angle α can be expressed in terms of the radial position r and the radius of the curvature R_C of the track with

$$\sin\alpha = \frac{r}{R_\mathrm{C}} = r \cdot \frac{qB}{p_\mathrm{T}} \,. \tag{5.5}$$

The radius of the curvature depends on the magnetic field strength B and the q/p_T of the track. A measurement of the distortions as a function of q/p_T, therefore, provides the inclination angle and the possibility to extract the real distortions.

The final results for the measured distortions $\mathrm{d}r\varphi'$ near the central electrode as a function of the radius are shown in Figure 5.11 for five different q/p_T ranges and averaged over all q/p_T. They are averaged over all TPC sectors excluding sectors

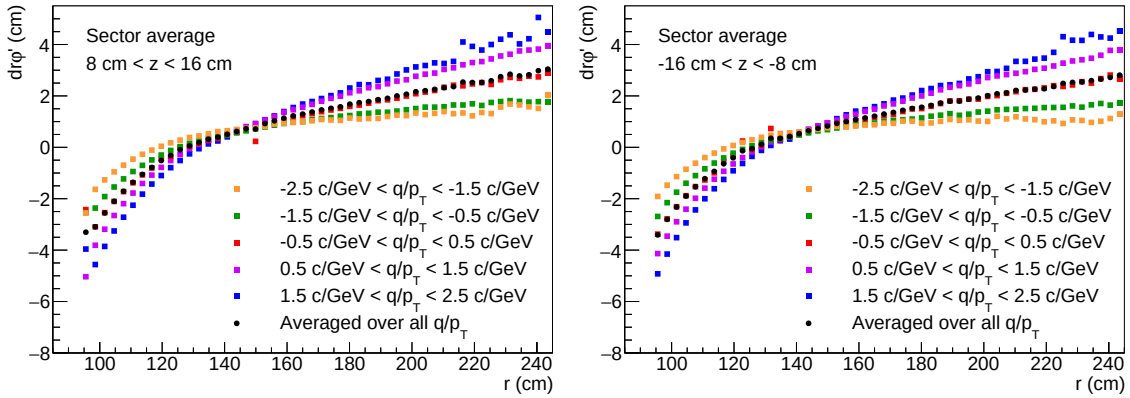

Figure 5.11: The measured distortions $\mathrm{d}r\varphi'$ near the central electrode as a function of the radius r for A-side (left) and C-side (right) and different q/p_T ranges.

7, 8 and 9 on the C-side because OROC C08 is switched off. The data points show the expected q/p_T dependence as differences of about a factor two are observed at the innermost and outermost radii. The average over all q/p_T is nearly equal to the high-p_T points which correspond to approximately straight tracks. The fluctuations of the points with increasing radius, especially for low p_T, correspond to the uncertainties of the measured distortions due to the extrapolation uncertainties of the ITS tracks and decreasing statistics. Considering the average values, distortions of the order of 3–3.5 cm in $r\varphi$ are measured at the inner and outer field cage which is a factor two lower than the calculated $r\varphi$-distortions for the TPC upgrade and $\varepsilon = 20$ in Figure 5.3. The radial dependence of the data points is very similar to the results of the simulations. The sign of $\mathrm{d}r\varphi'$ changes with the sign of the radial distortions since the major source is the $\mathbf{E}\times\mathbf{B}$ effect due to the radial distortions in the presence of a magnetic field. The intersection point of the curves for the data is at $\mathrm{d}r\varphi' = 0.6\,\mathrm{cm}$ whereas in the simulation it is at zero. This indicates fluctuations in the space-charge density in $r\varphi$ as expected due to local gain variations and dead zones between chambers. These fluctuations result in additional r- and $r\varphi$-components of the distortions which is not the case for a φ-symmetric space-charge density as assumed in the simulations.

Figure 5.12 shows the average of the measured distortions in $r\varphi$ as a function of the radius and z-position. At the smallest radii the bins are empty because the clusters are distorted in radial direction and start to end up at a radius of about 95 cm in the readout chambers. Averaging over all sectors and q/p_T reduces the uncertainties observed in individual bins as the measured distribution is smooth in most regions. In a large part of the TPC the measured distortions are smaller than 1.5 cm. The largest distortions are observed at the inner and outer field cage as expected. A small asymmetry between A- and C-side is observed due to the muon absorber on the C-side. In general, the shape of the measured and average

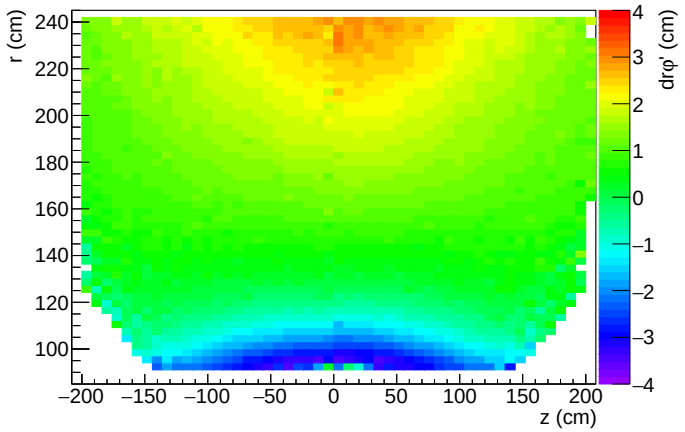

Figure 5.12: The measured distortions $\mathrm{d}r\varphi$ as a function of the radius r and z-position of the measured cluster. The results are averaged over all sectors, excluding sector 7, 8 and 9 on the C-side, and over all q/p_{T}.

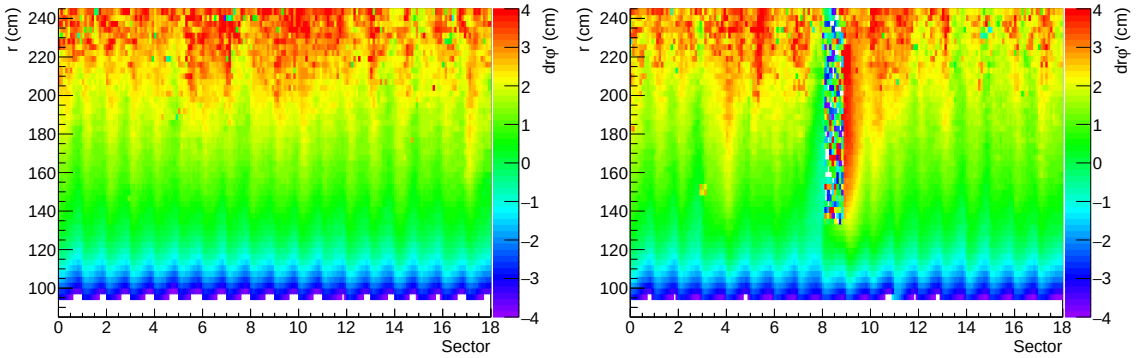

Figure 5.13: The measured distortions $\mathrm{d}r\varphi'$ near the central electrode as a function of the radius r and the TPC sector for A-side (left) and C-side (right). They are averaged over all q/p_{T}.

space-charge distortions is very similar to the $r\varphi$-distortions in the TPC upgrade simulations (Figure 5.2).

The measured distortions as a function of the radius and the TPC sector near the central electrode are shown in Figure 5.13. They are averaged over all q/p_{T} bins. A variation of the distortions within each sector is observed. The effect is most significant at small radii below 120 cm. Due to larger uncertainties of the measured distortions at big radii the effect seems less pronounced in the OROCs but it is still visible to some extent. The origin of this φ-dependence are the fluctuations due to gain variations and dead zones between chambers. In the regions between two chambers the ion density is smaller than at the center of a sector. The resulting electric field in $r\varphi$-direction deflects the electrons at sector boundaries towards the center of the sector. Adding this effect to the $r\varphi$-distortions due to the radial distortions and the $\mathbf{E} \times \mathbf{B}$ effect results in a shift of the mean value of the φ-variation depending on the radius.

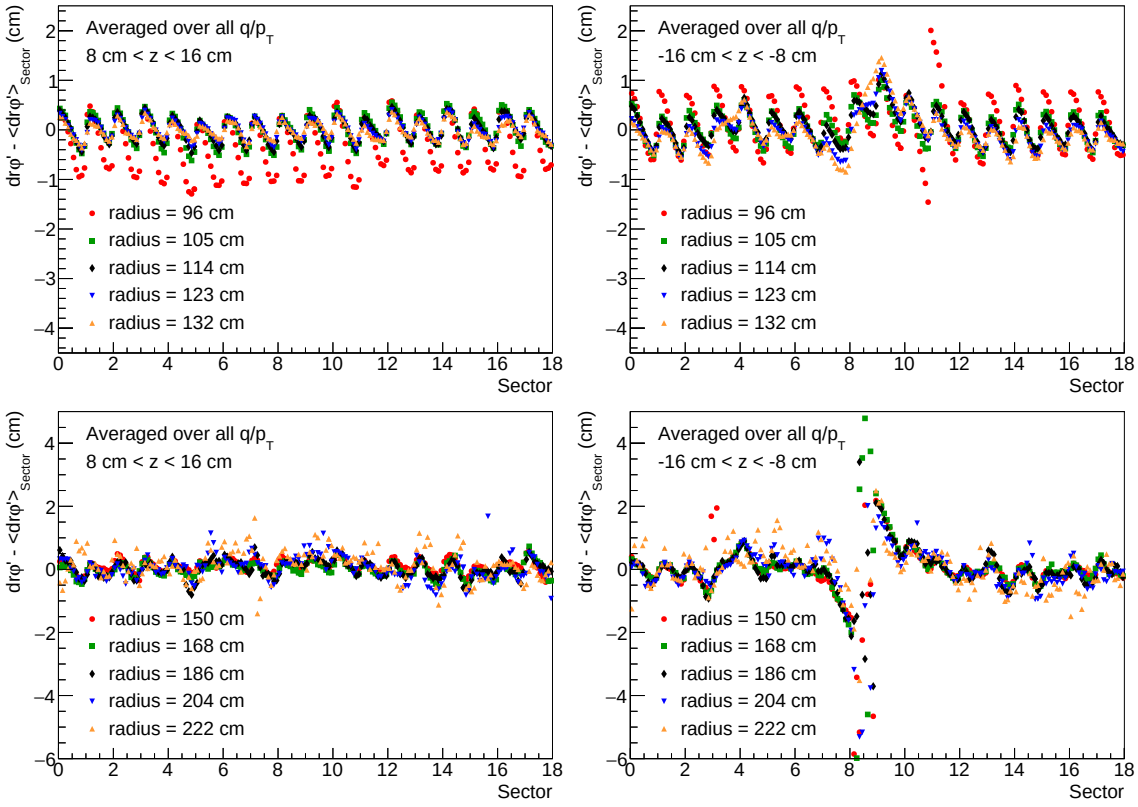

Figure 5.14: The difference between the measured distortions $\mathrm{d}r\varphi'$ and the average of all sectors $\langle \mathrm{d}r\varphi' \rangle_{Sector}$ near the central electrode as a function of the radius and the TPC sector for IROCs (top) and OROCs (bottom) as well as A-side (left) and C-side (right). The measured distortions are averaged over all q/p_{T}.

The significance of the φ-dependence is even better illustrated by calculating the difference of the measured distortions and the average over all sectors. In Figure 5.14 the difference $\mathrm{d}r\varphi' - \langle \mathrm{d}r\varphi' \rangle_{Sector}$ is plotted as a function of the sector for several radii in the IROC and OROC. The data points show a clear pattern as they oscillate around zero and precisely describe the effect. A small offset of the points for the smallest radius is observed due to a lack of statistics in some bins which increases the uncertainties. The uncertainties also increase towards the largest radii of the TPC as the fluctuations of the data points increase. However the significance of the effect in the OROC is comparable to the IROC considering the different axis ranges. On the A-side the results for all sectors are similar whereas on the C-side suspicious variations in the behavior of sectors 3–6 are observed. The source of these variations are the relatively large distortions measured in OROC C04 (Figure 5.13).

In both Figure 5.13 and Figure 5.14, the effect of one switched-off readout chamber is demonstrated for OROC C08. Since there is no ion backflow from this chamber the space-charge distortions in the neighboring regions are significantly affected. Due to the larger area of zero ion density the φ-variations become more significant in the adjacent chambers diminishing the distortions on one side of OROC C08 and

enhancing them on the other side. To some extent the distortion pattern in the neighboring IROCs is also affected by the switched off OROC.

5.3.3 Comparison to Model Calculations

As the magnitude of the distortions in the open gating grid run is determined, the data is compared to space-charge distortion calculations to provide valuable input on the validity and accuracy of the current model and calculation techniques. The calculations are performed by [51] and [52]. A similar approach is used as for the space-charge fluctuation studies in [35]. The space-charge density which serves as an input is constructed from the measured charge in the readout chambers of real data which defines the density distribution in r and φ. This distribution is assumed as one disc of ions drifting back into the drift volume. A specific number of such ion discs, according to the number of pileup events, is placed at a random z-coordinate to describe the density distribution in z. The resulting 3-dimensional space-charge density is corrected for the gain and scaled to the expected ε which is assumed to be $\varepsilon = 20$ for the TPC upgrade. Comparing the magnitude of the results obtained for the open gating grid data to the simulations in [35], input density maps scaled to $\varepsilon = 15$ are expected to describe the data. The calculation of the space-charge distortions is performed using the techniques in Section 5.1. Since the data provides the measured distortions $\mathrm{d}r\varphi'$, the model in Equation (5.4) is used to match the results of the calculations $\mathrm{d}r$ and $\mathrm{d}r\varphi$ to the results from the data.

The residuals after subtracting the calculated $\mathrm{d}r\varphi'_{\mathrm{Calculation}}$ from the measured $\mathrm{d}r\varphi'$ are shown in Figure 5.15. They are plotted as a function of the TPC sector and z for two different q/p_{T}. At small radii on the A-side in the upper panel the difference is of the order of 1 cm depending on the q/p_{T} since the magnitude of the measured distortions increases with rising q/p_{T}. A similar behavior of the residuals is observed for different z as they increase by about 50 % from $z = 80\,\mathrm{cm}$ to $z = 10\,\mathrm{cm}$. The residual fluctuations in φ are of the order of 40 %.

The residuals at small radii on the C-side are shown in the middle panel of Figure 5.15. A decrease of the space-charge distortions is expected because of the muon absorber. The observed offset of the residuals is bigger than for the A-side while the fluctuations in φ are of the same order. The relative difference of the residuals for different z-positions is also comparable to the A-side. The difference of the space-charge distortions between A- and C-side is disregarded in the calculations thus explaining the increased offset on the C-side. In general, the offset of the residuals can be reduced to the unknown space-charge density in the open gating grid data. The uncertainties of the assumption of $\varepsilon = 15$ in the calculations have to be considered for the comparison to the data.

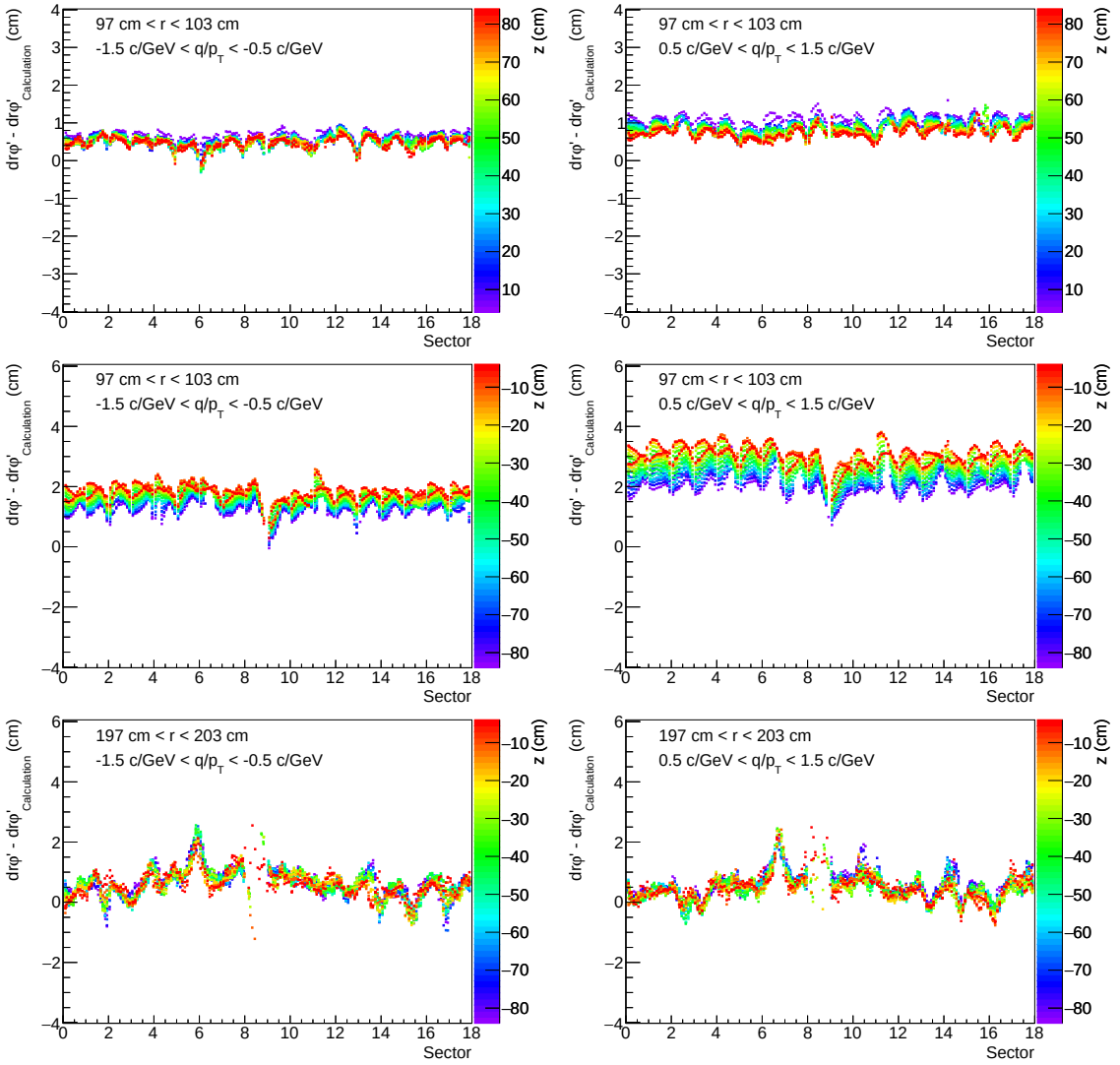

Figure 5.15: The difference of the measured distortions $\mathrm{d}r\varphi'$ in the data to the calculated distortions $\mathrm{d}r\varphi'_{\mathrm{Calculation}}$ as a function of the TPC sector and z for two different q/p_{T}. The results for small radii on the A-side (upper panel), small radii on the C-side (middle panel) and large radii on the C-side (lower panel) are shown.

The lower panel of Figure 5.15 shows the residuals at a radius of 200 cm on the C-side. OROC C08 is switched off both in the data and in the calculations. The offset is smaller compared to the results at smaller radii but the magnitude of the fluctuations in φ increases significantly. This can be ascribed to the bigger uncertainties in the data towards larger radii. It is remarkable that the distortions in the vicinity of the switched off OROC are described very well by the calculations as the residuals in sectors 7 and 9 are within the fluctuations.

The average difference between the distortions in the data and the calculations as a function of the radius is shown in Figure 5.16 for different q/p_{T}. The residuals at the boundary of IROCs and OROCs are of the order of 2 mm. Towards smaller and bigger radii the differences between data and the calculation increase steadily on the

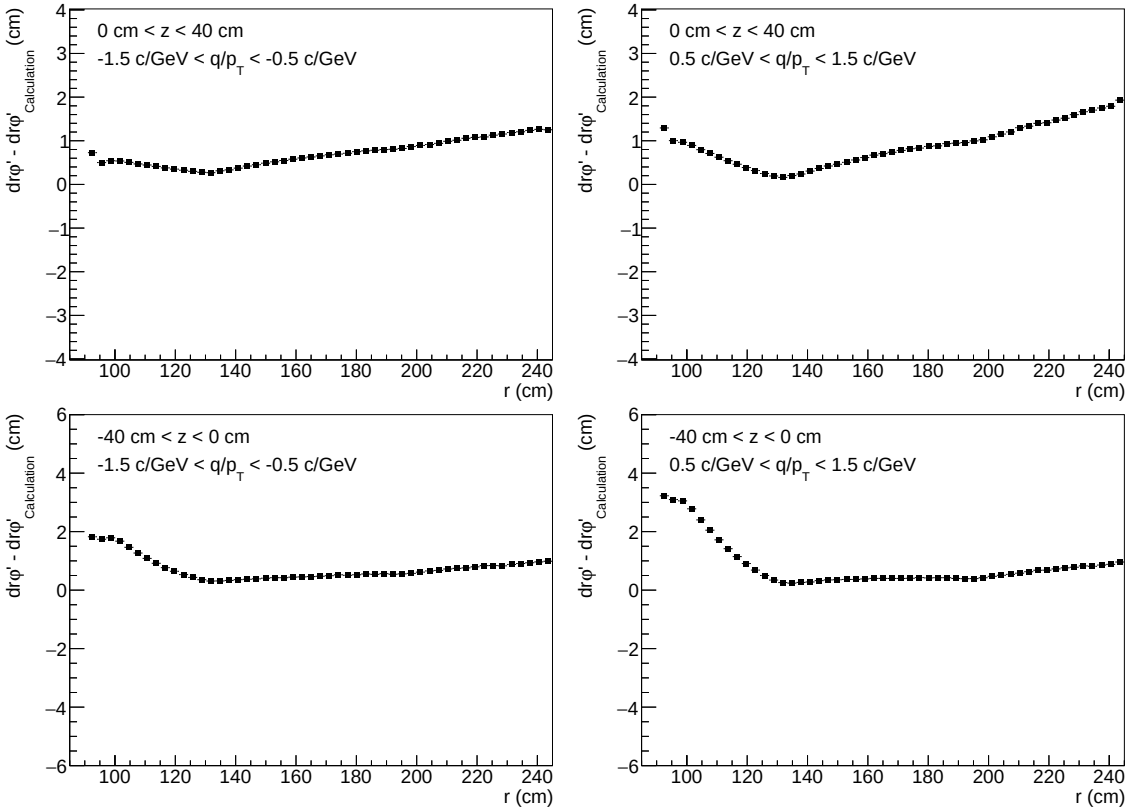

Figure 5.16: The average difference between the measured distortions $\mathrm{d}r\varphi'$ in the data and the calculated distortions $\mathrm{d}r\varphi'_{\mathrm{Calculation}}$ as a function of the radius r on the A-side (top) and C-side (bottom) for two different q/p_{T}. The statistical uncertainties are smaller than the data points.

A-side up to about 1 cm in the IROC and almost 2 cm in the OROC. Considering the shape of the measured distortions in Figure 5.11, the assumption of $\varepsilon = 15$ for the space-charge density overestimates the ion density in the IROCs and underestimates the ion density in the OROCs on the A-side. This can be explained by the different gains in the IROCs and OROCs which are applied in the real operation of the TPC due to the different pad sizes. According to simulations, the ion backflow is nearly the same for both types of readout chambers but the difference in gain leads to a difference in the absolute number of ions drifting back into the drift volume. On the C-side the ion density in the IROC is even more overestimated as the residuals are of the order of 2–3 cm at the inner field cage. In the OROC the residuals of about 1 cm at the outer field cage are smaller compared to the A-side. This observation is in agreement with the expected difference of the space-charge distortions on the A- and C-side.

5.4 Outlook

The available open gating grid data has the potential to significantly contribute to the understanding of the space-charge distortions in the TPC and to the further

development of the distortion models and calculations, which is crucial for the TPC upgrade. A comparison to current calculations demonstrates the performance and robustness of the model and calculation methods, using a simplified assumption of the ion density in the data. To improve the performance, the results obtained from the calculations can be fitted to the data by scaling the input density for IROCs, OROCs and for each chamber individually. Further developments include the implementation of a realistic ion drift in the TPC drift volume. The ion drift is distorted in a similar way as the electrons, but in the opposite direction, leading to an effective reduction of the space-charge density.

Further data with an open gating grid will provide the opportunity for a significantly better understanding of the behavior of the space-charge distortions with respect to the ion density inside the TPC. The conditions during LHC Run 2 are suitable for further open gating grid runs. The change of the main gas to Ar leads to a substantial increase of the space-charge distortions. A scan of the interaction rates offers the possibility to measure the distortions as a function of different ion densities similar to a variation of ε. The data analyzed in Section 5.3.2 only provide the average distortions over one run while the effective collision rate slightly decreases during a run.

Furthermore, the open gating grid data provide a useful test ground for the proposed calibration and correction schemes in [35]. The tracking performance of the TPC can be studied using different correction approaches for the data. The performance of the newly developed algorithms for the Run 2 and Run 3 data reconstruction can be verified and optimized in the extreme conditions of large space-charge distortions in the open gating grid data.

6 Summary

In this work the properties and operational requirements of Ar-based gas mixtures are evaluated to determine the eligibility for the application in the ALICE TPC. The obtained results are compared to Ne-based gas mixtures which were successfully used during LHC Run 1.

The electron transport properties are relevant for the drift of electrons in the TPC drift volume and are calculated with the Magboltz interface of the Garfield framework. At the nominal drift field of $E = 400\,\mathrm{V/cm}$ and a parallel magnetic field of $B = 0.5\,\mathrm{T}$, Ar-CO_2 with a CO_2 fraction of 12 % and 10 % show similar properties as Ne-CO_2 (90-10) and Ne-CO_2-N_2 (90-10-5). The electron drift velocity of Ar-CO_2 (88-12) is nearly identical to the one of Ne-CO_2 (90-10). The transverse diffusion coefficient is 5 % lower while the longitudinal diffusion coefficient is 6 % higher. For Ar-CO_2 (90-10) the drift velocity is 20 % higher resulting in a shorter drift time for the ionization electrons. The diffusion coefficients are 6–13 % higher than for Ne-CO_2 (90-10). Mixtures of Ne or Ar with CF_4 show promising electron transport properties but CF_4 has still to be validated for the use in the TPC.

The major ionization properties of the gas mixtures are calculated with the HEED interface to Garfield. The amount of primary ionization and the average total ionization in Ar-CO_2 is larger by a factor of two compared to Ne-CO_2 due to the lower ionization potential of Ar. The calculated values for the primary ionization are $N_\mathrm{p} = 27\,\mathrm{electrons/cm}$ for Ar-CO_2 and $N_\mathrm{p} = 14\,\mathrm{electrons/cm}$ for Ne-CO_2 and Ne-CO_2-N_2. The average total ionization amounts to $\langle N_\mathrm{t} \rangle = 75\,\mathrm{electrons/cm}$ and $\langle N_\mathrm{t} \rangle = 38\,\mathrm{electrons/cm}$, respectively.

The lower mobility of the ions in the Ar mixtures leads to a lower drift velocity of the Ar^+- and $CO_2{}^+$-ions. Therefore the closing time of the gating grid of the MWPCs has to be adjusted for the change to Ar. Simulations of the ion drift times in the TPC readout chambers are performed with the Garfield software package for the various Ne- and Ar-based gas mixtures. Using the nominal voltage settings for the gating grid wires, an ion-collection time of 175–191 μs is calculated for Ne-CO_2 (90-10) and Ne-CO_2-N_2 (90-10-5). The ion-collection time for the Ar-CO_2 mixtures is a factor 2.5–2.8 higher as it takes about 490 μs to collect all ions. By

tuning of the voltages of the gating grid wires, an improvement down to $\sim$450 μs can be achieved. Opening the gating grid early and taking an ion backflow of 1 % into account, ion-collection times of $\sim$350–400 μs are possible. However, the ion backflow results in significant space-charge distortions which have to be considered during the reconstruction of the data. The drift times of the ions and the ion backflow are also calculated for the case of an open gating grid. The latter amounts 13 % for Ne-CO_2 (90-10), 11 % for Ne-CO_2-N_2 (90-10-5) and about 12 % for the Ar-CO_2 mixtures.

Furthermore, possible space-charge effects in the TPC are studied. The expected space-charge distortions for the TPC upgrade are discussed. The gating grid of the TPC readout chambers was operated in the open state during a dedicated run in 2013. The magnitude of the resulting distortions due to the ion backflow is measured and analyzed. Indications of the space-charge distortions are observed in the tracking performance, particularly in the distributions of clusters assigned to TPC tracks and of all clusters measured in the TPC. The matching efficiencies to the external detectors also suffer from the low cluster-to-track association in this extreme environment. The measured distortions in $r\varphi$ are of the order of 3 cm near the central electrode and at the inner and outer field cage. Regarding the behavior of the distortions with respect to the radius, TPC sector and z, the obtained results are in agreement with expectations and simulations performed for the TPC upgrade. The magnitude of the measured distortions in the open gating grid data amounts to half of what is expected for the $\varepsilon = 20$ scenario for the upgrade of the TPC. A comparison to available calculations demonstrates the performance of the current model and calculation techniques while the prospect of potential improvements and further developments is presented.

Bibliography

[1] D. Griffiths. *Introduction to Elementary Particles*. WILEY-VCH, 2nd edition, 2009.

[2] G. Danby, J-M. Gaillard, K. Goulianos, L. M. Lederman, N. Mistry, M. Schwartz, and J. Steinberger. Observation of High-Energy Neutrino Reactions and the Existence of Two Kinds of Neutrinos. *Phys. Rev. Lett.*, 9(36), 1962. doi:10.1103/PhysRevLett.9.36.

[3] C. D. Anderson. The Positive Electron. *Phys. Rev.*, 43(491), 1933. doi:10.1103/PhysRev.43.491.

[4] C. M. G. Lattes, G. P. S. Occhialini, and C. F. Powell. Observations on the Tracks of Slow Mesons in Photographic Emulsions. *Nature*, 160(453, 486), 1947. dx.doi.org/10.1038/160453a0, dx.doi.org/10.1038/160486a0.

[5] G. D. Rochester and C. C. Butler. Evidence for the Existence of New Unstable Elementary Particles. *Nature*, 160(855), 1947. doi:10.1038/160855a0.

[6] M. Gell-Mann. Symmetries of Baryons and Mesons. *Phys. Rev.*, 125(1067), 1962. doi:10.1103/PhysRev.125.1067.

[7] M. Gell-Mann. A schematic model of baryons and mesons. *Phys. Letters*, 8(3), 1964. doi:10.1016/S0031-9163(64)92001-3.

[8] S. C. C. Ting et al. Experimental Observation of a Heavy Particle J. *Phys. Rev. Lett.*, 33(1404), 1974. doi:10.1103/PhysRevLett.33.1404.

[9] J. E. Augustin et al. Discovery of a Narrow Resonance in e^+e^- Annihilation. *Phys. Rev. Lett.*, 33(1406), 1974. doi:10.1103/PhysRevLett.33.1406.

[10] S. W. Herb et al. Observation of a Dimuon Resonance at 9.5 GeV in 400-GeV Proton-Nucleus Collisions. *Phys. Rev. Lett.*, 39(252), 1977. doi:10.1103/PhysRevLett.39.252.

[11] G. Arnison et al. Experimental observation of isolated large transverse energy electrons with associated missing energy at $\sqrt{s} = 540\,\text{GeV}$. *Physics Letters B*, 122(1), 1983. doi:10.1016/0370-2693(83)91177-2.

[12] K.A. Olive et al. (Particle Data Group). Review of Particle Physics. *Chin.Phys.*, C38(090001), 2014. doi:10.1088/1674-1137/38/9/090001.

[13] B. Povh, K. Rith, C. Scholz and F. Zetsche. *Teilchen und Kerne, Eine Einfürung in die physikalischen Konzepte*. Springer, 7th edition, 2006.

[14] U. W. Heinz. The Little Bang: searching for quark-gluon matter in relativistic heavy-ion collisions. *Nuclear Physics A*, 685(1-4), 2001. doi:10.1016/S0375-9474(01)00558-9.

[15] U. W. Heinz. Concepts of heavy ion physics. 2004. arXiv:hep-ph/0407360.

[16] S. Sarkar, H. Satz and B. Sinha (Eds.). *The Physics of the Quark-Gluon Plasma: Introductory Lectures, Lect. Notes Phys. 785*. Springer, 2010.

[17] P. Braun-Munzinger and J. Stachel. (Non)thermal aspects of charmonium production and a new look at J/ψ suppression. *Physics Letters B*, 490(3-4), 2000. doi:10.1016/S0370-2693(00)00991-6.

[18] R. L. Thews, M. Schroedter and J. Rafelski. Enhanced J/ψ production in deconfined quark matter. *Phys. Rev. C*, 63(054905), 2001. doi:10.1103/PhysRevC.63.054905.

[19] ALICE Collaboration. Inclusive, prompt and non-prompt J/ψ production at mid-rapidity in Pb-Pb collisions at $\sqrt{s_{\mathrm{NN}}} = 2.76\,\mathrm{TeV}$. *JHEP*, 1507, 2015. doi:10.1007/JHEP07(2015)051.

[20] L. Evans and P. Bryant. LHC Machine. *JINST*, 3(S08001), 2008. doi:10.1088/1748-0221/3/08/S08001.

[21] ALICE Collaboration et al. ALICE: Physics Performance Report, Volume I. *J. Phys. G: Nucl. Part. Phys.*, 30(11), 2004. doi:10.1088/0954-3899/30/11/001.

[22] ALICE Collaboration et al. ALICE: Physics Performance Report, Volume II. *J. Phys. G: Nucl. Part. Phys.*, 32(10), 2006. doi:10.1088/0954-3899/32/10/001.

[23] ALICE Collaboration, July 2015. URL: http://aliweb.cern.ch.

[24] B. Abelev et al (The ALICE Collaboration). Upgrade of the ALICE Experiment: Letter Of Intent. *J. Phys. G: Nucl. Part. Phys.*, 41(087001), 2014. doi:10.1088/0954-3899/41/8/087001.

[25] L. Betev and P. Chochula. Definition of the ALICE Coordinate System and Basic Rules for Sub-detector Components Numbering. ALICE-INT-2003-038, 2003.

[26] J. Wiechula. *Commissioning and Calibration of the ALICE-TPC*. Phd thesis, Goethe-Universität Frankfurt am Main, 2008.

[27] The ALICE Collaboration et al. The ALICE experiment at the CERN LHC. *JINST*, 3(S08002), 2008. doi:10.1088/1748-0221/3/08/S08002.

[28] ALICE Collaboration. Technical Design Report of the Time Projection Chamber. CERN-LHCC-2000-001, 2000.

[29] J. Alme et al. The ALICE TPC, a large 3-dimensional tracking device with fast readout for ultra-high multiplicity events. *Nucl. Instrum. Methods Phys. Res. A*, 622(1), 2010. doi:10.1016/j.nima.2010.04.042.

[30] R. Veenhof. Choosing a gas mixture for the ALICE TPC. ALICE-INT-2003-29, 2003.

[31] C. Garabatos. The ALICE TPC. *Nucl. Instrum. Methods Phys. Res. A*, 535(1–2), 2004. doi:10.1016/j.nima.2004.07.127.

[32] B.S. Nielsen, J. Westergaard, J.J. Gaardhoje and A. Lebedev. Design Note on the ALICE TPC laser calibration system. ALICE-INT-2002-22, 2002.

[33] C. Lippmann and D. Vranic. ALICE TPC Numbering Conventions.

[34] ALICE Collaboration. Technical Design Report of the Trigger, Data Acquisition, High-Level Trigger and Control System. CERN-LHCC-2003-062, 2004.

[35] ALICE Collaboration. Technical Design Report for the Upgrade of the ALICE Time Projection Chamber. CERN-LHCC-2013-020, 2014.

[36] ALICE Collaboration. Addendum to the Technical Design Report for the Upgrade of the ALICE Time Projection Chamber. CERN-LHCC-2015-002, 2015.

[37] W. Blum, W. Riegler and L. Rolandi. *Particle Detection with Drift Chambers*. Springer, 2nd edition, 2008.

[38] ALICE Collaboration. Performance of the ALICE Experiment at the CERN LHC. *Int. J. Mod. Phys. A*, 29(24), 2014. doi:10.1142/S0217751X14300440.

[39] K. Kleinknecht. *Detektoren für Teilchenstrahlung*. Teubner, 3rd edition, 1992.

[40] R. Veenhof. Garfield Version 9, 2013.

[41] S. Biagi. Magboltz Version 7.08, 2012.

[42] I. Smirnov. HEED Version 1.01, 2007.

[43] C. Garabatos. Private communication.

[44] Y. Kalkan, M. Arslandok, A.F.V. Cortez, Y. Kaya, İ. Tapan and R. Veenhof. Cluster ions in gas-based detectors. *JINST*, 10(P07004), 2015. doi:10.1088/1748-0221/10/07/P07004.

[45] S. Rossegger. *Simulation and Calibration of the ALICE Time-Projection Chamber including innovative Space Charge Calculations.* Phd thesis, Technische Universität, Graz, 2009.

[46] AliRoot. ALICE Offline Analysis Framework. URL: http://aliweb.cern.ch/Offline/AliRoot/Manual.html.

[47] ROOT Data Analysis Framework. URL: https://root.cern.ch.

[48] S. Rossegger, B. Schnizer and W. Riegler. Analytical solutions for space charge fields in TPC drift volumes. *Nucl. Instrum. Methods Phys. Res. A*, 632(1), 2011. doi:doi:10.1016/j.nima.2010.12.213.

[49] M. Mager, S. Rossegger, J. Thomas. The Langevin Equation expanded to 2^{nd} order and comments on using the equation to correct for space point distortions in a TPC. ALICE-INT-2010-016, 2010.

[50] S. Rossegger, J. Thomas. Space-charge effects in the ALICE TPC: a comparison between expected ALICE performance and current results from the STAR TPC. ALICE-INT-2010-017, 2011.

[51] M. Ivanov. Private communication.

[52] J. Wiechula. Private communication.

Erklärung nach §28 (12) Ordnung des FB Physiks (Fassung 2011) an der Goethe-Universität für den Bachelor- und den Masterstudiengang

Hiermit erkläre ich, dass ich diese Arbeit selbstständig und ohne Benutzung anderer als der angegebenen Quellen und Hilfsmittel verfasst habe. Alle Stellen der Arbeit, die wörtlich oder sinngemäß aus Veröffentlichungen oder aus anderen fremden Texten entnommen wurden, sind von mir als solche kenntlich gemacht worden. Ferner erkläre ich, dass die Arbeit nicht - auch nicht auszugsweise - für eine andere Prüfung verwendet wurde.

Frankfurt, den 27.10.2015

Ernst Hellbär

Danksagung

Zunächst möchte ich mich bei Prof. Dr. Harald Appelshäuser bedanken, der diese Arbeit ermöglicht und mir die Gelegenheit gegeben hat in die Welt der TPC einzutauchen. Mit regelmäßigem Feedback und viel Geduld hat er mir immer wieder Denkanstöße und neue Sichtweisen aufgezeigt, die die Ergebnisse dieser Arbeit vorangetrieben haben. Besonderer Dank gilt auch Prof. Dr. Christoph Blume, der freundlicherweise die Zweitkorrektur übernimmt, und Rainer Renfordt, Jens Wiechula und Kai Schweda, die diese Arbeit korrekturgelesen und wertvolles Feedback zu potentiellen Verbesserungen gegeben haben.

Weiterhin bedanke ich mich bei der gesamten ALICE TPC Gruppe, in der jeder jederzeit für Rat und Tat zur Seite steht. Christian Lippmann und Chilo Garabatos haben mir den Einstieg in das Thema erleichtert und bei Fragen über Space-Charge, Garfield, Gaseigenschaften, Readout Chambers, etc. stets weitergeholfen. Ebenso hilfreich und interessant waren die Gespräche mit Rainer Renfordt am IKF, der für alle Beobachtungen Erklärungansätze parat hat. Marian Ivanov und Jens Wiechula waren (und sind immer noch) unverzichtbar bei Fragen zu TPC Offline Themen und haben bei der Analyse der Open Gating Grid Daten und deren Interpretation einen wertvollen Beitrag geleistet. Auch Mesut Arslandok hat mir bei Schwierigkeiten beim Programmieren stets unter die Arme gegriffen. Bei der gesamten Arbeitsgruppe am IKF möchte ich mich für die sehr nette und angenehme Atmosphäre und für die unendliche Hilfsbereitschaft bei jeglichen Anliegen bedanken. Außerdem habt Ihr mir das Tor zu meiner neusten Leidenschaft (den Fußball ;-)) geöffnet. Speziell möchte ich mich dabei bei Susanne Gläßel, Esther Bartsch und Florian Roether bedanken für die erholsamen und motivierenden Zeiten am See oder im Park und für die geselligen Grillabende und Mahlzeiten in der Mensa oder sonstigen Edelrestaurants.

Ganz besonders bedanke ich mich bei meiner Familie, die mich schon immer mit all ihrer Kraft unterstützt hat und es mir stets ermöglicht all meine Ziele zu erreichen. Danke auch an all meine Freunde, die mich den Alltag vergessen lassen und die wirklich wichtigen Dinge im Lebens ins Bewusstsein rufen.